

UNIVERSIDADE DE SÃO PAULO  
CENTRO DE ENERGIA NUCLEAR NA AGRICULTURA

NÁDIA MARION DURAN

X-ray spectroscopy uncovering the effects of Cu and Fe based nanoparticles on  
*Phaseolus vulgaris* L. germination and seedling development

Piracicaba  
2018



NÁDIA MARION DURAN

X-ray spectroscopy uncovering the effects of Cu and Fe based nanoparticles on  
*Phaseolus vulgaris* L. germination and seedling development

Dissertação apresentada ao Centro de Energia Nuclear na Agricultura da Universidade de São Paulo para obtenção do título de Mestre em Ciências

Área de Concentração: Química na Agricultura e no Ambiente

Orientador: Prof. Dr. Hudson Wallace Pereira de Carvalho

Piracicaba  
2018

AUTORIZO A DIVULGAÇÃO TOTAL OU PARCIAL DESTE TRABALHO, POR QUALQUER MEIO CONVENCIONAL OU ELETRÔNICO, PARA FINS DE ESTUDO E PESQUISA, DESDE QUE CITADA A FONTE.

Dados Internacionais de Catalogação na Publicação (CIP)

**Técnica de Biblioteca - CENA/USP**

Duran, Nádia Marion

Efeitos de nanopartículas à base de Cu e Fe na germinação e desenvolvimento de plântulas de *Phaseolus vulgaris* L. observados por espectroscopia de raios-X / X-ray spectroscopy uncovering the effects of Cu and Fe based nanoparticles on *Phaseolus vulgaris* L. germination and seedling development / Nádia Marion Duran; orientador Hudson Wallace Pereira de Carvalho. - - Piracicaba, 2018.

88 p. : il.

Dissertação (Mestrado – Programa de Pós-Graduação em Ciências. Área de concentração: Química na Agricultura e no Ambiente) – Centro de Energia Nuclear na Agricultura, Universidade de São Paulo, 2018.

1. Espectroscopia de raios X 2. Fluorescência de raios X 3. Germinação de sementes 4. Magnetita 5. Nanopartículas 6. Óxido de cobre 7. Química analítica instrumental 8. Radiação sincrotron I. Título.

CDU (620.3 + 631.547.1) : 543.427

**Elaborada por:**

Marilia Ribeiro Garcia Henyei

CRB-8/3631

Resolução CFB Nº 184 de 29 de setembro de 2017

## ACKNOWLEDGMENTS

First of all, I am grateful to Prof. Hudson Wallace Pereira de Carvalho whose experience, guidance, patience, full dedication and support made this work possible.

I thank the Center for Nuclear Energy in Agriculture (CENA) and the University of São Paulo (USP) for the opportunity and for providing me with all the necessary facilities to develop this work.

I am also very grateful to the Coordination for the Improvement of Higher Level Personnel (CAPES) for granting the scholarship.

My deepest gratitude to Dr. Eduardo de Almeida for sharing his knowledge with me, having the patience and providing all the support during the XRF analysis. I cannot measure how grateful I am!

I would like to thank my fellow PhD and Masters students from the Laboratory of Nuclear Instrumentation (LIN) Susilaine, Tatiana, Joyce, Geovani, Marcos and Eduardo for the friendship, cooperation and companionship during the development of this work. I am also grateful to the scientific initiation students João and Rafael for the experimental support. It was a pleasure working with you!

My acknowledgments to the Brazilian Agricultural Research Corporation (EMBRAPA) and the Agronomic Institute of Campinas (IAC) for the supplied *Phaseolus vulgaris* L. seeds.

I thank the Brazilian Synchrotron Light Laboratory (LNLS) for beamtimes at XRF, XAFS2 and IMX beamlines and the beamlines scientists Dr. Carlos A. Perez, Dr. Douglas Galante and Dr. Santiago Figueroa for their support during the XAS measurements, and Prof. Eduardo F. Molina (UNIFRAN) for assistance during beamtime at IMX beamline.

The Brazilian Nanotechnology National Laboratory (LNNano) and the Brazilian Biosciences National Laboratory (LNBio) are also acknowledged for providing their facilities for the nanoparticles characterization.

Prof. Cornelis A. M. van Gestel (Vrije Universiteit) who made comments and suggestions that greatly improved the chapter one of this dissertation.

I am very grateful to Prof. Davide Mattia and Maria Maria Medina-Llamas (University of Bath) for synthesizing and providing the magnetite nanoparticles and for their collaboration in the second chapter of this dissertation. Dr. Willian R. Macedo is acknowledged (UFV) for the  $\alpha$ -amylase analysis and his insights.

I would like to acknowledge the assistance of Prof. Francisco S. Linhares and the Technician Monica L. Rossi for the root clearing and microscopy preparations.

Prof. Silvio M. Cícero and Dr. Francisco G. Gomes Júnior (LPV/ESALQ/USP) for providing the Image Analysis Laboratory facilities.

Profa. Célia Regina Montes for her availability and support during the SEM analysis.

Special thanks to my husband and my best friend Guilherme, for his unfailing support, understanding and companionship.

Most importantly, none of this could have happened without my family, especially for my parents Eduardo and Gisela and their continuous encouragement over my years of study.

## ABSTRACT

DURAN, N. M. **X-ray spectroscopy uncovering the effects of Cu and Fe based nanoparticles on *Phaseolus vulgaris* L. germination and seedling development.** 2018. 88 p. Dissertação (Mestrado em Ciências) – Centro de Energia Nuclear na Agricultura, Universidade de São Paulo, Piracicaba, 2018.

Nanotechnology offers a great potential do design fertilizers with unique properties capable to boost the plant productivity. However, the nanoparticles environmental fate and their toxic responses still need to be deeply investigated to their safe use. This study aims to investigate the effect of copper oxide (nCuO) and magnetite nanoparticles (nFe<sub>3</sub>O<sub>4</sub>) on the germination and seedling development of *Phaseolus vulgaris* L. Seeds were treated in nanoparticles dispersions in a wide range of concentrations (1, 10, 100 and 1 000 mg L<sup>-1</sup>) and incubated in a germination chamber during 5 days. Different sized nCuO (25, 40 and <80 nm) and polyethylene glycol (PEG) coated nFe<sub>3</sub>O<sub>4</sub> were evaluated. Although both nCuO and nFe<sub>3</sub>O<sub>4</sub> treatments did not affected the germination rate, seedling weight gain was promoted by 40 nm CuO at 100 mg Cu L<sup>-1</sup> and inhibited by 1 000 mg Cu L<sup>-1</sup> of 25 nm CuO and positive control (CuSO<sub>4</sub>). Among the tested nCuO, the higher chemical reactivity was found for the 25 nm CuO, and this may partially explain the observed deleterious effects. Seeds treated in nFe<sub>3</sub>O<sub>4</sub>-PEG at 1 000 mg Fe L<sup>-1</sup> increased radicle elongation compared to the negative control (water), while Fe<sup>2+</sup>/Fe<sup>3+</sup><sub>(aq)</sub> (positive control) and bare nFe<sub>3</sub>O<sub>4</sub> at 1 000 mg Fe L<sup>-1</sup> treatments reduced the radicle of the seedlings. The growth promoted by the PEG-coated nanoparticles can be justified by the higher water uptake induced by the PEG, and also by its lower chemical reactivity compared to the bare nanoparticles. This was reinforced by enzymatic assays since nFe<sub>3</sub>O<sub>4</sub>-PEG treatment was also the least harmful to the  $\alpha$ -amylase activity. X-ray fluorescence spectroscopy (XRF) showed that most of the Cu and Fe incorporated by the seeds remained in the seed coat, specially in the hilum region, and X-ray tomography indicated that Fe<sub>3</sub>O<sub>4</sub>-PEG penetrated in this structure. X-ray absorption spectroscopy (XAS) unraveled that the Cu and Fe chemical environment of the nCuO and nFe<sub>3</sub>O<sub>4</sub>-PEG treated seeds persisted mostly in its primitive form. These results contribute to the understanding of how nCuO, nFe<sub>3</sub>O<sub>4</sub> and nFe<sub>3</sub>O<sub>4</sub>-PEG interact with common bean seeds and seedlings and highlights its potential use in seed priming.

Keywords: *Phaseolus vulgaris* L. CuO nanoparticle. Fe<sub>3</sub>O<sub>4</sub> nanoparticle. Germination. X-ray spectroscopy. X-ray fluorescence. X-ray absorption. X-ray tomography.



## RESUMO

DURAN, N. M. **Efeitos de nanopartículas à base de Cu e Fe na germinação e desenvolvimento de plântulas de *Phaseolus vulgaris* L. observados por espectroscopia de raios-X.** 2018. 88 p. Dissertação (Mestrado em Ciências) – Centro de Energia Nuclear na Agricultura, Universidade de São Paulo, Piracicaba, 2018.

A nanotecnologia oferece um grande potencial para o desenvolvimento de fertilizantes com propriedades únicas, capazes de impulsionar a produtividade das plantas. Contudo, o destino ambiental e os efeitos tóxicos das nanopartículas ainda necessitam ser profundamente investigados para o seu uso seguro. Este estudo visa investigar o efeito das nanopartículas de óxido de cobre (nCuO) e magnetita (nFe<sub>3</sub>O<sub>4</sub>) na germinação e desenvolvimento das plântulas de *Phaseolus vulgaris* L. As sementes foram tratadas em dispersões de nanopartículas em diversas concentrações (1, 10, 100 and 1 000 mg L<sup>-1</sup>) e incubadas em uma câmara de germinação durante 5 dias. Diferentes tamanhos de nCuO (25, 40 e <80 nm) e nFe<sub>3</sub>O<sub>4</sub> recoberta com polietileno glicol (PEG) e foram avaliados. Embora ambos tratamentos de nCuO e nFe<sub>3</sub>O<sub>4</sub> não afetaram a taxa de germinação, o ganho de massa das plântulas foi promovido pela nCuO de 40 nm à 100 mg Cu L<sup>-1</sup> e inibido pelos tratamentos de nCuO de 25 nm e controle positivo (CuSO<sub>4</sub>) à 1 000 mg Cu L<sup>-1</sup>. Dentre as nCuO testadas, a maior reatividade química foi encontrada para a nCuO de 25 nm, e isso pode explicar parcialmente os efeitos deletérios desta nanopartícula. Sementes tratadas com nFe<sub>3</sub>O<sub>4</sub>-PEG à 1 000 mg Fe L<sup>-1</sup> aumentaram o alongamento das radículas em comparação ao controle negativo (água), enquanto que os tratamentos Fe<sup>2+</sup>/Fe<sup>3+</sup><sub>(aq)</sub> (controle positivo) e nFe<sub>3</sub>O<sub>4</sub> sem recobrimento à 1 000 mg Fe L<sup>-1</sup> reduziram as radículas das plântulas. O crescimento promovido pelas nanopartículas recobertas com PEG pode ser justificado pela maior absorção de água induzido pelo PEG, e também pela sua baixa reatividade química comparada às nanopartículas sem recobrimento. Isso foi reforçado por ensaios enzimáticos uma vez que o tratamento de nFe<sub>3</sub>O<sub>4</sub>-PEG foi também o menos prejudicial à atividade da  $\alpha$ -amilase. A espectroscopia de fluorescência de raios-X (XRF) mostrou que a maior parte do Cu e do Fe incorporados pelas sementes permaneceu no tegumento, especialmente na região do hilo, e a tomografia de raios-X indicou que nFe<sub>3</sub>O<sub>4</sub>-PEG penetrou nesta estrutura. A espectroscopia de absorção de raios-X (XAS) revelou que o ambiente químico do Cu e do Fe das sementes tratadas com nCuO e nFe<sub>3</sub>O<sub>4</sub>-PEG persistiram majoritariamente em sua forma primitiva. Estes resultados contribuem para o entendimento de como nCuO, nFe<sub>3</sub>O<sub>4</sub> e nFe<sub>3</sub>O<sub>4</sub>-PEG interagem com sementes de feijão e destaca seu potencial uso no tratamento de sementes.

Palavras-chave: *Phaseolus vulgaris* L. Nanopartícula de CuO. Nanopartícula de Fe<sub>3</sub>O<sub>4</sub>. Germinação. Espectroscopia de raios-X. Fluorescência de raios-X. Absorção de raios-X. Tomografia de raios-X.



## SUMMARY

1 INTRODUCTION .....	11
1.1 Hypothesis .....	15
1.2 Objectives .....	15
1.3 Structure of the dissertation .....	16
References .....	16
2 X-RAY SPECTROSCOPY UNCOVERING THE EFFECTS OF CU BASED NANOPARTICLE CONCENTRATION AND STRUCTURE ON <i>PHASEOLUS VULGARIS</i> GERMINATION AND SEEDLING DEVELOPMENT .....	21
2.1 Introduction .....	22
2.2 Materials and Methods .....	24
2.2.1 Characterization of pristine CuO nanoparticles and dispersions.....	24
2.2.2 Germination assay .....	25
2.2.3 Copper uptake quantification.....	25
2.2.4 nCuO solubility.....	26
2.2.5 Mapping the Cu accumulation spots .....	26
2.2.6 Copper chemical speciation analysis.....	27
2.2.7 Root microscopic analysis .....	27
2.2.8 Surface reactivity of CuO nanoparticles.....	28
2.2.9 Statistical analysis.....	28
2.3 Results and Discussion .....	28
2.3.1 Characterization of the nanoparticles and dispersions .....	28
2.3.2 Effects of nCuO on seed germination and seedling growth.....	31
2.3.3 Determination of Cu uptake by <i>Phaseolus vulgaris</i> seeds .....	35
2.3.4 Spatial distribution of Cu in the soaked seeds.....	38
2.3.5 Chemical speciation of the incorporated Cu.....	40
2.3.6 <i>In vivo</i> spatial distribution of Cu in the seedlings .....	42
2.3.7 Chemical reactivity of Cu based nanoparticles and physiological effects .....	45
2.4 Conclusions .....	47
References .....	47

3 BEAN SEEDLING GROWTH ENHANCEMENT USING MAGNETITE NANOPARTICLES.....	53
3.1 Introduction.....	54
3.2 Materials and Methods.....	56
3.2.1 Synthesis of iron oxide nanoparticles .....	56
3.2.2 Characterization of pristine Fe <sub>3</sub> O <sub>4</sub> nanoparticles and dispersions .....	56
3.2.3 Germination assay.....	57
3.2.4 Radicle length determination .....	58
3.2.5 Iron uptake quantification .....	58
3.2.6 nFe <sub>3</sub> O <sub>4</sub> solubility.....	59
3.2.7 Mapping Fe accumulation spots .....	60
3.2.8 3D distribution and chemical speciation of Fe in the hilum .....	60
3.2.9 Reactivity of soluble-Fe and magnetite nanoparticles .....	61
3.2.10 $\alpha$ -amylase activity .....	61
3.2.11 Statistical analysis .....	62
3.3 Results and Discussion.....	62
3.3.1 Characterization of the nanoparticles and dispersions.....	62
3.3.2 Effects of magnetite nanoparticles on <i>P. vulgaris</i> seed germination and radicle growth.....	65
3.3.3 Determination of Fe uptake by <i>P. vulgaris</i> seeds .....	69
3.3.4 Spatial distribution and chemical speciation of Fe in the primed seeds .....	71
3.3.5 Chemical reactivity of nFe <sub>3</sub> O <sub>4</sub> and nFe <sub>3</sub> O <sub>4</sub> -PEG .....	77
3.3.6 $\alpha$ -amylase activity .....	77
3.4 Conclusions.....	80
References.....	80
4. FINAL REMARKS AND OUTLOOK.....	87

## 1 INTRODUCTION

To achieve a successful growth and yield, crop plants require 17 essential minerals. The elements that are required in higher amounts are known as macronutrients, while those required in trace quantities are called micronutrients, although they are evenly important for plant growth. Namely, macronutrients are carbon, hydrogen, oxygen, nitrogen, phosphorus, potassium, calcium, magnesium and sulfur. Micronutrients comprise zinc, copper, iron, manganese, boron, molybdenum, chlorine, and nickel.<sup>1</sup>

Copper (Cu) is an essential redox-active element required for several biochemical and physiological process like photosynthesis, respiration, carbohydrate, lipid and nitrogen metabolism, protection against oxidative stress and lignification of plant cell walls. It is a cofactor in many enzymes such as superoxide dismutase and cytochrome c oxidase.<sup>1; 2</sup> Iron (Fe) is a cofactor in the biosynthesis of chlorophyll, and it is essential for the structure and function of the photosynthetic apparatus. It is an important constituent of enzymes involved in redox reactions like cytochromes and iron-sulfur proteins, and many others proteins participants of photosynthesis, nitrogen fixation and respiration.<sup>1; 3; 4</sup>

To improve the plant nutritional status fertilizers are commonly supplied through soil or foliar application. The former present some limitations since some soil properties can interfere in element solubility and take up by plant roots.<sup>1</sup> Whilst the latter needs higher leaf area index for absorption, several sprays sessions for macronutrients, caution when applying high concentrated nutrient solutions to avoid leaf damage and, besides that, fertilizer can be washed out by rain.<sup>5</sup>

Priming seeds with nutrient-containing solutions is an attractive and easy alternative to complement these methods. Seed treatment requires few external inputs and low cost technologies. It is a simple and effective method of nutrient application.<sup>6</sup>

The seed priming consists in exposing the seeds to a certain solution, or dispersion, for a certain period. Meanwhile, the seed is partially hydrated but the radicle emergency does not happen. Although the germination process does not occur, this moisture level triggers pre-germination metabolic activity such as nucleic acid and protein synthesis and repair, that generally favor germination rate and seedling development.<sup>7</sup> The major seed priming techniques include hydropriming (seeds are soaked in water), osmopriming (osmotic solutions like polyethylene glycol), halopriming (salt solutions such as  $\text{CuSO}_4$  and  $\text{CaCl}_2$ ) and solid matrix priming (using solid carriers).<sup>8</sup>

In general, the germination process is triphasic: phase I, or imbibition, is when the dry seed take up water and the metabolic activities are low, whereas during phase II, there is little water uptake but intense metabolic activities. In phase III water content increases again concomitantly with radicle emergence and growth.<sup>9</sup> Regarding *Phaseolus vulgaris* seeds, the seed coat becomes wrinkled and the embryo starts to swell in the earlier hours of imbibition. After 48 and 72 hours, the radicle emerges and secondary roots are formed.<sup>10</sup>

In the last ten years, many efforts have been devoted to investigate how agriculture can be benefited by nanotechnology. A nanoparticle is typically defined as a material with a characteristic dimension from 1 to 100 nm.<sup>11</sup> Due to their high surface area and nanoscale size, they usually differ from their bulk counterparts presenting new chemical and/or physical properties, such as mechanical strength,<sup>12</sup> optical absorption or emission energy shifts,<sup>13</sup> chemical reactivity,<sup>14</sup> surface charges,<sup>15</sup> magnetism,<sup>16</sup> higher thermal conductivity<sup>17</sup> and solubility.<sup>18</sup> Some of these features, as surface charges, solubility and chemical reactivity can be suitable and desired to develop new fertilizers, including those targeted to seed treatment. Studies about seed priming with nanoparticles mostly observed beneficial and detrimental effects on seed germination and plant development, which may vary according to the plant species, tested material, nanoparticle size, time of exposure and applied concentration. Table 1 shows that nanotechnology can enhance crops yield if such parameters are well established.

Seeds soaked in zinc oxide nanoparticles at 10 mg L<sup>-1</sup> elongated roots of corn seedlings.<sup>19</sup> Zinc (50-500 mg L<sup>-1</sup>) and silver (20 and 50 mg L<sup>-1</sup>) nanoparticles enhanced okra<sup>20</sup> and pearl millet<sup>21</sup> seeds germination, but decreased seedlings growth. Cucumber seeds exposed to copper oxide (100, 200, 400 and 600 mg L<sup>-1</sup>)<sup>22</sup> and zinc oxide (10, 100 and 1 000 mg L<sup>-1</sup>)<sup>19</sup> presented decreased root elongation. Although many reports showed that nanoparticles can positively or negatively affect seed germination and seedling development, the mechanisms behind these phenomena are still poorly understood.

Along with the crop yield increase appeal, there are the health and environmental issues related to the possible negative effects that nanomaterials can bring.<sup>23</sup> Nanoparticles released in the aquatic environment can be harmful to their organisms,<sup>24</sup> in soil can be toxic for earthworms<sup>25; 26</sup> and beneficial rhizosphere bacteria<sup>27</sup> which indirectly affect plants growth. On the plant level, nanoparticles can induce genotoxicity,<sup>28; 29</sup> alteration in nutritional status,<sup>30</sup> oxidative stress,<sup>29</sup> and may result in decreased plant growth and biomass.

**Table 1** - Bibliographic survey of nanoparticle seed treatment. Symbols used in the table: ↑= Increase, ↓= Decrease

Ref.	Species	Concentration (mg L <sup>-1</sup> )	Type	Size (nm)	Time of exposure	M in visual effect
21	<i>Pennisetum glaucum</i> (pearl millet)	20 and 50	Ag	13	2 h	↑ germination rate and ↓ seedlings growth
31	<i>Oryza sativa</i> L. cv. <i>KDML 105</i> (jasmine rice)	0.1, 1, 10, 100 and 1 000	Ag	20, 30 – 60, 70 – 120 and 1	24	↓ germination rate and seedlings growth
32	<i>Vigna radiata</i> L. (mung bean)	5, 10, 20 and 50	Ag	20	21 days	↓ shoot length at 50 mg L <sup>-1</sup> and ↓ root length at 20 and 50 mg L <sup>-1</sup>
33	<i>Triticum aestivum</i> L. (wheat)	1 and 10	Ag	10	4 h	↓ seedling growth at 10 mg L <sup>-1</sup>
34	<i>Arachis hypogaea</i> (peanut)	0.56, 1.12, 2.24, 4.48, 8.96 and 17.92	Fe <sup>0</sup>	20 – 80	5 days	↑ seedling growth (except at 17.92 mg L <sup>-1</sup> )
19	<i>Zea mays</i> L. (maize)	10, 100 and 1 000	ZnO	30 ± 12	2 h	↑ root elongation at 10 mg L <sup>-1</sup> and ↓ at 1 000 mg L <sup>-1</sup>
19	<i>Cucumis sativus</i> L. (cucumber)	10, 100 and 1 000	ZnO	3 ± 1	2 h	↓ root elongation
35	<i>Brassica pekinensis</i> L. (chinese cabbage)	1, 5, 10, 20, 40 and 80	ZnO	30, 50, 90 and 150	3 days	↓ seedling growth
20	<i>Abelmoschus esculentus</i> (L.) Moench (okra)	50, 100, 200 and 500	Zn	<50	24 h	↑ germination rate, ↓ shoot length and ↑ root hairs (except at 500 mg L <sup>-1</sup> )
36	<i>Pisum sativum</i> L. (green pea)	50, 100, 200, 400 and 500	CuO	30	14 days	↓ seedling growth (except for 50 mg L <sup>-1</sup> )
37	<i>Arabidopsis thaliana</i>	20 and 50	CuO	20 – 40	48 h	↓ root and shoot fresh weight
22	<i>Cucumis sativus</i> L. (cucumber)	100, 200, 400 and 600	CuO	< 100	6 h	↓ germination rate and root elongation

Advances on the interaction between environment and nanoparticles require suitable analytical techniques for qualitative-quantitative assessment. Plant mineral analysis is commonly carried out by means of spectroscopy techniques like inductively coupled plasma mass spectrometry (ICP-MS), inductively coupled plasma optical emission spectrometry (ICP-OES) and electrothermal atomic absorption spectroscopy (ET-AAS). Each of them presenting their own advantages and limitations, but they all have in common the sample preparation step as a mandatory procedure. In this operation the sample matrix is destroyed by the digestion with strong acids, which is laborious and time-consuming.

On the other hand, X-ray fluorescence spectroscopy (XRF) requires minimum or none sample preparation. This non-destructive feature property makes it a very suitable technique for plant analysis *in vivo* and even *in situ*, when acquired with handheld devices. Moreover, the multi-elemental and simultaneous capability, high throughput and low cost features make it even more attractive.

There are several variants of XRF systems. In the context of this dissertation, the use of benchtop energy dispersive X-ray fluorescence (EDXRF) and energy dispersive microprobe X-ray fluorescence ( $\mu$ -XRF) systems are highlighted. Besides providing qualitative-quantitative information,  $\mu$ -XRF is an important tool for seed studies because of its capability of elemental distribution mapping.<sup>38; 39</sup> It can be useful to investigate the mineral distribution in seeds during its development,<sup>40</sup> evaluate the elemental distribution between distinct genotypes<sup>41</sup> and patterns during germination.<sup>42</sup>

Besides XRF techniques, this dissertation also employed synchrotron-based X-ray absorption spectroscopy (XAS). XAS is widely used to determine the average local structural and chemical environment of an absorbing atom. In this method the X-ray beam scans the sample over a range of energies below and above the absorption edge of the element of interest and a spectrum is created. The absorption edge refers to a sharp increase in the absorption coefficient, which occurs when the core electron absorbs energy equal to or greater than its binding energy. The energy region of the spectrum from the absorption edge to about 50 eV above it is the X-ray absorption near-edge structure (XANES), which is used to determine the oxidation state, geometry and nature of ligands around the element of interest.<sup>43; 44</sup>

Common bean (*Phaseolus vulgaris* L.) is the most consumed food legume in the world and is the major source of dietary protein in Latin America and Eastern Africa.<sup>45</sup> Besides that, this seed was chosen as model species because it presents low dormancy, and it results in a plant of small size and short cycle, which makes it easy to be employed in laboratory studies.

## 1.1 Hypothesis

This study raised the following hypothesis:

- i) Nanoparticles (CuO and Fe<sub>3</sub>O<sub>4</sub>) can penetrate within the seeds;
- ii) Nanoparticles can enhance seed germination and seedling growth;
- iii) Nanoparticles can be biotransformed after seed soaking.

## 1.2 Objectives

The general objective of this Masters dissertation was to assess the effect of copper oxide (nCuO) and magnetite nanoparticles (nFe<sub>3</sub>O<sub>4</sub>) on the germination and seedling development of *Phaseolus vulgaris* L. Thus, a series of experiments were designed to tests the abovementioned hypothesis. Seeds were treated in a wide range of concentrations. Different sized nCuO and coated nFe<sub>3</sub>O<sub>4</sub> were evaluated.

To achieve the objectives, the biometric parameters germination rate and seedling weight gain were determined. XRF measured the Cu and Fe uptake and pointed out their storage location. X-ray absorption spectroscopy revealed the Cu and Fe chemical environment of the nCuO and nFe<sub>3</sub>O<sub>4</sub> treated seeds, while X-ray tomography showed the 3D distribution of Fe in the nFe<sub>3</sub>O<sub>4</sub> treated seeds. Radicle elongation and  $\alpha$ -amylase activity were also recorded for the nFe<sub>3</sub>O<sub>4</sub> treated seedlings.

A comprehensive nanoparticle characterization was accomplished through dynamic light scattering (DLS), X-ray diffraction (XRD), EDXRF, scanning electron microscopy (SEM) for nCuO and transmission electron microscopy (TEM) for nFe<sub>3</sub>O<sub>4</sub>.

### 1.3 Structure of the dissertation

This dissertation comprises an introductory text followed by two chapters. Each chapter comprises a manuscript published by the *Journal of Agricultural and Food Chemistry*. The original texts were adapted to comply with institutional format requirements.

Chapter 1: DURAN, N. M. et al. X-ray spectroscopy uncovering the effects of Cu based nanoparticle concentration and structure on *Phaseolus vulgaris* germination and seedling development. **Journal of Agricultural and Food Chemistry**, Washington, v. 65, n. 36, p. 7874-7884, 2017.

- Chapter 2: DURAN, N. M. et al. Bean seedling growth enhancement using magnetite nanoparticles. **Journal of Agricultural and Food Chemistry**, Washington, 2018. [Epub ahead of print].

### References

1 MARSCHNER, P. **Mineral nutrition of higher plants**. 3. ed. San Diego: Academic Press, 2012. 672 p.

2 FOX, T. C.; GUERINOT, M. L. Molecular biology of cation transport in plants. **Annual Review of Plant Physiology and Plant Molecular Biology**, Palo Alto, v. 49, p. 669-696, 1998.

3 MARSH, H. V.; EVANS, H. J.; MATRONE, G. Investigations of role of iron in chlorophyll metabolism I. Effect of iron deficiency on chlorophyll and heme content and on activities of certain enzymes in leaves. **Plant Physiology**, Rockville, v. 38, n. 6, p. 632-638, 1963.

4 BRIAT, J. F.; CURIE, C.; GAYMARD, F. Iron utilization and metabolism in plants. **Current Opinion in Plant Biology**, London, v. 10, n. 3, p. 276-282, 2007.

5 FAGERIA, N. K. et al. Foliar fertilization of crop plants. **Journal of Plant Nutrition**, New York, v. 32, n. 6, p. 1044-1064, 2009.

6 HARRIS, D. et al. 'On-farm' seed priming with zinc sulphate solution - A cost-effective way to increase the maize yields of resource-poor farmers. **Field Crops Research**, Amsterdam, v. 102, n. 2, p. 119-127, 2007.

7 MCDONALD, M. B. Seed priming. In: BLACK, M.; BEWLEY, J. D. (Ed.). **Seed technology and its biological basis**. 1. ed. Sheffield: Sheffield Academic Press, 2000. chap. 9, p. 287-325.

- 8 SHARMA, A. D. et al. Comparison of various seed priming methods for seed germination, seedling vigour and fruit yield in okra (*Abelmoschus esculentus* L. Moench). **Scientia Horticulturae**, Amsterdam, v. 165, p. 75-81, 2014.
- 9 BEWLEY, J. D. Seed germination and dormancy. **Plant Cell**, Rockville, v. 9, n. 7, p. 1055-1066, 1997.
- 10 BRADBEER, J. W. **Seed dormancy and germination**. 1. ed. Glasgow: Blackie, 1988. 146 p.
- 11 AUFFAN, M. et al. Towards a definition of inorganic nanoparticles from an environmental, health and safety perspective. **Nature Nanotechnology**, London, v. 4, n. 10, p. 634-641, 2009.
- 12 GUO, D.; XIE, G. X.; LUO, J. B. Mechanical properties of nanoparticles: basics and applications. **Journal of Physics D: Applied Physics**, London, v. 47, n. 1, p. 25, 2014. DOI:10.1088/0022-3727/47/1/013001.
- 13 KHLEBTSOV, N. G.; DYKMAN, L. A. Optical properties and biomedical applications of plasmonic nanoparticles. **Journal of Quantitative Spectroscopy & Radiative Transfer**, Oxford, v. 111, n. 1, p. 1-35, 2010.
- 14 DREIZIN, E. L. Metal-based reactive nanomaterials. **Progress in Energy and Combustion Science**, Oxford, v. 35, n. 2, p. 141-167, 2009.
- 15 EL BADAWEY, A. M. et al. Surface charge-dependent toxicity of silver nanoparticles. **Environmental Science & Technology**, Washington, DC, v. 45, n. 1, p. 283-287, 2011.
- 16 FAIVRE, D.; BENNET, M. Magnetic nanoparticles line up. **Nature**, London, v. 535, n. 7611, p. 235-236, 2016.
- 17 LEE, S. et al. Measuring thermal conductivity of fluids containing oxide nanoparticles. **Journal of Heat Transfer-Transactions of the Asme**, New York, v. 121, n. 2, p. 280-289, 1999.
- 18 MUDUNKOTUWA, I. A. et al. Dissolution of ZnO nanoparticles at circumneutral pH: A study of size effects in the presence and absence of citric acid. **Langmuir**, Washington, DC, v. 28, n. 1, p. 396-403, 2012.
- 19 ZHANG, R. C. et al. Phytotoxicity of ZnO nanoparticles and the released Zn(II) ion to corn (*Zea mays* L.) and cucumber (*Cucumis sativus* L.) during germination. **Environmental Science and Pollution Research**, Landsberg, v. 22, n. 14, p. 11109-11117, 2015.
- 20 GOKAK, I. B.; TARANATH, T. C. Morphological and biochemical responses of *Abelmoschus esculantus* (L.) Moench to zinc nanoparticles. **Advances in Natural Sciences-Nanoscience and Nanotechnology**, Bristol, v. 6, n. 2, 5 p. 2015. DOI:10.1088/2043-6262/6/2/025017.
- 21 PARVEEN, A.; RAO, S. Effect of nanosilver on seed germination and seedling growth in *Pennisetum glaucum*. **Journal of Cluster Science**, New York, v. 26, n. 3, p. 693-701, 2015.

- 22 MOON, Y. S. et al. SELDI-TOF MS-based discovery of a biomarker in *Cucumis sativus* seeds exposed to CuO nanoparticles. **Environmental Toxicology and Pharmacology**, Amsterdam, v. 38, n. 3, p. 922-931, 2014.
- 23 SAJID, M. et al. Impact of nanoparticles on human and environment: review of toxicity factors, exposures, control strategies, and future prospects. **Environmental Science and Pollution Research**, Landsberg, v. 22, n. 6, p. 4122-4143, 2015.
- 24 BLINOVA, I. et al. Toxicity of two types of silver nanoparticles to aquatic crustaceans *Daphnia magna* and *Thamnocephalus platyurus*. **Environmental Science and Pollution Research**, Landsberg, v. 20, n. 5, p. 3456-3463, 2013.
- 25 VAN DER PLOEG, M. J. C. et al. Effects of silver nanoparticles (NM-300K) on *Lumbricus rubellus* earthworms and particle characterization in relevant test matrices including soil. **Environmental Toxicology and Chemistry**, Hoboken, v. 33, n. 4, p. 743-752, 2014.
- 26 JESMER, A. H. et al. The toxicity of silver to soil organisms exposed to silver nanoparticles and silver nitrate in biosolids-amended field soil. **Environmental Toxicology and Chemistry**, Hoboken, v. 36, n. 10, p. 2756-2765, 2017.
- 27 GUPTA, I. R.; ANDERSON, A. J.; RAI, M. Toxicity of fungal-generated silver nanoparticles to soil-inhabiting *Pseudomonas putida* KT2440, a rhizospheric bacterium responsible for plant protection and bioremediation. **Journal of Hazardous Materials**, Amsterdam, v. 286, p. 48-54, 2015.
- 28 GOLBAMAKI, N. et al. Genotoxicity of metal oxide nanomaterials: review of recent data and discussion of possible mechanisms. **Nanoscale**, Cambridge, v. 7, n. 6, p. 2154-2198, 2015.
- 29 MANNA, I.; BANDYOPADHYAY, M. Engineered nickel oxide nanoparticles affect genome stability in *Allium cepa* (L.). **Plant Physiology and Biochemistry**, Amsterdam, v. 121, p. 206-215, 2017.
- 30 LI, X. G. et al. Bt-transgenic cotton is more sensitive to CeO<sub>2</sub> nanoparticles than its parental non-transgenic cotton. **Journal of Hazardous Materials**, Amsterdam, v. 274, p. 173-180, 2014.
- 31 THUESOMBAT, P. et al. Effect of silver nanoparticles on rice (*Oryza sativa* L. cv. KDML 105) seed germination and seedling growth. **Ecotoxicology and Environmental Safety**, Amsterdam, v. 104, p. 302-309, 2014.
- 32 NAIR, P. M. G.; CHUNG, I. M. Physiological and molecular level studies on the toxicity of silver nanoparticles in germinating seedlings of mung bean (*Vigna radiata* L.). **Acta Physiologiae Plantarum**, Warszawa, v. 37, n. 1, p. 1719, 2015.
- 33 VANNINI, C. et al. Phytotoxic and genotoxic effects of silver nanoparticles exposure on germinating wheat seedlings. **Journal of Plant Physiology**, Jena, v. 171, n. 13, p. 1142-1148, 2014.

- 34 LI, X. et al. Stimulation of peanut seedling development and growth by zero-valent iron nanoparticles at low concentrations. **Plos One**, San Francisco, v. 10, n. 4, p. 1-12, 2015.
- 35 XIANG, L. et al. Effects of the size and morphology of zinc oxide nanoparticles on the germination of Chinese cabbage seeds. **Environmental Science and Pollution Research**, Landsberg, v. 22, n. 14, p. 10452-10462, 2015.
- 36 NAIR, P. M. G.; CHUNG, I. M. The responses of germinating seedlings of green peas to copper oxide nanoparticles. **Biologia Plantarum**, Praha, v. 59, n. 3, p. 591-595, 2015.
- 37 WANG, Z. Y. et al. CuO Nanoparticle Interaction with *Arabidopsis thaliana*: Toxicity, Parent-Progeny Transfer, and Gene Expression. **Environmental Science & Technology**, Washington, DC, v. 50, n. 11, p. 6008-6016, 2016.
- 38 AJIBOYE, B. et al. X-ray fluorescence microscopy of zinc localization in wheat grains biofortified through foliar zinc applications at different growth stages under field conditions. **Plant and Soil**, Dordrecht, v. 392, n. 1-2, p. 357-370, 2015.
- 39 KYRIACOU, B. et al. Localization of iron in rice grain using synchrotron X-ray fluorescence microscopy and high resolution secondary ion mass spectrometry. **Journal of Cereal Science**, London, v. 59, n. 2, p. 173-180, 2014.
- 40 IWAI, T. et al. Dynamic changes in the distribution of minerals in relation to phytic acid accumulation during rice seed development. **Plant Physiology**, Rockville, v. 160, n. 4, p. 2007-2014, 2012.
- 41 SINGH, S. P. et al. Pattern of iron distribution in maternal and filial tissues in wheat grains with contrasting levels of iron. **Journal of Experimental Botany**, Oxford, v. 64, n. 11, p. 3249-3260, 2013.
- 42 LU, L. L. et al. Analysis of metal element distributions in rice (*Oryza sativa* L.) seeds and relocation during germination based on X-Ray fluorescence imaging of Zn, Fe, K, Ca, and Mn. **Plos One**, San Francisco, v. 8, n. 2, p. 9, 2013.
- 43 CHAURAND, P. et al. Environmental impacts of steel slag reused in road construction: A crystallographic and molecular (XANES) approach. **Journal of Hazardous Materials**, Amsterdam, v. 139, n. 3, p. 537-542, 2007.
- 44 WU, P. W. et al. Applications of Synchrotron-Based Spectroscopic Techniques in Studying Nucleic Acids and Nucleic Acid-Functionalized Nanomaterials. **Advanced Materials**, Weinheim, v. 26, n. 46, p. 7849-7872, 2014.
- 45 GRAHAM, P. H.; RANALLI, P. Common bean (*Phaseolus vulgaris* L). **Field Crops Research**, Amsterdam, v. 53, n. 1-3, p. 131-146, 1997.



## 2 X-RAY SPECTROSCOPY UNCOVERING THE EFFECTS OF CU BASED NANOPARTICLE CONCENTRATION AND STRUCTURE ON *PHASEOLUS VULGARIS* GERMINATION AND SEEDLING DEVELOPMENT

### Abstract

Nanoparticles properties such as solubility, tunable surface charges, and singular reactivity might be explored to improve the performance of fertilizers. Nevertheless, these unique properties may also bring risks to the environment since the fate of nanoparticles is poorly understood. This study investigated the impact of a range of CuO nanoparticles sizes and concentrations on the germination and seedling development of *Phaseolus vulgaris* L. Nanoparticles did not affect seed germination, but seedling weight gain was promoted by 40 nm CuO at 100 mg Cu L<sup>-1</sup> and inhibited by 1 000 mg Cu L<sup>-1</sup> of 25 nm CuO and CuSO<sub>4</sub>. Most of the Cu taken up remained in the seed coat with Cu hotspots in the hilum. X-ray absorption spectroscopy unraveled that most of the Cu remained in its pristine form. The higher surface reactivity of the 25 nm CuO nanoparticles might be responsible for its deleterious effects. The present study therefore highlights the importance of the nanoparticle structure for its physiological impacts.

**Keywords:** *Phaseolus vulgaris* L. CuO nanoparticle. Germination. X-ray based spectroscopy.

## 2.1 Introduction

In the past few years, a wide range of engineered nanoparticles, with unique physicochemical properties, has been launched on the market and consequently to the environment. Such properties make these materials suitable for applications that substantially differ from those of the usual bulk form. The nanoscale particle size of these materials increases the surface to volume ratio, thus an important fraction of the atoms lies on the surface. These surface atoms have different properties than those in bulk, thus affecting their solubility, light scattering and absorbance, conductivity, melting point, and catalytic properties.<sup>1</sup> Being present also in many daily life goods, nanoparticles can easily be released into the environment and reach the entire food chain. This possibility, which may result in toxicological effects on consumers,<sup>2</sup> remains so far uncertain and has been a matter of intense debate in recent years.

The development of nanotechnologies tailored for agricultural purposes can result in a more rational use of pesticides, biocides, and fertilizers,<sup>3;4</sup> potentially reducing the usage of these hazardous products in agricultural practices. Such innovations could lead to cost reduction, less nutrient leaching, and preservation of the desirable soil microbiota. In this context, we highlight the possibility of employing nanotechnology for seed coating.<sup>5</sup> Seed coating is an attractive way for micronutrient delivery. It has the potential to improve seedling growth and crop productivity<sup>6</sup> while treated seeds generally germinate faster and more synchronized than nontreated seeds.<sup>7</sup> Compared to soil fertilization, seed treatment is an easier and cost-effective way requiring a lower quantity of nutrients.<sup>6</sup> A significant yield increase was observed when wheat seeds were treated with a low dose of Cu-EDTA ( $0.04 \text{ kg ha}^{-1}$ ).<sup>8</sup>

The uptake of nanoparticles by plants occurs not only through the root system<sup>9</sup> but also via leaves<sup>10</sup> and seeds.<sup>11</sup> Studies regarding the effects of the interaction between nanoparticles and plants are not consensual. While some studies show that nano ZnO promoted root elongation in peanut<sup>12</sup> and soybean,<sup>13</sup> others showed similar results of nano CeO<sub>2</sub> treatments on coriander,<sup>14</sup> corn, and cucumber,<sup>15</sup> while studies on tobacco<sup>16</sup> and basil<sup>17</sup> showed detrimental effects on germination and growth upon exposure to nano TiO<sub>2</sub>.

The effects of nanoparticle exposure do not only vary with the plant species, they also depend on the chemical composition, reactivity, size, and morphology of the particles as well as on aggregation state, applied concentration, and experimental conditions. Inside living cells,

they can influence crucial processes like oxidative balance, genomic, proteomic, and metabolomic. The nanoparticles can be internalized by endocytosis, and depending on their nature, can be located in different types of organelles. The entrance is controlled by biological and physicochemical attributes such as the cell type, surface chemistry and charge, size, shape, and mechanical properties of the nanoparticles.<sup>18</sup>

Specifically regarding the interaction between nanoparticles and seeds, the literature is still scarce. Depending on nanoparticle size, composition, and concentration, germination and root elongation can be either favored or reduced. Studies on Cu-based nanoparticles are even scarcer.

Nanometric copper is broadly used in catalysts, coatings, electronic components, medicines, and lubricant compounds.<sup>19</sup> It means that regardless of their potential application for seed treatment, copper-based nanoparticles will ultimately reach the environment and end up interacting with plants. Therefore, we must investigate and understand how these nanoparticles affect seed germination and seedling development. Albeit found only as a trace element in many plant tissues, copper is considered essential for vegetal life, being a transition metal involved in several metabolic processes like photosynthesis, mitochondrial respiration, oxidative stress protection, and protein synthesis.<sup>20</sup> Nonetheless, most reports in the literature show an increased toxicity in plants exposed to copper nanoparticles. These reports emphasize an inhibitory effect on seedling growth in different species such as black mustard,<sup>21</sup> green peas,<sup>22</sup> mung beans, and wheat.<sup>11</sup>

The present study aimed at investigating the effect of commercial Cu-based nanoparticles, used for seed priming, on the germination and seedling development of *Phaseolus vulgaris*, also known as common bean or kidney bean. In order to verify their potential use as seed fertilizer and the possible high doses impairments, we evaluated the impact of three nanoparticle sizes (25, 40, and <80 nm) at four concentrations (1, 10, 100 and 1000 mg Cu L<sup>-1</sup>). Besides monitoring biometric parameters such as germination rate and seedling weight gain, a comprehensive characterization was carried out using X-ray fluorescence (XRF) and X-ray absorption spectroscopy (XAS) seeking to trace the Cu uptake, storage location, and biotransformation.

## 2.2 Materials and Methods

### 2.2.1 Characterization of pristine CuO nanoparticles and dispersions

Copper oxide and passivated CuO nanoparticles (herein all referred as nCuO) were purchased from US Nanomaterials Research Inc. (USA), in three different sizes: 25, 40, and <80 nm. Copper sulfate ( $\text{CuSO}_4 \cdot 5\text{H}_2\text{O}$ ) was purchased from MERCK KGaA (Germany) and used as a copper ionic reference treatment.

The purity of each nCuO was determined by energy dispersive X-ray fluorescence spectroscopy (EDXRF; EDX-720 Shimadzu, Japan). Two hundred milligrams of pristine powders were weighted in a 6.3 mm aperture X-ray fluorescence spectroscopy (XRF) sample cup (no. 3577 - Spex Ind. Inc., USA) sealed with a 5  $\mu\text{m}$  thick polypropylene film (no. 3520 - Spex Ind. Inc., USA). The samples were analyzed under vacuum, in triplicate, using a rhodium (Rh) X-ray tube at 50 kV and auto-tunable current adjusted for a detector deadtime below 30% and a 3-mm collimator. The X-ray spectrum of the sample was acquired utilizing a Si (Li) detector for 300 s. The quantification was carried out using the fundamental parameters method.

The crystal structure of the nCuO was determined by X-ray diffraction (XRD) employing a PW 1877 diffractometer (Philips, The Netherlands) with  $\text{Cu-K}\alpha$  radiation. Using the peak width it was possible to estimate the crystallite size by the Scherrer equation:

$$D_{(hkl)} = K\lambda / \beta \cos\theta$$

where  $D$  is the mean crystal size of the nanoparticles,  $K$  the Scherrer constant (0.94 for spherical crystals with cubic symmetry),  $\lambda$  the wavelength of light used for the diffraction (0.154184 nm to Cu),  $\beta$  the full width at half maximum of the peak, and  $\theta$  refers to the angle measured.

Nanoparticle morphology was evaluated by scanning electron microscopy (SEM; Inspect F50, FEI Company, USA) at the Brazilian Nanotechnology National Laboratory (LNNano, Campinas, Brazil). The CuO nanoparticles were suspended in deionized water and dispersed using an ultrasonic processor (model 705 Sonic Dismembrator, Fisher Scientific, USA) under 50% amplitude for 8 min at 1, 10, 100, and 1 000  $\text{mg Cu L}^{-1}$ . The hydrodynamic size and the zeta potential were analyzed by dynamic light scattering (DLS; Zetasizer Nano, Malvern Instruments, U.K.) at the Brazilian Biosciences National Laboratory (LNBio, Campinas, Brazil).

### 2.2.2 Germination assay

*Phaseolus vulgaris* seeds, variety BRS Cometa, were supplied by the Brazilian Agricultural Research Corporation (EMBRAPA), having an average germination rate of 88%.

Seeds were first immersed in a 10% NaClO solution under stirring for 10 s for disinfection, followed by rinsing with deionized water. Subsequently, 20 seeds were soaked for 20 min in the appropriate concentration of each nCuO size. CuSO<sub>4</sub>·5H<sub>2</sub>O solutions at the same concentrations were used as a positive control, whereas deionized water was used as a negative control. After the exposure, the seeds were placed on a 15 cm paper filter fit on the bottom of a Petri dish, and 8 mL of the soaking solution was added for moisturizing the paper filter. The Petri dishes were sealed with Parafilm M (Bemis Company Inc., USA), inserted into a plastic bag for preventing water loss, and finally incubated in a germination chamber (TE-4020, Tecnal, BR) under dark and ventilation at 27 °C for 5 days. The experiment was conducted in quadruplicate per treatment.

The number of germinated seeds was counted daily to determine the rate of germination. After 5 days, the assay was completed. Fresh mass was measured and the germinated seeds were rinsed in deionized water to remove the surface-bound metal or nano metal oxide and then dried in a laboratory oven (515/4A, FANEM, Brazil) at 60 °C for 2 days to obtain the dry mass.

### 2.2.3 Copper uptake quantification

Dried seedlings were carefully separated in two fractions: seedling and seed coat. One gram of each component was weighted in a previously decontaminated porcelain crucible and then digested by dry ashing method using a muffle furnace (F-2, Fornitec, Brazil) at 100 °C h<sup>-1</sup> ramp rate up to 550 °C and ashed for 14 h. Each dry ashing digestion batch included a blank for ensuring no contamination. The ashes were dissolved in 5 mL of 1 M HNO<sub>3</sub>(aq), and 950 µL of this solution was transferred into a 1.5 mL vial and 50 µL of 1 000 mg Ga L<sup>-1</sup> was added as an internal standard. Then, the sample was homogenized using a tube shaker vortex (MA162, Marconi, Brazil).

The Cu content of the digested samples was determined by EDXRF. Fifteen milliliters of the digests were pipetted into the external side window of the 6.3 mm aperture XRF sample cup (no. 3577 - Spex Ind. Inc., USA) sealed with 5 µm thickness polypropylene film (no. 3520 - Spex Ind. Inc., USA) and dried at 60°C in a laboratory oven. This procedure was

carried out twice. The samples were analyzed in triplicate using a rhodium (Rh) X-ray tube at 50 kV and auto-tunable current with a deadtime at 30% and a 3-mm collimator. The X-ray spectrum of the sample was acquired utilizing a Si (Li) detector for 200 s. The quantification was performed using external standard calibration. The recovery of this method was assessed spiking the sample with 1 000 mg Cu L<sup>-1</sup> before the dry ashing step.

#### **2.2.4 nCuO solubility**

To verify the Cu solubility of each nCuO powder, 50 mL of nCuO aqueous dispersions were prepared at 100 and 1 000 mg Cu L<sup>-1</sup> using a probe ultrasonic device (Fisher Scientific™ Model 705 Sonic Dismembrator). The equipment was operated at 95 W (amplitude of 50 %) and 50 J, during 4 x 5 min with an interval of 3 min between each cycle. After 24 hours, one milliliter of each dispersion was transferred to Eppendorf™ vials and then centrifuged by a microcentrifuge (Mikro 120, Hettich, Germany) for 60 minutes at 13 000 rpm.

Quantitative analysis of the supernatants was performed by EDXRF using Ga as internal standard. The analysis parameters and experimental setup were the same as above mentioned (copper uptake quantification).

#### **2.2.5 Mapping the Cu accumulation spots**

The seeds were exposed to 25 and 80 nm nCuO dispersions at 1 000 mg Cu L<sup>-1</sup> and 40 nm nCuO at 5 000 mg Cu L<sup>-1</sup> for 20 min, dried at room temperature, and gently cut in the middle using a stainless steel blade. Subsequently, the seed was placed in a sample holder with a poly(amide) tape and the cotyledon's inner side exposed for analysis. Chemical images of the primary root were also recorded at the third, fourth, and fifth day germination. For the latter measurements, the same germination assay procedure was followed, but only the higher nCuO concentration (1 000 mg Cu L<sup>-1</sup>) treatment and copper sulfate (positive control) were analyzed, except for the 40 nm nCuO treatment which seeds were soaked in 100 mg Cu L<sup>-1</sup>.

The microanalysis was carried out using benchtop microprobe X-ray fluorescence system (Orbis PC EDAX, USA) operating with a Rh X-ray tube at 40 kV and 300 μA. The sample was interrogated with a 30 μm X-ray beam spot size provided by a polycapillary optic. The detection was carried out by a 30 mm<sup>2</sup> silicon drift detector (140 eV FWHM at the 5.9 keV Mn-Kα line) with a deadtime of nearly 3%. Seed maps were registered using a matrix

of 64x50 points (number of analyzed points on xy-axes) and dwell time per pixel of 1 s. For the primary roots, a matrix of 32x25 points and 500  $\mu$ s of dwell time were selected.

### 2.2.6 Copper chemical speciation analysis

Sample preparation for determining copper speciation by micro-X-ray absorption near-edge structure ( $\mu$ -XANES) analysis was the same as used for  $\mu$ -XRF analysis, but the seeds only received the 1 000 mg Cu L<sup>-1</sup> dispersion treatment. After drying, the samples were stored in sealed Petri dishes 10 days prior analysis. The analysis was accomplished using  $\mu$ -XANES at the D09B-XRF beamline at the 1.37 GeV Brazilian Synchrotron Light Laboratory (LNLS, Campinas, Brazil).

At XRF beamline, synchrotron radiation was generated by a bending-magnet and collimated by slits. The monochromatic beam was produced by a Si(111) crystal and a KB mirror system was used to focus it to the 20  $\mu$ m diameter spot size. The  $\mu$ -XANES spectra were recorded in fluorescence mode using a silicon drift detector (SDD; AXAS-A, KETEK GmbH, Germany). The energy was calibrated utilizing a reference Cu foil.

The chemical maps, previously provided by  $\mu$ -XRF analysis, aided selecting the proper seed region for  $\mu$ -XANES analysis according to the Cu accumulation spots after the nCuO exposure. The  $\mu$ -XRF maps identified three different regions for speciation studies: outside seed coat, within seed coat, and cotyledon near seed coat.

In order to improve the signal-to-noise ratio, five XANES spectra were recorded and merged in each sample region. Sixteen reference Cu compounds were previously synthesized in our laboratory according to Sarret et al.<sup>23</sup> and measured for providing the model spectra. The  $\mu$ -XANES spectra were normalized and subjected to linear combination fitting (LCF) analysis using the Athena software of the IFEFFIT package.<sup>24</sup> The uncertainties stated for the weighted compounds correspond to 1 $\sigma$  standard errors.

### 2.2.7 Root microscopic analysis

To determine the exact tissue of Cu accumulation in root samples, seedlings were cleared in a solution of 2.5% commercial bleach in deionized water for 24 h and rinsed in deionized water five times. Roots were cut from the rest of the seedling and mounted on glass slides with 50% glycerol. Images were taken on a Zeiss AxioVert 35 microscope coupled with a Zeiss AxioCam ICc 3 digital camera in brightfield conditions.

### 2.2.8 Surface reactivity of CuO nanoparticles

The reactivity of the CuO nanoparticles was evaluated measuring its ability to decompose  $\text{H}_2\text{O}_2$  through a Fenton-like reaction.<sup>25</sup> In a 25 mL round-bottom reaction flask, 19.5 mL of a 1 000 mg  $\text{Cu L}^{-1}$  aqueous dispersion of the tested nanoparticle was magnetically stirred. The flask was connected to a 25 mL graduated pipet through a silicone tube. The pipet was immersed in a measuring cylinder water column. Then, 0.5 mL of 30% v/v  $\text{H}_2\text{O}_2$  solution was inserted in the reaction flask with a syringe. The volume of the produced  $\text{O}_2$  was monitored by following the shift of a water column in a pipet. The procedure was carried out twice. In addition to the CuO nanoparticles, also the  $\text{O}_2$  evolution by  $\text{CuSO}_4$  was determined.

### 2.2.9 Statistical analysis

The number of germinated seeds and the weight data were submitted to analysis of variance (ANOVA) and Tukey's multiple range tests at 95% confidence interval using the Action Stat software (version 3.3.111.1178, Estatcamp, BR).

## 2.3 Results and Discussion

### 2.3.1 Characterization of the nanoparticles and dispersions

The purity of the nanoparticles as evaluated by EDXRF was above 99.6% for all nanoparticles (Table 2.1). The contaminants found were Cr, Ca, and Sn and their concentrations ranged from hundreds to thousands  $\text{mg kg}^{-1}$ . XRD patterns, presented in Figure 2.1, showed that crystalline phases present in the 40 and 80 nm particles corresponded to CuO in the monoclinic phase. For the 25 nm particles, besides the standard diffraction peaks attributed to CuO the XRD pattern also revealed the presence of face centered cubic metallic Cu as informed by the supplier. The crystallite size in the direction of the plane 111 of the oxidic phase was 3.91, 23, and 21 nm for the 25, 40, and 80 nm CuO nanoparticles, respectively. The crystallite size in the 111 direction for the metallic fraction of the 25 nm particles was 5.21 nm (see Table 2.2). The particle sizes measured by SEM were in agreement with those reported by the supplier (Figure 2.2).

Table 2.1 - Degree of purity of each nCuO used in this study and concentrations of contaminants found

CuO size (nm)	Purity (%)	Contaminants (mg kg <sup>-1</sup> )		
		Cr	Ca	Sn
25	100%	---	---	---
40	>99.9%	418	---	---
<80	>99.6%	---	1764	2095

Figure 2.1 - XRD patterns for 25, 40 and <80 nm nCuO. The data shows that the 25 and 40 nm particles are CuO, whereas the 25 nm particles contain a mixture of CuO and metallic Cu

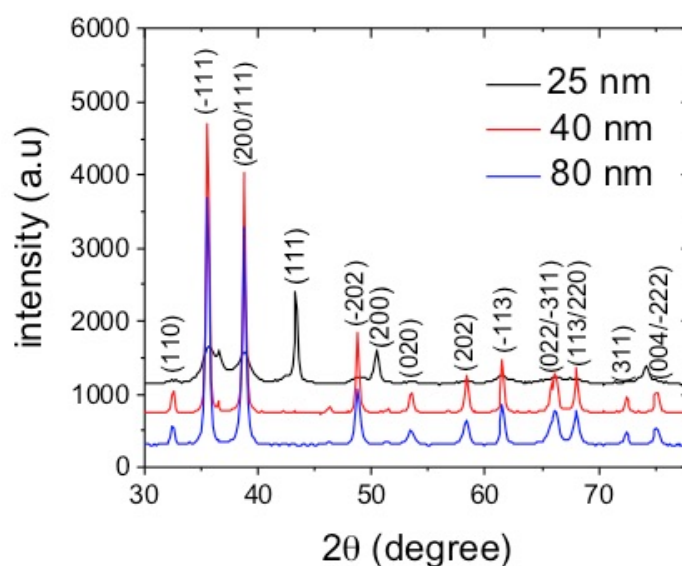
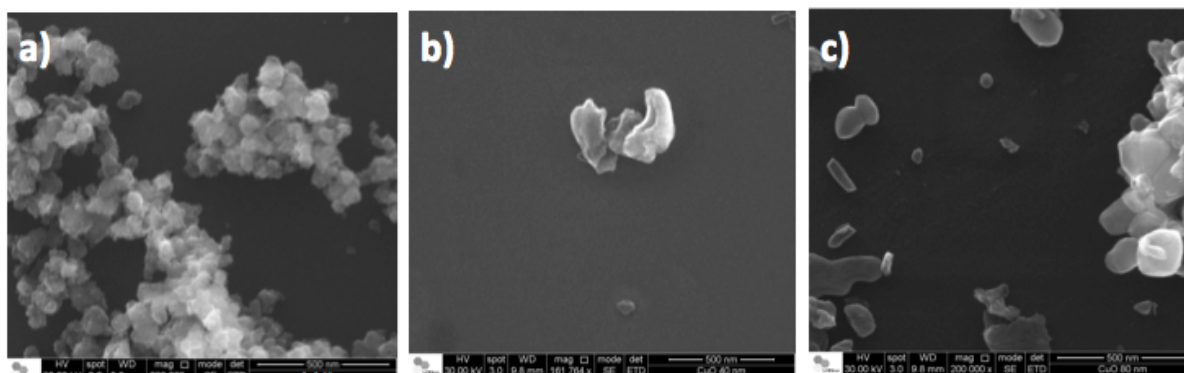


Table 2.2 - Crystallite size (D) of nCuO (25, 40 and 80 nm) in different planes

Plane (oxidic)	D <sub>(hkl)</sub> (nm)		
	CuO 25 nm	CuO 40 nm	CuO 80 nm
-111	---	41.40	32.2
111	3.91	23.00	21.00
-202	---	23.75	17.05
Plane (metallic)	CuO 25 nm	CuO 40 nm	CuO 80 nm
111	5.21	---	---
200	6.47	---	---

Figure 2.2 - Size and morphology of bulk nCuO observed by scanning electron microscopy (SEM; scale bar: 500 nm). (a) CuO 25 nm; (b) CuO 40 nm and (c) CuO <80 nm



The stability of the nCuO aqueous dispersions used for seed treatments was evaluated by DLS and zeta-potential (Table 2.3). These nanoparticles were dispersed without any surfactants, and primary particle agglomeration was observed with average hydrodynamic diameters of 428, 180, and 273 nm for 25, 40, and 80 nm nCuO, respectively. Measurements showed that these particles presented negative zeta-potentials regardless the size, with values of  $-21 \pm 5$ ,  $-15 \pm 6$ , and  $-25 \pm 7$  mV for 25, 40, and 80 nm nCuO, respectively. The literature reported similar values for 20–200 nm nCuO water dispersions, for which a hydrodynamic diameter of 480 nm and a zeta potential of  $-21 \pm 2$  mV were found.<sup>26</sup>

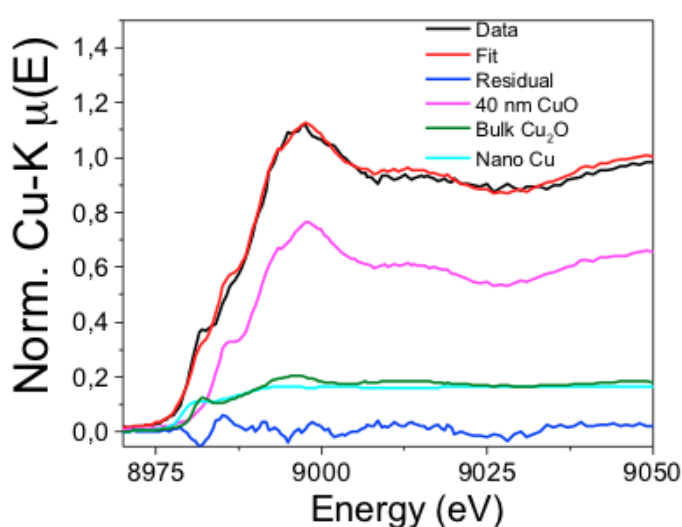
Table 2.3 - Zeta potential and hydrodynamic diameter of the nCuO (25, 40 and 80 nm) dispersions determined by Dynamic Light Scattering (DLS)

Nominal size (nm)	Zeta-potential (mV)	Hydrodynamic diameter (nm)	
		Peak 1	Peak 2
25	$-21 \pm 5$	428 (98.1%)	5 477 (1.9%)
40	$-15 \pm 6$	180 (100%)	---
80	$-25 \pm 7$	273 (100%)	---

X-ray absorption spectroscopy (XAS) measurements for the pristine 25 nm nCuO showed that this nanoparticle contained metallic Cu, Cu<sub>2</sub>O, and CuO, as shown in Figure 2.3. The linear combination analysis of the XANES spectra revealed the following proportion: CuO ( $65 \pm 2\%$ ), Cu<sub>2</sub>O ( $18 \pm 4\%$ ), and Cu ( $17 \pm 10\%$ ). The XRD input and XAS analysis

allowed us to conclude that the structure of the 25 nm nCuO consisted of a metallic core made of Cu covered by oxidized layers of Cu<sub>2</sub>O and CuO. Therefore, the results obtained for the 25 nm nCuO may not only be a consequence of their size but may also be influenced by the chemical composition of its core. One should keep in mind that the core properties can affect the surface of the material.

Figure 2.3 - Linear combination fit for Cu-K edge XAS spectra recorded for the 25 nm CuO based nanomaterial. The 25 nm CuO nanoparticle was a mixture of CuO (65 ± 2 %), Cu<sub>2</sub>O (18 ± 4%) and Cu (17 ± 10%) R-factor= 0.31%.



### 2.3.2 Effects of nCuO on seed germination and seedling growth

Figure 2.4 shows the root development on the fifth day after the seeds were exposed to the Cu treatments. Qualitative measurements of growth parameters pointed out that 1 and 10 mg Cu L<sup>-1</sup> nCuO promoted root elongation in comparison to the water control. Root elongation inhibition was noticed from 100 mg Cu L<sup>-1</sup> nCuO upward. The only exception was the 100 mg Cu L<sup>-1</sup> treatment with 40 nm nCuO that did not affect root elongation.

Figure 2.4 - Morphological characteristics of germinated *P. vulgaris* seeds soaked in (a) 25 nm, (b) 40 nm, (c) <80 nm CuO nanoparticles, and (d) CuSO<sub>4</sub>. Concentrations of the treatments varied from 1 to 1 000 mg Cu L<sup>-1</sup>

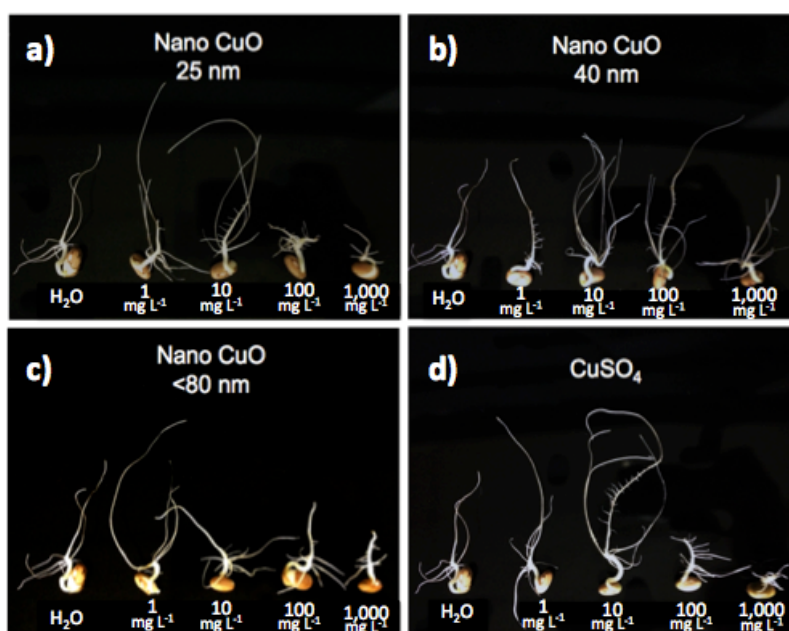


Figure 2.5 presents both (a) germination rate and (b) fresh mass gain on 5<sup>th</sup> day after germination. For the water control, the average germination rate was 80%. All the nCuO treated seeds had higher or comparable values compared to the negative control, except for the 40 nm nCuO treatment at 1 mg Cu L<sup>-1</sup> that had only 70% germination. The highest and the lowest germination rates were found for the CuSO<sub>4</sub> treatments at 100 (92.5%) and 1 000 mg Cu L<sup>-1</sup> (65%), respectively.

Figure 2.5b displays the fresh weight gain in a 2D plot as a function of the concentration of Cu in the dispersion and particle size. For the negative control (water), we considered zero entry values for particle size and concentration. For the positive control (CuSO<sub>4</sub>), we considered a size of 0.8 nm based on the diameter of CuSO<sub>4</sub> molecule<sup>27</sup> and the several concentrations employed in the test.

The 2D plot interpolates sizes and concentrations revealing the trends between the actual tested points. Figure 2.5b shows that on the fifth day of the germination assay, some treatments tended to promote fresh mass gain (reddish areas) whereas others tended to prevent it (bluish areas). Seeds exposed to 80 and 40 nm nCuO at 1 and 100 mg Cu L<sup>-1</sup>, respectively, had the highest mass gain. The 25 nm CuO nanoparticles were deleterious at 100 and 1 000 mg Cu L<sup>-1</sup>, while the <80 nm nCuO and CuSO<sub>4</sub> reduced seedling development at

1 000 mg Cu L<sup>-1</sup>. The difference between the higher and lower mass gain was statistically significant according to the Tukey test ( $p < 0.05$ ). Figure 2.6 shows that low concentrations and higher particle size improved mass gain whereas higher concentrations regardless of the particle size, including CuSO<sub>4</sub>, reduced the mass gain. A similar trend was found for the dry mass (data not shown here).

Figure 2.5 - (a) Germination rate and (b) fresh mass gain of *P. vulgaris* seeds exposed to 25, 40, <80 nm CuO nanoparticles, CuSO<sub>4</sub> (1–1 000 mg Cu L<sup>-1</sup>), and H<sub>2</sub>O (control) after 5 days of germination

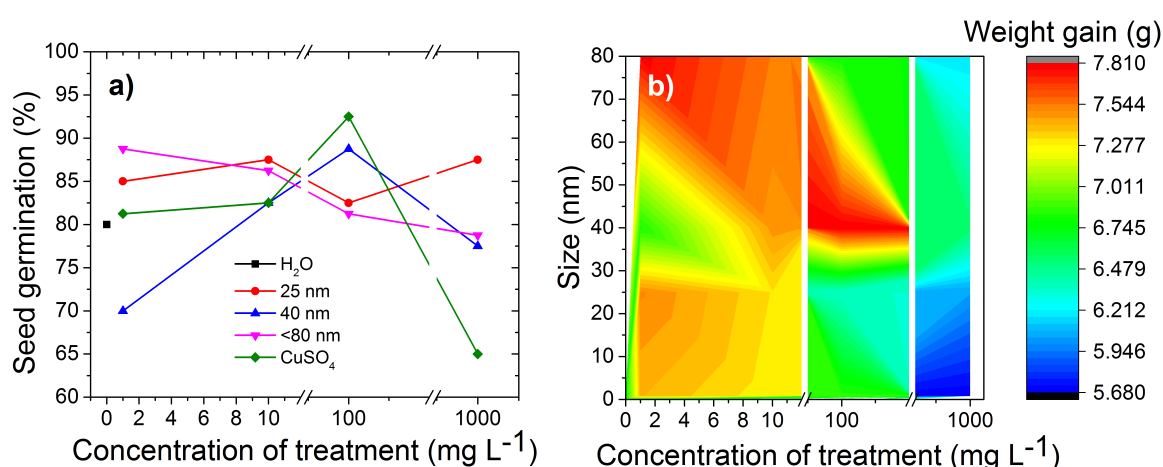
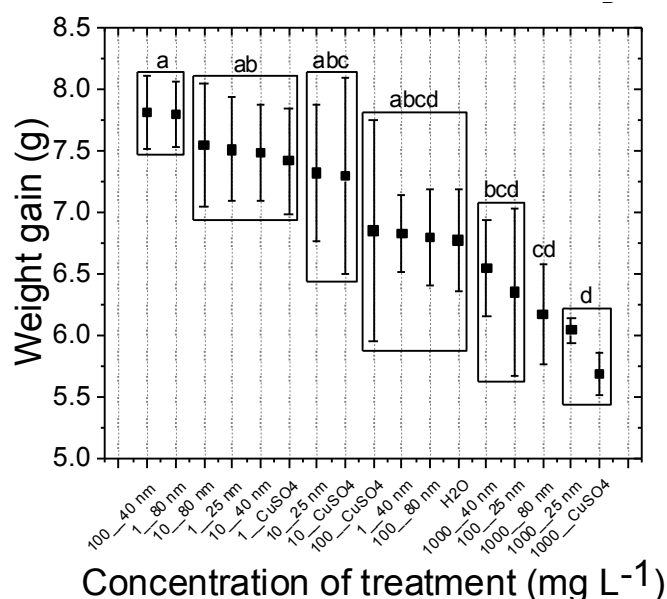
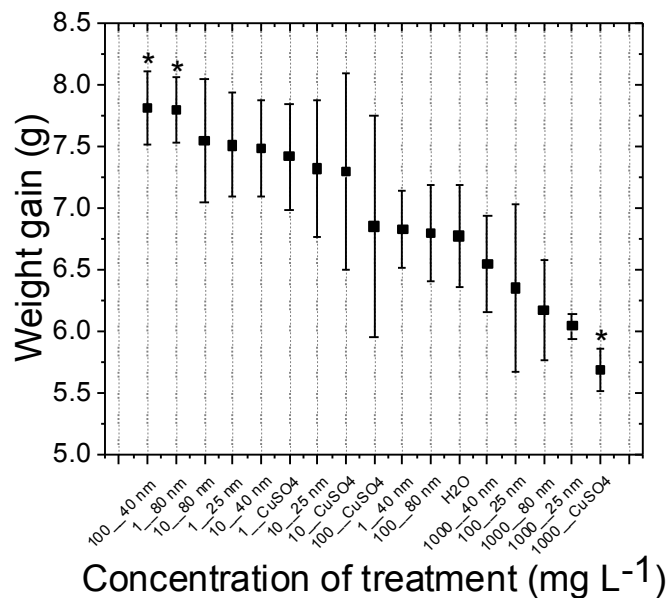


Figure 2.6 - Weight gain of *P. vulgaris* seeds as function of the concentration of nCuO and CuSO<sub>4</sub> (in mg Cu L<sup>-1</sup>). The data points followed by the same letter were significantly different according to the Tukey test at  $p < 0.05$



The mass gain test suggested a hormetic behavior for 40 nm CuO particles reaching the maximum beneficial effect at 100 mg Cu L<sup>-1</sup>. According to the Dunnett's test, mass gain was significantly different from the control at 100 mg Cu L<sup>-1</sup> of 40 nm nCuO and for CuSO<sub>4</sub> at 1 000 mg Cu L<sup>-1</sup> (Figure 2.7). Among the nanoparticles, mass gain showed a dose-related decrease for 25 nm CuO, with the inhibition being similar to that of CuSO<sub>4</sub> at 1 000 mg Cu L<sup>-1</sup>.

Figure 2.7 - Weight gain of *P. vulgaris* seeds as function of the concentration of nCuO and CuSO<sub>4</sub> (in mg Cu L<sup>-1</sup>). According to the Dunnett's test at  $p < 0.05$  the treatments marked with asterisk are significantly different from the negative control



Copper is a micronutrient, but as any chemical it becomes toxic at high concentrations. High Cu concentrations reduce root development, leading to deficient water and nutrient uptake and consequent growth reduction.<sup>28</sup> This was confirmed by the results shown in Figure 2.4, where seedling growth is strongly affected by an excess of Cu.

Increments in germination rate were also observed for other seed species treated with nano Zn<sup>29</sup> and Ag.<sup>30</sup> Gokak and Taranath suggested that Zn nanoparticles may photo generate radical species that can favor the germination process, Parveen and Rao argued that Ag nanoparticles might create nano holes facilitating the water transport. Although these hypotheses might sound interesting, the experimental strategies in the cited papers did not prove them. The argument of the radical formation, regardless the generation mechanism,

found some resonance in our results. As discussed below, the copper nanoparticles were reactive (in terms of  $H_2O_2$  decomposition), it is currently known that radicals may also act as singling molecule and therefore, under certain conditions, they could promote the germination.<sup>31</sup>

Contrary to our findings, low doses of  $<50$  nm CuO nanoparticles decreased the germination of rice (*Oryza sativa* L.); the concentrations used were 0.5–1.5 mM (39.8 to 119.3 mg L<sup>-1</sup>). Root mass and length were equally affected under nCuO stress. Copper stressed roots showed loss of viable cells as established by Evans blue staining.<sup>32</sup> In green peas (*Pisum sativum* L.), mass gain was also impaired at higher nCuO concentrations (from 100 to 500 mg L<sup>-1</sup>). An increase in reactive oxygen species, lipid peroxidation, and gene expression in the roots were found.<sup>22</sup> Lower concentrations (10 and 20 mg L<sup>-1</sup>) of 20–30 nm nCuO reduced the root length and mass gain of lettuce (*Lactuca sativa*), accompanied by increased catalase activity and decreased ascorbate peroxidase activity.<sup>33</sup>

Thus, in addition to our results that showed that dose and type of nanoparticles play a role in the seed germination and growth effects, the literature indicated that the effects may also vary from one plant species to another.

### 2.3.3 Determination of Cu uptake by *Phaseolus vulgaris* seeds

To determine the Cu content of seedlings exposed to nCuO, CuSO<sub>4</sub>, and water by EDXRF, the seed coat was removed to enable separate analysis of the seedling and respective seed coat (Figure 2.8).

Figure 2.8 - Seed coat and seedling of a common bean. These parts were separated to determine the Cu content shown in Figure 2.9

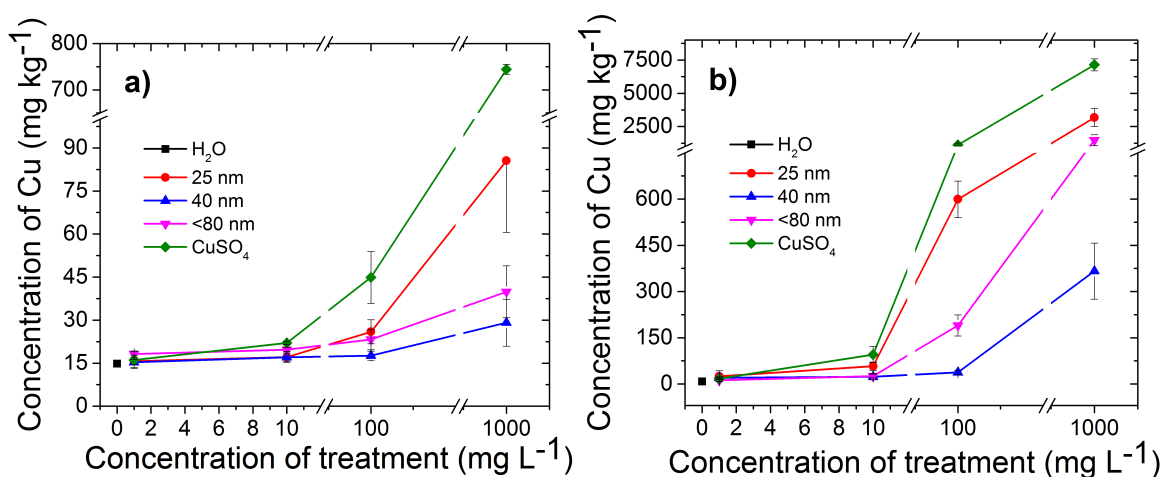


Figure 2.9 presents the concentration of Cu accumulated in the seedlings (a) and in the seed coat (b). The concentration of Cu in both the seedling and the seed coat increased as a function of the nCuO or CuSO<sub>4</sub> concentration. Copper was much more concentrated in the external than in the inner part of the seeds. It means that the seed coat was an effective barrier for nCuO absorption, but this was less evident for CuSO<sub>4</sub>. In the case of ZnO nanoparticles, Zn uptake by the endosperm of corn without seed coat during germination was about six times higher than in the whole grain.<sup>34</sup>

Deionized water treatment (negative control) gave concentrations of  $14.8 \pm 0.5$  mg Cu kg<sup>-1</sup> in the seedling and  $8.2 \pm 1.6$  mg Cu kg<sup>-1</sup> in the seed coat. Concentrations close to the negative control were observed for the seeds exposed to nCuO at 1 and 10 mg Cu L<sup>-1</sup>, suggesting that at these concentrations Cu hardly managed to enter and cross the seed coat. The concentration of Cu incorporated by the seeds sharply rose at nCuO exposure levels of 100 and 1 000 mg Cu L<sup>-1</sup>. Compared to the other two nanoparticles sizes, the 40 nm nCuO seemed to be less incorporated by the seeds.

A linear correlation was found between the content of Cu taken up by the seed coat/seedling and the concentration of CuSO<sub>4</sub> solution used for seed priming. Both adjusts (not shown here) gave Pearson's  $r > 0.98$ . The slope for the relationship between Cu concentration in the embryo and exposure concentration (Figure 2.9a) was 11.2 times lower than that found for the seed coat (Figure 2.9b).

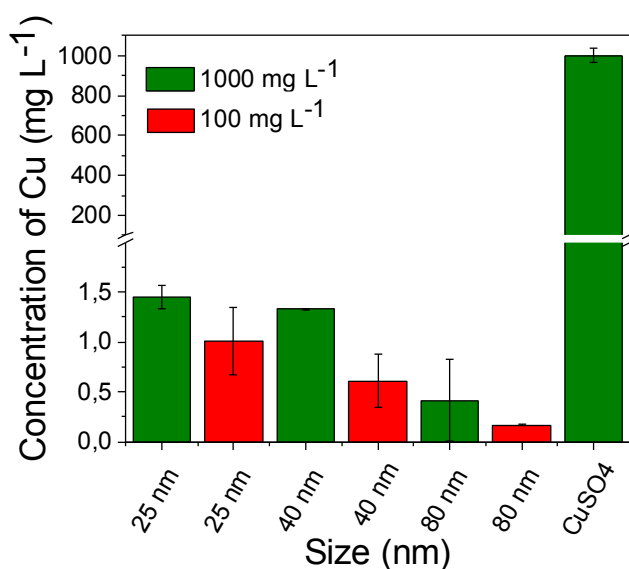
Figure 2.9 - Copper concentrations in the (a) seedling and (b) seed coat of germinated common bean seeds treated with 25, 40, <80 nm CuO nanoparticles, CuSO<sub>4</sub> (1–1 000 mg Cu L<sup>-1</sup>) and H<sub>2</sub>O (control)



Cu solubility tests were carried out to evaluate the fraction of soluble Cu ions released by the nCuO. They indicated that the smaller the nCuO size, the greater the solubility (Figure 2.10). At 100 mg Cu L<sup>-1</sup>, the supernatant fraction of the 25 nm nCuO dispersion contained 1.1 ± 0.3 mg Cu L<sup>-1</sup> compared with 0.18 ± 0.01 mg Cu L<sup>-1</sup> for the 80 nm nCuO dispersion. Such low concentrations in solution suggest that Cu incorporated by the seedling corresponded mainly to dispersed nCuO rather than only to ionic Cu in solution. For cucumber seedlings (*Cucumis sativus* L.), which seeds were exposed to ZnO nanoparticles, the Zn content was significantly correlated with the soluble Zn found in the solution, which indicates that cucumber seeds uptake Zn mainly in the soluble form.<sup>34</sup>

Exposure to the 80 nm nCuO led to concentrations of 40 ± 9 and 1 500 ± 400 mg Cu kg<sup>-1</sup> in the embryo and seed coat, respectively. Different from the 25 nm nCuO, no effect on germination or weight was found for 80 nm nCuO at 1 000 mg Cu L<sup>-1</sup>. These results suggest that these latter nanoparticles may be used in seed priming when it is aimed at overcoming Cu deficiency.

Figure 2.10 - Cu soluble fraction in the supernatant of nCuO (25, 40 and 80 nm) dispersions and CuSO<sub>4</sub> solution



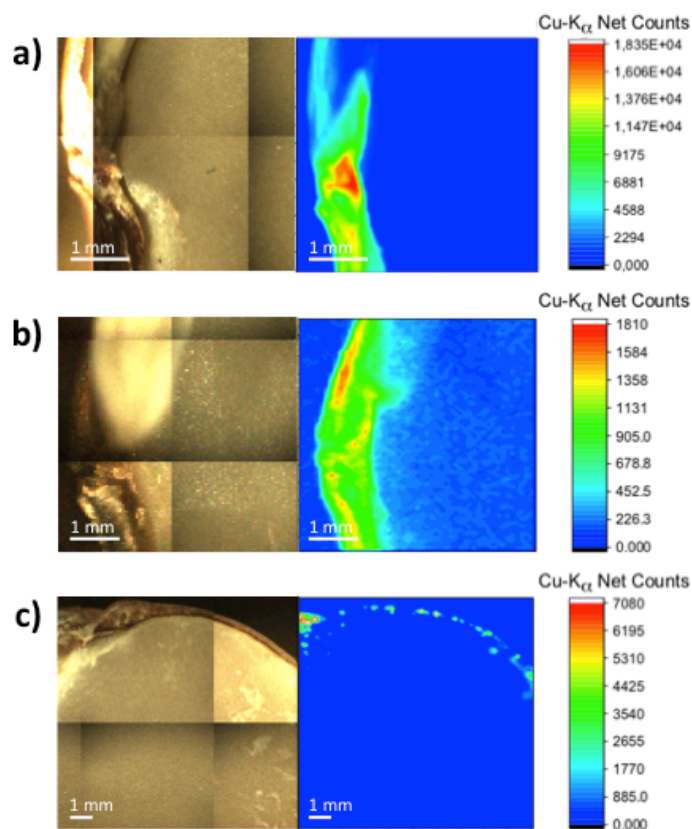
### 2.3.4 Spatial distribution of Cu in the soaked seeds

$\mu$ -XRF is a nondestructive microanalytical method that allows evaluating the spatial distribution of elements in for instance biological tissues. To the best of our knowledge, this is the first  $\mu$ -XRF mapping of treated seeds. This technique has been commonly used to investigate the allocation of elements in nontreated seeds like wheat,<sup>35</sup> rice,<sup>36</sup> soybean,<sup>37</sup> and *Arabidopsis thaliana*.<sup>38</sup> However, most of these studies employed synchrotron X-ray sources. Here we show results acquired using an X-ray tube excitation laboratory benchtop facility that uncovered the pattern of distribution of Cu in the nCuO and CuSO<sub>4</sub> exposed bean seeds.

Figure 2.11 shows the mapped area of the seed and the corresponding Cu chemical image for a seed soaked in CuSO<sub>4</sub> (a) nCuO 25 nm (b) and nCuO 40 nm (c). The images were recorded 24 h after the soaking and prior to seed germination. The  $\mu$ -XRF maps confirmed the EDXRF results (shown above) that the Cu was mostly concentrated in the seed coat but also revealed the presence of Cu hotspots in the hilum region.

To be absorbed by the seeds, the water-dispersed nanoparticle must cross the seed coat (or testa). This structure is composed by a layer of sclerenchyma cells, similar to the palisade cells, with a thick cell wall. Below this layer, there is another layer characterized by smaller cells and finally a parenchyma composed of elongated outer cells and smaller internal cells with irregular or branched shapes. Common beans have a hilum associated with the seed coat, which is a scar left by the funiculus, the structure that connects the seed to the placenta. Just below the hilum there is the micropyle, a small pore that allows water uptake into the seed.<sup>39</sup>

Figure 2.11 - Pictures and  $\mu$ -XRF chemical maps for Cu in common bean seeds exposed to (a)  $\text{CuSO}_4$  at  $1\,000\text{ mg Cu L}^{-1}$ , (b) nCuO 25 nm at  $1000\text{ mg Cu L}^{-1}$ , and (c) nCuO 40 nm at  $5\,000\text{ mg Cu L}^{-1}$



The chemical images also revealed the existence of a concentration gradient from the outer to the inner region of the seed. This indicates that movement of Cu is driven by the higher chemical potential of the nCuO dispersion or  $\text{CuSO}_4$  solution. Since the seed coat is not a homogeneous structure, the nCuO particles or Cu ions may find preferential channels, such as through the micropyle.

Differently from the EDXRF assessment, which gave the average concentrations of Cu in the seedling (comprising the storage tissue and emerging root) (Figure 2.9a), the spatial resolution provided by the  $30\ \mu\text{m}$  X-ray beam shows that Cu is concentrated in a small fraction of the embryo. Therefore, although Cu is not well distributed along the seedling tissue, its presence in very specific regions of the tissue was sufficient to affect seedling weight gain at  $1\,000\text{ mg Cu L}^{-1}$ .

Because of its high solubility, Cu from the  $\text{CuSO}_4$  treatment was more prone to be absorbed than from the nCuO treatment. This indicates that Cu transport through the seed occurs by diffusion, since the transport of Cu ions is much faster and easier than that of nanoparticles.

### 2.3.5 Chemical speciation of the incorporated Cu

Once Cu accumulation spots were located, we determined its chemical form using XAS, which is a nondestructive tool. Figure 2.12a shows the spots measured in the treated seeds. Figure 2.12b–d shows the spectra recorded in the outside, seed coat, embryo, radicle, and pristine nanoparticles used to produce the  $1\,000\text{ mg Cu L}^{-1}$  dispersions. Figure 2.12b presents data for treatments with 25 nm nCuO, Figure 2.12c for 40 nm nCuO and Figure 2.12d for 80 nm nCuO.

Figure 2.12b indicates that the chemical environment on the outside of the seed coat, in the hilum region (seed coat) and inside the seed (embryo) treated with 25 nm nCuO was the same. The spectra recorded in these regions are slightly different from the spectra obtained for the pristine 25 nm nCuO. The observed differences are the decrease of the pre-edge feature at 8 982 eV assigned to the 1s to 4p electronic transition in  $\text{Cu}^{1+}$  followed by an increase of the white line intensity. These two spectral changes are related to the oxidation of  $\text{Cu}^{1+}$  to  $\text{Cu}^{2+}$ .<sup>40</sup> The spectrum recorded in the radicle presented the features of the pristine material.

Figure 2.12c shows a pronounced shoulder feature for the Cu located in the embryo of the seed primed with nCuO. This feature is associated with  $\text{Cu}^{1+}$  and indicates that 40 nm nCuO was reduced compared to that found in the seed coat and outside of the seed. The linear combination analysis (Figure 2.13) showed that spectra recorded in the embryo could be described as a mixture of  $34 \pm 1\%$   $\text{Cu}_2\text{O}$  and  $66 \pm 1\%$   $\text{CuO}$ . Figure 2.12d shows that the chemical neighborhood of Cu incorporated by the seed tissues and radical in the samples treated with 80 nm nCuO did not change and remained as  $\text{CuO}$ . The spectra recorded in the samples perfectly overlapped that recorded for the pristine 80 nm nCuO powder.

Figure 2.12 - Cu-K edge XAS spectra recorded in different regions of *P. vulgaris* seeds treated with 1 000 mg Cu L<sup>-1</sup> dispersions of CuO nanoparticles. (a) Picture of a bean seed pointing out the three regions measured, (b) spectra recorded of the 25 nm nCuO treatment, (c) spectra recorded of the 40 nm nCuO treatment, and (d) spectra recorded of the 80 nm nCuO treatment

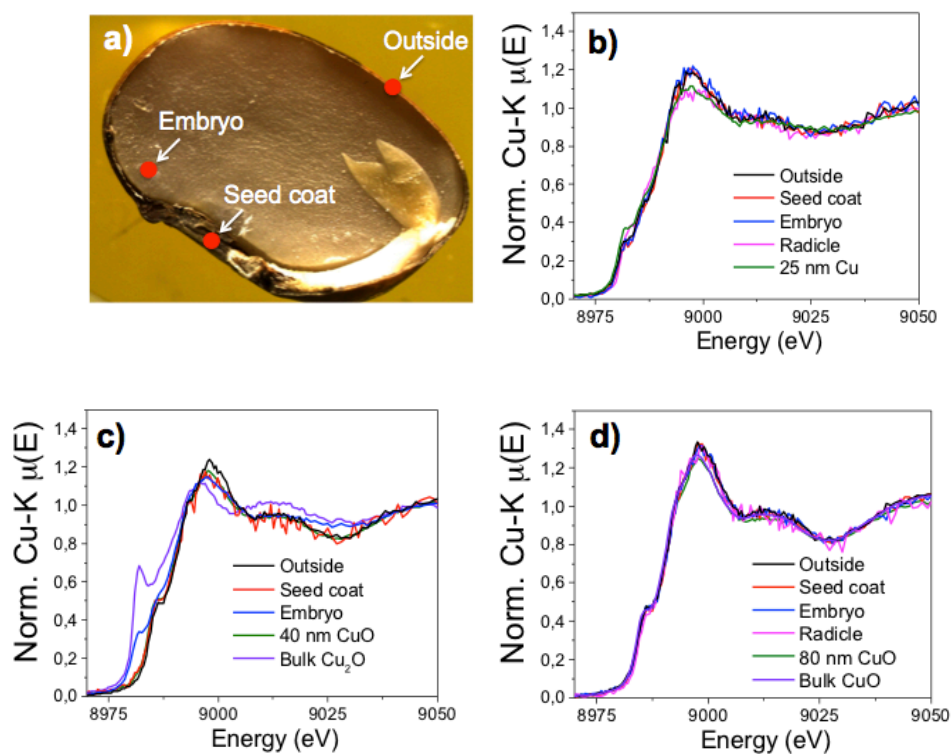
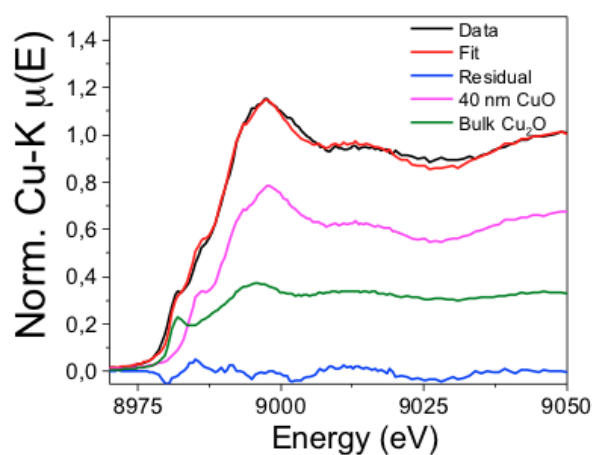


Figure 2.13 - Linear combination fit for Cu-K edge XAS spectra recorded in the embryo of a *P. vulgaris* seed treated with 40 nm nCuO at 1 000 mg Cu L<sup>-1</sup>



The copper chemical environment in harvested *Arabidopsis thaliana* seeds treated with 20 and 50 mg L<sup>-1</sup> nCuO was also mostly in the form of CuO (88.8%), with some Cu<sub>2</sub>(OH)PO<sub>4</sub> (2.0%), Cu-acetate (3.2%), and Cu<sub>2</sub>O (6.0%).<sup>41</sup> This suggests that nCuO can be also accumulated in plant progeny.

Although our results showed a slight redox behavior for 40 and 25 nm nCuO in a physiological environment, the Cu-based nanoparticles used in this study were not as reactive as ZnO.<sup>37</sup> This can be partially explained by the low solubility of the CuO based nanoparticles. However, one has to keep in mind that the sensitivity of XAS would hardly be able to identify the presence of Cu fractions below 5 wt %.

The combined data supplied by EDXRF,  $\mu$ -XRF maps,  $\mu$ -XANES, and literature background on seed morphology<sup>39</sup> suggested that the main Cu uptake mechanism takes place through diffusion driven by the concentration gradient. The main entrance region was the hilum spongy tissue. The presence of CuO and Cu<sub>2</sub>O most likely indicated that the CuO nanoparticles were incorporated as entire particles instead of anions. In addition to the spectroscopic speciation, this hypothesis was supported by the hilum pore size, which reaches tens of micrometers (see the electronic Supporting Information of Duran et al.<sup>42</sup>). The presence of Cu in the endosperm region away from the hilum (Figure 2.11c) also implied that possibility of Cu to cross the seed coat structure. Nevertheless, the extent of the penetration into the endosperm was smaller. In this context, it is worth mentioning that there are many pathways of Cu transportation in plants. In cell-to-cell migration, Cu can be coordinated by proteins like Cu chaperones and Cu carriers, which transport Cu to the organelles.<sup>43</sup>

### 2.3.6 *In vivo* spatial distribution of Cu in the seedlings

In addition to the chemical maps that uncovered the spatial distribution of Cu in the seeds after the priming, we mapped the *in vivo* chemical distribution of Cu in the primary root of the seedling under development. We monitored seedlings primed in CuSO<sub>4</sub> at 1 000 mg Cu L<sup>-1</sup> and 40 nm nCuO at 100 mg Cu L<sup>-1</sup> since these treatments showed significant effects compared to the control according to the Dunnett's test.

Figure 2.14a-c shows the pictures and corresponding Cu-K $\alpha$  chemical images for the emerging primary root of the seedling primed in CuSO<sub>4</sub> at 1 000 mg Cu L<sup>-1</sup> on the third, fourth, and fifth day of germination, respectively. The chemical images revealed a hotspot of Cu on the tip of the primary root, which remained on the same location along the monitored period and was not diluted during the growing process.

Figure 2.14 - Pictures and  $\mu$ -XRF chemical maps for Cu in the primary root of a *P. vulgaris* seed exposed to CuSO<sub>4</sub> at 1 000 mg Cu L<sup>-1</sup> on the (a) third, (b) fourth, and (c) fifth day of germination

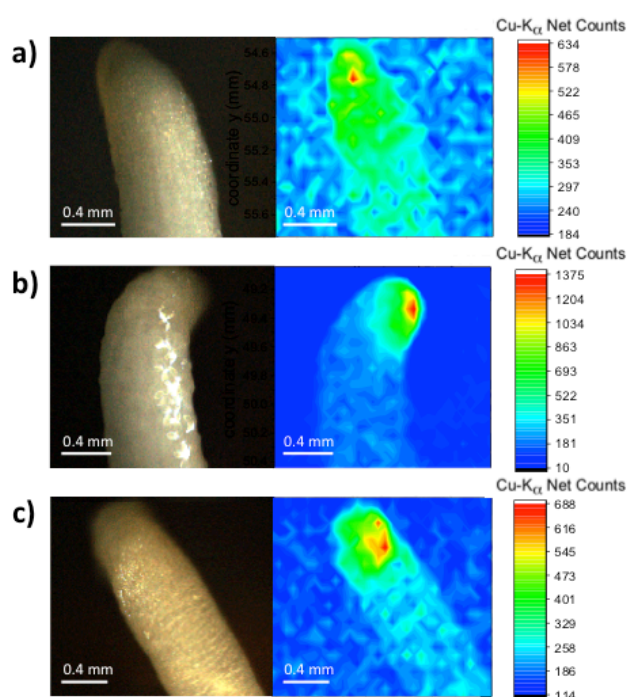


Figure 2.15 presents the pictures and chemical maps for the tip of the primary root of the seedling treated with 40 nm nCuO at 100 mg Cu L<sup>-1</sup> on the third (a), fourth (b), and fifth (c) day of the seedling growth. The results were similar to those found for CuSO<sub>4</sub>.

Figure 2.15 - Pictures and  $\mu$ -XRF chemical maps for Cu in the primary root of a *P. vulgaris* seed exposed to nano CuO 40 nm at 100 mg Cu L<sup>-1</sup> on the (a) third, (b) fourth, and (c) fifth day of germination

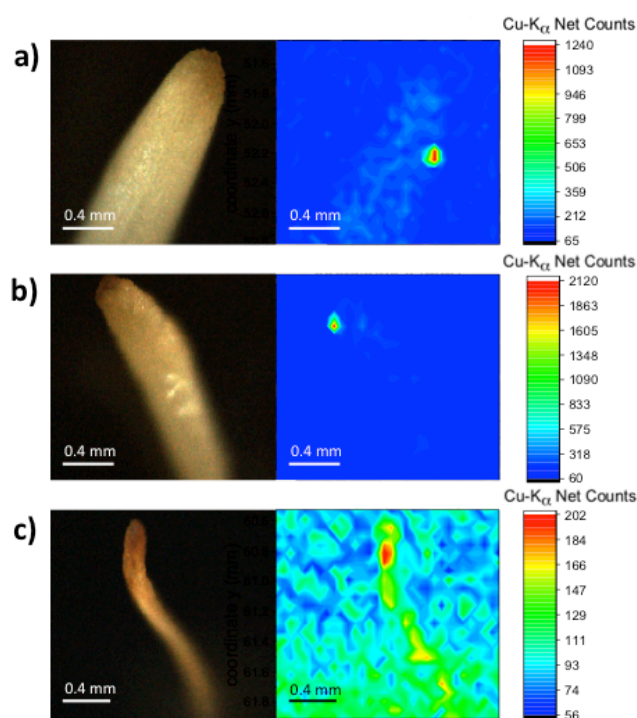
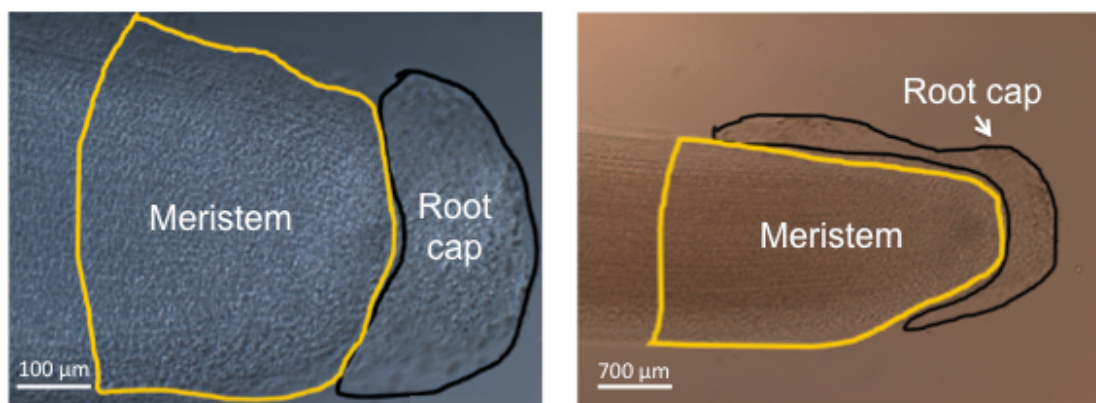


Figure 2.16 presents an optical microscope image that was allowed to precisely identify the tissue in which the Cu spots were found. It corresponded to the root cap. We believe that the root cap incorporated Cu from the seed coat during the radical emergence. It is also noteworthy mentioning that the incorporation and diffusion of Cu could be favored by the chemical properties of mucilage, especially in the soluble form. The chemical images also showed that the Cu transferred to the root cap had low mobility. Part of the Cu could have been transferred to the meristem, site of intense cell division activity, which at low concentrations may have favored root growth while at high concentration it might have prevented it. Previous experiments carried out by Wang and colleagues, in the model species *Arabidopsis thaliana*, showed that nCuO treatments induce modulation of auxin related genes, supporting the idea that changes in root growth rates are related to the modulation of auxin sensing and root size control.

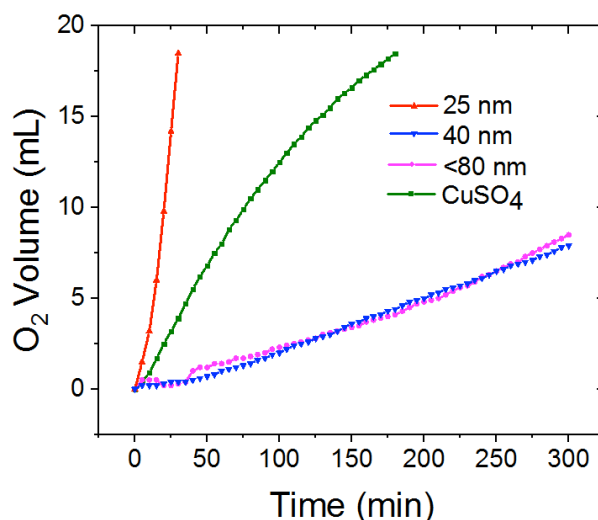
Figure 2.16 - Optical microscopy of primary roots of the common bean. The root cap is the site that contained the highest Cu concentrations after exposure of the beans to CuO nanoparticles or CuSO<sub>4</sub>



### 2.3.7 Chemical reactivity of Cu based nanoparticles and physiological effects

The deleterious effects of the 25 nm CuO nanoparticles at 100 and 1 000 mg Cu L<sup>-1</sup> could not be explained by the treatment concentration, since a different behavior was found for 40 and 80 nm nCuO. The crystal phase effects could not be accessed in the present study since for all particles the CuO were monoclinic. However, the literature indicated that for rutile and anatase TiO<sub>2</sub> the crystal phase did not influence the uptake and translocation of TiO<sub>2</sub> in wheat.<sup>44</sup>

Figure 2.17 shows the degradation of H<sub>2</sub>O<sub>2</sub> by the CuO nanoparticle dispersions used to prime the seeds. The 40 and 80 nm nCuO presented similar behavior, taking nearly 300 min to produce 7.9 and 8.5 mL of O<sub>2</sub>, respectively. CuSO<sub>4</sub> produced 18.5 mL of O<sub>2</sub> in 180 min. The most reactive nanoparticle was the 25 nm CuO that readily produced 18.5 mL of O<sub>2</sub> in 30 min. The surface properties of core-shell structures can greatly differ from those exhibited by single phase materials. For example, the catalytic activity of Ru-Cu nanoparticles in converting NH<sub>3</sub> into N<sub>2</sub> and H<sub>2</sub> depends on the number of Cu layers on top of Ru.<sup>45</sup> Facing the low solubility shown by all Cu-based nanoparticles used in the present study and the similar results obtained for the 40 and 80 nm CuO particles, we hypothesize that the deleterious effects of the 25 nm particles may be caused by their modified surface properties.

Figure 2.17 - H<sub>2</sub>O<sub>2</sub> degradation rate in the presence of CuSO<sub>4</sub> and 25, 40 and 80 nm nCuO

Considering the excess of Cu ions, the deleterious effects can be explained in the light of previous studies. The literature reports after 5 days of germination under normal conditions, an increase in protein and amino acid content in *Phaseolus* beans.<sup>46</sup> On the other hand, cotyledons of germinating bean seeds (*Phaseolus vulgaris*) exposed to 200  $\mu\text{M}$  CuCl<sub>2</sub> (26.9 mg L<sup>-1</sup>) showed protein damage and oxidative stress. In common beans, Cu toxicity caused inactivation of the ubiquitin-proteasome pathway, an important nonlysosomal proteolytic system, and inhibition of leucine and proline aminopeptidase activities. These injuries led to a deficiency in the cell's capability to remove oxidatively damaged proteins.<sup>47</sup> Oxidative stress was also found in lettuce treated with nCuO at 20 mg L<sup>-1</sup>. Cu reduced catalase and ascorbate peroxidase activities, two important antioxidant enzymes.<sup>33</sup> Nevertheless, our chemical speciation did not detect Cu binding to proteins. The chemical environments were mostly similar to those of pristine materials. It means that in the case Cu-protein interaction actually happened, the fraction of Cu playing this role was below the XAS detection limit. In linear combination analysis of XAS, a component weighting less than 5% would be hardly detectable, since normalization can introduce errors on the order of 10%.

Besides preventing the development of *P. vulgaris*, Cu based treatments led to reduction of the content of Ca, Fe, K, Mn, Zn, carbohydrates, and amino acids as was also observed in the embryonic axis of seeds exposed to excess Cu (5 mmol L<sup>-1</sup> or 672.2 mg L<sup>-1</sup> of CuCl<sub>2</sub>). Oxidative damage may be enhanced in Cu-intoxicated tissues and affect membrane integrity due to the lipid peroxidation process, which induces solute leakage from germinating seeds.<sup>48</sup>

Chemical imaging combined with spectroscopic speciation showed that although Cu was located in small hotspots instead of being spread homogeneously throughout the tissues, and most of the incorporated Cu remained in its pristine form, it strongly affected the germination of the seeds and the growth of the seedlings. As discussed above, it is likely that low concentrations of promptly available Cu ions may have impaired the proper functioning of proteins.

## 2.4 Conclusions

In agreement to the published literature, the present study shows that much attention has to be paid to the concentration of the nanoparticles used in seed priming. At concentrations from 1 to 100 mg Cu L<sup>-1</sup>, 40 and 80 nm nCuO did not harm the seed germination and seedling development, while 40 nm nCuO at 100 mg Cu L<sup>-1</sup> favored weight gain. The 80 nm nCuO did not affect weight gain, although it was able to increase concentrations in the embryo to 40 ± 9 mg Cu kg<sup>-1</sup>. This might be a consequence of the slow release of Cu ions from the oxide structure to the physiological solution. Therefore, Cu in these oxide forms can be used by the developing seedling instead of intoxicating it, different from what happened for CuSO<sub>4</sub> at 1 000 mg Cu L<sup>-1</sup> which prevented seedling growth. Hence, depending on its physical-chemical properties, CuO based nanoparticles might be considered for seed priming rather than soluble Cu sources, since the possibility of phytotoxicity by the latter is higher.

The current study also highlighted the importance of the structure and chemical nature of the nanoparticle. The effects of 25 nm nCuO, which presented a metallic core covered by an oxide shell structure, deserve further investigation. This nanoparticle, probably due to its higher surface reactivity, had deleterious effects on bean seedling development. These results reinforce the necessity of care regarding the disposal of nanoparticles in the environment and their usage as fertilizers.

## References

- 1 BORM, P. J. et al. The potential risks of nanomaterials: a review carried out for ECETOC. **Particle and Fibre Toxicology**, London, v. 3, n. 11, p. 1-35, 2006.
- 2 EUROPEAN FOOD SAFETY AUTHORITY - EFSA. Scientific Committee. Guidance on the risk assessment of the application of nanoscience and nanotechnologies in the food and feed chain. **EFSA Journal**, Parma, v. 9, n. 5, p. 1-36, 2011.

3 RIKILT; JCR. **Inventory of nanotechnology applications in the agricultural, feed and food sector.**, Parma: EFSA, 2014. 125 p. (Supporting Publication EN-621).

4 DASGUPTA, N.; RANJAN, S.; RAMALINGAM, C. Applications of nanotechnology in agriculture and water quality management. **Environmental Chemistry Letters**, Heidelberg, v. 15, n. 4, p. 591-605, 2017.

5 PEDRINI, S. et al. Seed coating: science or marketing spin? **Trends in Plant Science**, Kidlington, v. 22, n. 2, p. 106-116, 2017.

6 FAROOQ, M.; WAHID, A.; SIDDIQUE, K. H. M. Micronutrient application through seed treatments - a review. **Journal of Soil Science and Plant Nutrition**, Tokyo, v. 12, n. 1, p. 125-142, 2012.

7 FAROOQ, M. et al. Rice seed invigoration. In LICHTFOUSE, E. (Ed.). **Sustainable Agriculture Reviews**. Heidelberg: Springer, 2009. v. 1, p. 137-175.

8 MALHI, S. S. Effectiveness of seed-soaked Cu, autumn- versus spring-applied Cu, and Cu-treated P fertilizer on seed yield of wheat and residual nitrate-N for a Cu-deficient soil. **Canadian Journal of Plant Science**, Ottawa, v. 89, n. 6, p. 1017-1030, 2009.

9 CIFUENTES, Z. et al. Absorption and translocation to the aerial part of magnetic carbon-coated nanoparticles through the root of different crop plants. **Journal of Nanobiotechnology**, London, v. 8, p. 1-8, 2010.

10 LARUE, C. et al. Foliar exposure of the crop *Lactuca sativa* to silver nanoparticles: Evidence for internalization and changes in Ag speciation. **Journal of Hazardous Materials**, Amsterdam, v. 264, p. 98-106, 2014.

11 LEE, W. M. et al. Toxicity and bioavailability of copper nanoparticles to the terrestrial plants mung bean (*Phaseolus radiatus*) and wheat (*Triticum aestivum*): Plant agar test for water-insoluble nanoparticles. **Environmental Toxicology and Chemistry**, New York, v. 27, n. 9, p. 1915-1921, 2008.

12 PRASAD, T. et al. Effect of nanoscale zinc oxide particles on the germination, growth and yield of peanut. **Journal of Plant Nutrition**, New York, v. 35, n. 6, p. 905-927, 2012.

13 LOPEZ-MORENO, M. L. et al. Evidence of the differential biotransformation and genotoxicity of ZnO and CeO<sub>2</sub> nanoparticles on soybean (*Glycine max*) plants. **Environmental Science & Technology**, Washington, DC, v. 44, n. 19, p. 7315-7320, 2010.

14 MORALES, M. I. et al. Toxicity assessment of cerium oxide nanoparticles in cilantro (*Coriandrum sativum* L.) plants grown in organic soil. **Journal of Agricultural and Food Chemistry**, Washington, DC, v. 61, n. 26, p. 6224-6230, 2013.

15 LOPEZ-MORENO, M. L. et al. X-ray absorption spectroscopy (XAS) corroboration of the uptake and storage of CeO<sub>2</sub> nanoparticles and assessment of their differential toxicity in four edible plant species. **Journal of Agricultural and Food Chemistry**, Washington, DC, v. 58, n. 6, p. 3689-3693, 2010.

- 16 FRAZIER, T. P.; BURKLEW, C. E.; ZHANG, B. H. Titanium dioxide nanoparticles affect the growth and microRNA expression of tobacco (*Nicotiana tabacum*). **Functional & Integrative Genomics**, Berlin, v. 14, n. 1, p. 75-83, 2014.
- 17 TAN, W. J. et al. Surface coating changes the physiological and biochemical impacts of nano-TiO<sub>2</sub> in basil (*Ocimum basilicum*) plants. **Environmental Pollution**, Oxford, v. 222, p. 64-72, 2017.
- 18 MU, Q. X. et al. Chemical basis of interactions between engineered nanoparticles and biological systems. **Chemical Reviews**, Washington, DC, v. 114, n. 15, p. 7740-7781, 2014.
- 19 US RESEARCH NANOMATERIALS INC. **Copper Cu Nanopowder / Nanoparticles** (Cu, 99.9%, 40 nm, metal basis). Houston, s.d. Available in: <<http://www.us-nano.com/inc/sdetail/162>>. Accessed on: March 28, 2017.
- 20 HANSCH, R.; MENDEL, R. R. Physiological functions of mineral micronutrients (Cu, Zn, Mn, Fe, Ni, Mo, B, Cl). **Current Opinion in Plant Biology**, London, v. 12, n. 3, p. 259-266, 2009.
- 21 ZAFAR, H.; ALI, A.; ZIA, M. CuO nanoparticles inhibited root growth from *Brassica nigra* seedlings but induced root from stem and leaf explants. **Applied Biochemistry and Biotechnology**, Clifton, v. 181, n. 1, p. 365-378, 2017.
- 22 NAIR, P. M. G.; CHUNG, I. M. The responses of germinating seedlings of green peas to copper oxide nanoparticles. **Biologia Plantarum**, Praha, v. 59, n. 3, p. 591-595, 2015.
- 23 SARRET, G. et al. Zinc distribution and speciation in *Arabidopsis halleri* x *Arabidopsis lyrata* progenies presenting various zinc accumulation capacities. **New Phytologist**, Malden, v. 184, n. 3, p. 581-595, 2009.
- 24 RAVEL, B.; NEWVILLE, M. ATHENA, ARTEMIS, HEPHAESTUS: data analysis for X-ray absorption spectroscopy using IFEFFIT. **Journal of Synchrotron Radiation**, Copenhagen, v. 12, p. 537-541, 2005.
- 25 CARVALHO, H. W. P. et al. Improvement of the photocatalytic activity of magnetite by Mn-incorporation. **Materials Science and Engineering: B - Advanced Functional Solid-State Materials**, Amsterdam, v. 181, p. 64-69, 2014.
- 26 ISANI, G. et al. Comparative toxicity of CuO nanoparticles and CuSO<sub>4</sub> in rainbow trout. **Ecotoxicology and Environmental Safety**, Amsterdam, v. 97, p. 40-46, 2013.
- 27 CARVALHO, H. W. P. et al. TiO<sub>2</sub>-Cu photocatalysts: a study on the long- and short-range chemical environment of the dopant. **Journal of Materials Science**, Norwell, v. 48, n. 11, p. 3904-3912, 2013.
- 28 PAHLSSON, A. M. B. Toxicity of heavy-metals (Zn, Cu, Cd, Pb) to vascular plants - a literature-review. **Water Air and Soil Pollution**, Dordrecht, v. 47, n. 3-4, p. 287-319, 1989.

- 29 GOKAK, I. B.; TARANATH, T. C. Morphological and biochemical responses of *Abelmoschus esculantus* (L.) Moench to zinc nanoparticles. **Advances in Natural Sciences-Nanoscience and Nanotechnology**, Bristol, v. 6, n. 025017, p. 1-5, 2015.
- 30 PARVEEN, A.; RAO, S. Effect of Nanosilver on Seed Germination and Seedling Growth in *Pennisetum glaucum*. **Journal of Cluster Science**, New York, v. 26, n. 3, p. 693-701, 2015.
- 31 WOJTYLA, L. et al. Different modes of hydrogen peroxide action during seed germination. **Frontiers in Plant Science**, Lausanne, v. 7, p. 16, 2016. DOI: 10.3389/fpls.2016.00066.
- 32 SHAW, A. K.; HOSSAIN, Z. Impact of nano-CuO stress on rice (*Oryza sativa* L.) seedlings. **Chemosphere**, Oxford, v. 93, n. 6, p. 906-915, 2013.
- 33 TRUJILLO-REYES, J. et al. Exposure studies of core-shell Fe/Fe<sub>3</sub>O<sub>4</sub> and Cu/CuO NPs to lettuce (*Lactuca sativa*) plants: Are they a potential physiological and nutritional hazard? **Journal of Hazardous Materials**, Amsterdam, v. 267, p. 255-263, 2014.
- 34 ZHANG, R. C. et al. Phytotoxicity of ZnO nanoparticles and the released Zn(II) ion to corn (*Zea mays* L.) and cucumber (*Cucumis sativus* L.) during germination. **Environmental Science and Pollution Research**, Landsberg, v. 22, n. 14, p. 11109-11117, 2015.
- 35 AJIBOYE, B. et al. X-ray fluorescence microscopy of zinc localization in wheat grains biofortified through foliar zinc applications at different growth stages under field conditions. **Plant and Soil**, The Hague, v. 392, n. 1-2, p. 357-370, 2015.
- 36 KYRIACOU, B. et al. Localization of iron in rice grain using synchrotron X-ray fluorescence microscopy and high resolution secondary ion mass spectrometry. **Journal of Cereal Science**, London, v. 59, n. 2, p. 173-180, 2014.
- 37 HERNANDEZ-VIEZCAS, J. A. et al. In situ synchrotron x-ray fluorescence mapping and speciation of CeO<sub>2</sub> and ZnO nanoparticles in soil cultivated soybean (*Glycine max*). **ACS Nano**, Washington, DC, v. 7, n. 2, p. 1415-1423, 2013.
- 38 YOUNG, L. et al. Inferring the geometry of fourth-period metallic elements in *Arabidopsis thaliana* seeds using synchrotron-based multi-angle X-ray fluorescence mapping. **Annals of Botany**, Oxford, v. 100, n. 6, p. 1357-1365, 2007.
- 39 VIEIRA, C.; PAULA JÚNIOR, T. J.; BORÉM, A. **Feijão**. 2. ed. Viçosa: Universidade Federal de Viçosa, 2006. 600 p.
- 40 GUNTER, T. et al. Structural snapshots of the SCR reaction mechanism on Cu-SSZ-13. **Chemical Communications**, London, v. 51, n. 44, p. 9227-9230, 2015.
- 41 WANG, Z. Y. et al. CuO nanoparticle interaction with *Arabidopsis thaliana*: Toxicity, parent-progeny transfer, and gene expression. **Environmental Science & Technology**, Washington, DC, v. 50, n. 11, p. 6008-6016, 2016.

- 42 DURAN, N. M. et al. X-ray spectroscopy uncovering the effects of cu based nanoparticle concentration and structure on *Phaseolus vulgaris* germination and seedling development. **Journal of Agricultural and Food Chemistry**, Washington, DC, v. 65, n. 36, p. 7874-7884, 2017.
- 43 YRUELA, I. Copper in plants: acquisition, transport and interactions. **Functional Plant Biology**, Collingwood, v. 36, n. 5, p. 409-430, 2009.
- 44 LARUE, C. et al. Accumulation, translocation and impact of TiO<sub>2</sub> nanoparticles in wheat (*Triticum aestivum* spp.): Influence of diameter and crystal phase. **Science of the Total Environment**, Amsterdam, v. 431, p. 197-208, 2012.
- 45 CHAKRABORTY, D. et al. Bottom up design of a novel CuRu nanoparticulate catalyst for low temperature ammonia oxidation. **Angewandte Chemie International Edition**, Weinheim, v. 56, n. 30, p. 8711-8715, 2017.
- 46 LEE, C. K.; KARUNANITHY, R. Effects of germination on the chemical-composition of *Glycine* and *Phaseolus* beans. **Journal of the Science of Food and Agriculture**, London, v. 51, n. 4, p. 437-445, 1990.
- 47 KARMOUS, I. et al. Role of the ubiquitin-proteasome pathway and some peptidases during seed germination and copper stress in bean cotyledons. **Plant Physiology and Biochemistry**, Paris, v. 76, p. 77-85, 2014.
- 48 SFAXI-BOUSBIH, A.; CHAOUI, A.; EL FERJANI, E. Unsuitable availability of nutrients in germinating bean embryos exposed to copper excess. **Biological Trace Element Research**, Totowa, v. 135, n. 1-3, p. 295-303, 2010.



### 3 BEAN SEEDLING GROWTH ENHANCEMENT USING MAGNETITE NANOPARTICLES

#### Abstract

Advanced fertilizers are one of the top requirements to address rising global food demand. This study investigates the effect of bare and polyethylene glycol-coated Fe<sub>3</sub>O<sub>4</sub> nanoparticles on the germination and seedling development of *Phaseolus vulgaris* L. Although the germination rate was not affected by the treatments (1 to 1 000 mg Fe L<sup>-1</sup>), seed soaking in Fe<sub>3</sub>O<sub>4</sub>-PEG at 1 000 mg Fe L<sup>-1</sup> increased radicle elongation (8.1 ± 1.1 cm vs. 5.9 ± 1.0 cm for the control). Conversely, Fe<sup>2+</sup>/Fe<sup>3+</sup><sub>(aq)</sub> and bare Fe<sub>3</sub>O<sub>4</sub> at 1 000 mg Fe L<sup>-1</sup> prevented the growth. X-ray spectroscopy and tomography showed that Fe penetrated in the seed. Enzymatic assays showed that Fe<sub>3</sub>O<sub>4</sub>-PEG was least harmful treatment to α-amylase. The growth promoted by the Fe<sub>3</sub>O<sub>4</sub>-PEG might be related to water uptake enhancement induced by the PEG coating. These results show the potential of using coated iron nanoparticles to enhance the growth of common food crops.

**Keywords:** *Phaseolus vulgaris* L. Fe<sub>3</sub>O<sub>4</sub> nanoparticle. Polyethylene glycol. Germination. X-ray spectroscopy.

### 3.1 Introduction

The population growth is pushing agriculture worldwide to intensify the use of chemical fertilizers in order to meet the increasing food demand. A large portion of fertilizers applied into the soil is lost by water leaching, strong adsorption, or in case of nitrogen sources, by evaporation. This loss affects negatively the environment, the sustainability of mineral inputs and the economic performance of agricultural activity. In this context, nano-sized fertilizers can become an alternative to increase plant uptake ratio. Thus, paving the way to a more sustainable strategy to improve nutrient delivery.<sup>1</sup>

Nutrient seed priming is an option to deliver micronutrients to plants. A proper supply of micronutrients during the earlier growth stages may improve seedling emergence, grain yield and nutritional content.<sup>2</sup> Nutrient primed seeds have been shown to increase yield of maize,<sup>3</sup> oat,<sup>4</sup> wheat<sup>5; 6</sup> and rice.<sup>7</sup> Seedlings obtain nutrients partly from seed reserves and partly from soil. An adequate nutrient reserve in the seed is necessary to sustain seedling growth until roots starts the nutrient supply function.<sup>8</sup> Although seed priming is commonly practiced by farmers, and a fairly investigated topic, we did not find any model explaining how the nutrients applied to seeds migrate to the plant.

Fe is mostly found as  $\text{Fe}^{3+}$  oxides and oxyhydroxides in cultivated (aerated) soils.<sup>9</sup> Despite of their abundancy, compounds such as goethite, ferrihydrite and hematite presents  $K_{sp}$  values ranging from  $10^{-37}$  to  $10^{-44}$ , which make them virtually insoluble. Even though the total Fe content is high, its availability to plants is still low. The availability of Fe is also influenced by the crystallite size and degree of isomorphic substitution.<sup>10</sup> It has been reported that rates of dissolution decrease with the following order: ferrihydrite > lepidocrocite > magnetite > hematite > goethite.<sup>11</sup>

Even though  $\text{Fe}^{3+}$  is more available than  $\text{Fe}^{2+}$ , for most plants the preferred absorption form is  $\text{Fe}^{2+}$ .<sup>9</sup> Iron uptake differs for nongraminaceous and graminaceous plants. For the former, plant species take up Fe via three mechanisms: (i) excreting protons from the roots to the rhizosphere, reducing the soil solution pH and thus increasing  $\text{Fe}^{3+}$  solubility; (ii) reducing  $\text{Fe}^{3+}$  to  $\text{Fe}^{2+}$  by  $\text{Fe}^{3+}$ -chelate reductase; and (iii) plasmalemma transport of  $\text{Fe}^{2+}$  by iron transporters. On the other hand, roots of graminaceous species release phytosiderophores that chelate  $\text{Fe}^{3+}$  in the rhizosphere, and then specific plasmalemma transporters take the  $\text{Fe}^{3+}$ -phytosiderophores complexes.<sup>1; 12</sup>

Iron is an essential element for plants. Its deficiency can limit plant development and reduce grain yield.<sup>13</sup> It plays an important role in the photosynthetic activity, biosynthesis of many enzymes, Fe-S protein clusters and heme proteins like cytochromes. It is required in chloroplast thylakoids structure and chlorophyll synthesis.<sup>9</sup> The legume–rhizobium symbiosis is sensitive to Fe deficiency,<sup>14</sup> Fe seems to be involved in nitrogen fixation through enzymes such as nitrogenase, nitrogen reductase and leghemoglobin.<sup>15</sup>

In common bean (*Phaseolus vulgaris*) Fe concentration in grains and shoot tissue is around 76 mg kg<sup>-1</sup> and 154 mg kg<sup>-1</sup>,<sup>16</sup> respectively. It means that at least ca. 653 g Fe ha<sup>-1</sup> are necessary for the proper culture development (the consulted data did not include Fe concentration in roots, thus this is a lower boundary estimation). Since this nutrient is required in large quantities, seed priming can only supply part of plants requirements, especially for the early phenological states. High loads of nutrients via seed treatment can induce phytotoxic effects.<sup>17; 18; 19</sup>

Magnetic iron oxide nanoparticles are currently used in drug delivery systems, contrast agents in magnetic resonance imaging, hyperthermia treatments, the production of magnetic inks and magnetic seals in motors, to name a few applications.<sup>20</sup> In all instances, iron nanoparticle effects vary according to their chemical composition, size, morphology, aggregation state, applied concentration as well as experimental conditions like temperature and time of exposure. Nano magnetite was chosen for this study because of it is a well-characterized nanomaterial. It is easy to synthesize, relatively cheap and used in several types of applications, especially biotechnological ones.<sup>21; 22; 23; 24; 25</sup>

In the agricultural scenario, the effects of iron nanoparticles have been observed in the uptake, transport, accumulation and development of plant species. It has been previously demonstrated that iron oxide nanoparticles accumulated in pumpkin plants tissues,<sup>26</sup> stimulated the development of peanut<sup>27</sup> and watermelon<sup>28</sup> seedlings, but did not affect growth and chlorophyll content of lettuce.<sup>22</sup>

Magnetite nanoparticles are prone to aggregation due to a combined effect of their high surface area to volume ratio and their strong magnetization, which however limits their use for bio-applications.<sup>29</sup> To address the former problem, magnetite nanoparticles are usually synthesized in the presence of surfactants, forming a coating layer preventing aggregation. Common surfactants are polyethylene glycol (PEG), polyvinyl alcohol (PVA), Polyvinylpyrrolidone (PVP), poly lactic-co-glycolic acid (PLGA), chitosan and dextran.<sup>21</sup>

Among them, PEG is a hydrophilic polymer widely used for biomedical applications, being biocompatible, non-immunogenic, and non-antigenic.<sup>30</sup>

In this work, we report the effect of Fe<sub>3</sub>O<sub>4</sub>-PEG and bare Fe<sub>3</sub>O<sub>4</sub> nanoparticles on the germination and seedling development of *Phaseolus vulgaris* L. seeds. The effects of 1, 10, 100 and 1 000 mg Fe L<sup>-1</sup> seed soaking treatments were observed on the germination rate, radicle elongation and  $\alpha$ -amylase activity of 5-days old seedlings. X-ray fluorescence (XRF) and absorption (XANES) spectroscopy, X-ray tomography and scanning electron microscopy (SEM-EDX) uncovered the Fe uptake and spatial distribution.

## 3.2 Materials and Methods

### 3.2.1 Synthesis of iron oxide nanoparticles

Bare magnetite nanoparticles (nFe<sub>3</sub>O<sub>4</sub>) were synthesized by a co-precipitation method using a mixture of iron (III) chloride tetrahydrate (FeCl<sub>2</sub>·4H<sub>2</sub>O) and iron (II) chloride hexahydrate (FeCl<sub>3</sub>·6H<sub>2</sub>O), both purchased from Sigma-Aldrich at a 2:1 molar ratio of Fe<sup>3+</sup>:Fe<sup>2+</sup>,  $m_{FeCl_3} = 7.00$  g,  $m_{FeCl_2} = 2.58$  g in 300 ml DI water. The solution was poured in a three-neck round bottom flask provided with a condenser, nitrogen and liquid inlets. Then 0.5 ml of a 37 % wt. HCl were added under gentle agitation. Oxygen was purged using nitrogen for 20 minutes prior the addition of 100 ml 1.5 M NH<sub>4</sub>OH. The solution quickly turned black, indicating the beginning of the production of the nanoparticles. The reaction lasted 1 hour at 20 °C and nitrogen was supplied during the whole reaction. After the synthesis, the nanoparticles were washed using cycles of deoxygenated DI water and magnetic decantation. Then, the nanoparticles were dried at room temperature under vacuum for 24 h and immediately characterized.

A slightly modified procedure was used to produce Fe<sub>3</sub>O<sub>4</sub>-PEG nanoparticles (nFe<sub>3</sub>O<sub>4</sub>-PEG), which consisted in dissolving the iron salts in 300 ml of a 10 % wt PEG ( $M_w$  10 000) in DI water solution prior the addition of NH<sub>4</sub>OH. Reaction and washing conditions were the same as described above.

### 3.2.2 Characterization of pristine Fe<sub>3</sub>O<sub>4</sub> nanoparticles and dispersions

The composition of each set of nanoparticles was determined by energy dispersive X-ray fluorescence spectroscopy (EDXRF; EDX-720 Shimadzu, Japan). Two hundred milligrams of pristine powders were weighted in a 6.3 mm aperture X-ray fluorescence

spectroscopy (XRF) sample cup (no. 3577 - Spex Ind. Inc., USA) sealed with a 5  $\mu\text{m}$  thick polypropylene film (no. 3520 - Spex Ind. Inc., USA). The samples were analyzed using a rhodium (Rh) X-ray tube at 50 kV and auto-tunable current adjusted for a detector deadtime below 30% and a 3-mm collimator. The X-ray spectrum of the sample was acquired utilizing a Si (Li) detector for 200 s. The analyses were carried out in triplicate and the quantitative method selected was the fundamental parameters.

Nanoparticle size and morphology were evaluated via transmission electron microscopy (TEM; JEOL, JEM-2100 Plus, USA).

Crystal size and phase identification were determined by X-ray diffraction (XRD), using a Bruker D8-Advance diffractometer (Bruker-AXS GmbH, Karlsruhe, Germany) with Cu  $K\alpha$  radiation. Measurements were recorded for  $2\theta$  values from 20 to 80°. Using the broadening of the peaks it was possible to estimate the crystallite size by the Scherrer equation:

$$D_{(hkl)} = K\lambda / \beta \cos\theta$$

where  $D$  is the mean crystal size of the nanoparticles,  $K$  the Scherrer constant (0.94 for spherical crystals with cubic symmetry),  $\lambda$  the wavelength of light used for the diffraction (0.154184 nm to Cu),  $\beta$  the full width at half maximum of the peak, and  $\theta$  refers to the angle measured.

The coated and uncoated magnetite nanoparticles were suspended in deionized water and dispersed using an ultrasonic processor (model 705 Sonic Dismembrator, Fisher Scientific, USA) under 50% amplitude for 15 min, with 30 s interval every minute, at 1, 10, 100 and 1 000 mg Fe  $L^{-1}$ . The hydrodynamic size and the zeta potential of the nanomaterials at 100 mg Fe  $L^{-1}$  were analyzed via dynamic light scattering (DLS; Zetasizer Nano, Malvern Instruments, UK).

### 3.2.3 Germination assay

The effects of  $n\text{Fe}_3\text{O}_4$  and  $n\text{Fe}_3\text{O}_4\text{-PEG}$  on the germination of *Phaseolus vulgaris* L. seeds were evaluated. Since one-third of the Fe atoms in magnetite occurs as  $\text{Fe}^{2+}$  and two-thirds occur as  $\text{Fe}^{3+}$ ,<sup>31</sup> an iron ionic reference treatment (herein referred as soluble-Fe) was prepared as a mixture of one-third of  $\text{FeSO}_4 \cdot 7\text{H}_2\text{O}$  and two-thirds of  $\text{Fe}_2(\text{SO}_4)_3 \cdot n\text{H}_2\text{O}$ , both purchased from Reagen (Brazil).

*Phaseolus vulgaris* L. seeds, cultivar Sintonia, were supplied by the Agronomic Institute of Campinas (IAC), presented an average germination rate of 80%. This seed was chosen as model species because of its low dormancy, which results in a plant of small size and short growth cycle, i.e. an ideal test case. In addition, *P. vulgaris* is an important and accessible source of protein.<sup>32</sup>

Seeds were first immersed in a 10% NaClO solution under stirring for 10 s for disinfection, followed by rinsing with deionized water. Subsequently, twenty seeds were soaked for 20 min in the appropriate concentration of nFe<sub>3</sub>O<sub>4</sub> and nFe<sub>3</sub>O<sub>4</sub>-PEG dispersions. Soluble-Fe solutions at the same concentrations were used as a positive control, whereas deionized water was used as a negative control. After exposure, the seeds were placed on a 15-cm paper filter fitted on the bottom of a Petri dish, and 8 mL of the soaking solution was added to moisturize the paper filter. The Petri dishes were sealed with Parafilm M (Bemis Company Inc., USA), inserted into a plastic bag preventing water loss, and finally incubated in a germination chamber (TE-4020, Tecnal, BR) under dark and ventilation at 27 °C for five days. Five replicates of the experiment were conducted per treatment.

Five days after the sowing the assay was completed and the number of germinated seeds counted to determine the rate of germination. The radicle length of the seedlings was measured, manually removed and weighted. Afterwards, radicles and seeds were both rinsed with deionized water to remove the surface-bound metal or nano metal oxide and then dried in a laboratory oven (515/4A, FANEM, Brazil) at 60 °C for two days.

### **3.2.4 Radicle length determination**

At the end of the germination period, the five replicates of seedlings from each treatment were separately transferred to a black cardboard, then a HP Scanjet 2410 scanner operated by Photosmart software was used to obtain scanned images of the seedlings. The radicle length (cm) of the seedlings was determined through the digitized images using the Seed Vigor Imaging System software (SVIS<sup>®</sup>).<sup>33</sup>

### **3.2.5 Iron uptake quantification**

Each treatment replicates were grouped and the dried seedlings carefully separated in three fractions: cotyledon, seed coat and radicle. The cotyledons were then ground using a mortar mill (MA890, Marconi, Brazil). One gram of each component was weighed in a decontaminated porcelain crucible and then digested by dry ashing method using a muffle

furnace (F-2, Fornitec, Brazil) at  $100\text{ }^{\circ}\text{C h}^{-1}$  ramp rate up to  $550^{\circ}\text{C}$  and then ashed for 14 h. Each dry ashing digestion batch included a blank to ensure no contamination. The ashes were dissolved in 5 mL of 1 M  $\text{HNO}_{3(\text{aq})}$ , then 200  $\mu\text{L}$  of this solution plus 750  $\mu\text{L}$  of ultra pure water was transferred into a 1.5 mL vial, and 50  $\mu\text{L}$  of 1 000 mg Ga  $\text{L}^{-1}$  was added as an internal standard. Then, the sample was homogenized using a tube shaker vortex (MA162, Marconi, Brazil).

The Fe content of the digested samples was determined by EDXRF. For that, 10  $\mu\text{L}$  of the digests were pipetted on the external side of the window of a 6.3 mm XRF sample cup (no. 3577 - Spex Ind. Inc., USA) and sealed with a 5  $\mu\text{m}$  thick polypropylene film (no. 3520 - Spex Ind. Inc., USA). The cups were then left drying in a laboratory oven at  $60^{\circ}\text{C}$ . The samples were triplicate analyzed using a rhodium (Rh) X-ray tube at 50 kV and auto-tunable current with a deadtime at 30% and a 3-mm collimator. The X-ray spectrum of the sample was acquired utilizing a Si (Li) detector for 200 s. The quantification was performed using external standard calibration. The trueness of this method was assessed analyzing two certified reference materials: apple leaves (NIST 1515) and peach leaves (NIST 1547).

### 3.2.6 $\text{nFe}_3\text{O}_4$ solubility

To verify the Fe solubility of  $\text{nFe}_3\text{O}_4$  and  $\text{nFe}_3\text{O}_4\text{-PEG}$ , aqueous dispersions of 15 mL were prepared at 100 and 1 000 mg Fe  $\text{L}^{-1}$  using a probe ultrasonic device (Fisher Scientific™ Model 705 Sonic Dismembrator). The equipment was operated at 95 W (amplitude of 50 %) and 50 J, during 15 x 1 min with an interval of 30 s between each cycle. After 24 hours, one milliliter of each dispersion was transferred to Eppendorf tubes and then centrifuged by a microcentrifuge (Mikro 120, Hettich, Germany) for 60 minutes at 13 000 rpm.

Quantitative analysis of the supernatants was performed by EDXRF (EDX-720, Shimadzu, Japan). Fifteen milliliters of the supernatants were dripped in a 6.3 window cuvette (no. 3577 - Spex Ind. Inc., USA) assembled with a five micrometer thick polypropylene film, and dried at  $60^{\circ}\text{C}$  in a laboratory oven. After repeating this procedure twice, the samples were measured using the same experimental condition of  $\text{nFe}_3\text{O}_4$  characterization. The quantification was performed using external standard calibration and Ga as internal standard. The measurements were performed in triplicate.

### 3.2.7 Mapping Fe accumulation spots

The seeds were exposed to  $n\text{Fe}_3\text{O}_4$ ,  $n\text{Fe}_3\text{O}_4\text{-PEG}$  and soluble-Fe at  $1\,000\text{ mg Fe L}^{-1}$  for 20 min, dried at room temperature and gently cut in the middle using a stainless steel blade. Subsequently, the seeds were placed on a sample holder with a Kapton tape and the cotyledon's inner side exposed for analysis.

The microanalysis was carried out using a benchtop microprobe X-ray fluorescence spectrometer ( $\mu\text{-XRF}$ ) system (Orbis PC EDAX, USA) operated with a Rh X-ray tube at 40 kV and  $300\ \mu\text{A}$  and using a  $25\ \mu\text{m}$  Ni filter. A polycapillary optic provided a  $30\ \mu\text{m}$  X-ray beam spot size. The detection was carried out by a  $30\ \text{mm}^2$  silicon drift detector (140 eV FWHM at the 5.9 keV Mn-K $\alpha$  line) with a deadtime of nearly 3%. Maps were registered using a matrix of  $64 \times 50$  pixels (number of analyzed points on xy- axes) and dwell time per pixel of 1 s.

Additionally, scanning electron microscopy (SEM) images were recorded using a JEOL JSM-5600LV SEM. The hilum of the bean seeds was removed using a razor blade and transversally cut. The samples were coated with Au and placed in the stubs for measurements. The chemical composition of specific parts of the imaged tissues were determined using the X-ray energy disperse detector (EDX) of the microscope.

### 3.2.8 3D distribution and chemical speciation of Fe in the hilum

Common beans have a hilum associated to the seed coat, and near the hilum there is the micropyle, a small pore that allows water uptake into the seed.<sup>34</sup> We employed X-ray tomography to verify the 3D distribution of Fe in the hilum region of treated seeds, and the chemical speciation of Fe in the hilum was performed by means of X-ray absorption near edge spectroscopy (XANES).

Common bean seeds were exposed to  $n\text{Fe}_3\text{O}_4\text{-PEG}$  and soluble-Fe at  $1\,000\text{ mg Fe L}^{-1}$  for 20 min and dried at room temperature. A small fraction of the seed coat containing the hilum were carefully collected and cut using a razor blade.

Tomograms were acquired at the X-ray imaging beamline (IMX) at the 1.37 GeV Brazilian Synchrotron Light Laboratory (LNLS, Campinas, Brazil). At IMX beamline, synchrotron radiation was generated by a bending-magnet. The measurements were carried out using a pink beam from 4 to 14 keV and 1024 projections were taken under  $180^\circ$  rotation. The exposure time was 300 ms per projection. The image was magnified and focused on a

cooled camera detector (CCD; PCO.2000, PCO, Germany). Pictures of the sample holders containing the seed coat fractions and the experimental X-ray tomography setup are presented in the electronic Supporting Information of Duran et al.<sup>35</sup>

To complement these data, the same samples were also submitted to  $\mu$ -XRF mapping. The analysis parameters and experimental setup were the same as above mentioned (mapping Fe accumulation spots).

The XANES measurements were carried out at the Fe K edge in fluorescence mode at XAFS2 beamline of LNLS (Brazil). At this experimental station the X-rays are generated by dipole bending magnet, the higher harmonics are rejected by a set of mirrors, the energy was selected by a Si(111) monochromator and the X-ray beam was focused to a spot of *ca.* 500  $\mu\text{m}$  by a Rh coated mirror. The fluorescence was detected by a 15 element Ge solid state Canberra detector. The spectra were energy calibrated using a Fe foil, normalized and subjected to linear combination analysis from -20 to 50 eV above the edge. The reference compounds were  $n\text{Fe}_3\text{O}_4$ -PEG and the pristine bean. We also measured pelletized  $n\text{Fe}_3\text{O}_4$  and iron (II) and (III) sulfates. The analysis was accomplished using the IFEFFIT code.<sup>36</sup>

### 3.2.9 Reactivity of soluble-Fe and magnetite nanoparticles

The reactivity of the soluble-Fe and magnetite nanoparticles was evaluated measuring their ability to decompose  $\text{H}_2\text{O}_2$ <sup>37</sup> through a Fenton-like reaction.<sup>38</sup> In a 25 mL round-bottom reaction flask, 19.5 mL of a 1 000 mg Fe  $\text{L}^{-1}$  aqueous dispersion of the tested nanoparticles and soluble-Fe solution was magnetically stirred. The flask was connected to a 25 mL graduated pipette through a silicone tube. The pipette was immersed in a measuring cylinder water column. Then, 0.5 mL of 30% v/v  $\text{H}_2\text{O}_2$  solution was inserted in the reaction flask with a syringe. The volume of the produced  $\text{O}_2$  was monitored by following the shift of a water column in pipette.

### 3.2.10 $\alpha$ -amylase activity

The evaluations for the  $\alpha$ -amylase enzyme followed the recommendations of Fuwa.<sup>39</sup> *P. vulgaris* seeds were soaked in  $n\text{Fe}_3\text{O}_4$ ,  $n\text{Fe}_3\text{O}_4$ -PEG and soluble-Fe at 1 000 mg Fe  $\text{L}^{-1}$  for 20 min and then germinated in paper rolls inside a germination chamber (Mangelsdorf, DeLeo, Brazil) at 25°C. The experiment was quadruplicate conducted with 20 seeds per replicate. The seedlings were collected on the 7<sup>th</sup> day after sowing, subsequently nearly 1 g were weighed and macerated using a mortar and pestle in a phosphate buffer solution (pH 6.9)

at a 9:1 (distilled water: buffer) ratio. This material was centrifuged for 4 min at 12 000 g (NT 805, Novatecnica, Brazil), then the supernatant was removed for the enzymatic analysis, and 1% starch solution was used as substrate. The value of 1 U (Enzymatic Unit) was considered to be the reduction of 10% of the colorimetric intensity of the amylose-iodine complex.

### 3.2.11 Statistical analysis

The number of germinated seeds and the radicle length and weight data were submitted to analysis of variance (ANOVA) and Tukey's multiple range tests at 95% confidence interval using the Action Stat software (version 3.3.111.1178, Estatcamp, BR).

## 3.3 Results and Discussion

### 3.3.1 Characterization of the nanoparticles and dispersions

The purity of the  $n\text{Fe}_3\text{O}_4$  and  $\text{Fe}_3\text{O}_4\text{-PEG}$  was determined by EDXRF. Considering the limits of detection of the method, *ca.* of  $\text{mg kg}^{-1}$ , no contaminants were found in the nanoparticles. Figure 3.1 presents the XRF spectra of these samples. XRD patterns, presented in Figure 3.2, showed an average crystallite size in the direction of the plane (220) of 11.6 nm for the uncoated and 13.9 nm for coated magnetite nanoparticles, respectively (see the crystallite size in the direction of the other planes in Table 3.1). These results were in agreement with the transmission electron microscopy (TEM) observations (Figure 3.3), with presumed average particle size of 11 nm for  $n\text{Fe}_3\text{O}_4$  and 12 nm for  $\text{Fe}_3\text{O}_4\text{-PEG}$ .

Figure 3.1 - XRF Spectra of the magnetite nanomaterials used in this study. A)  $n\text{Fe}_3\text{O}_4$  and B)  $n\text{Fe}_3\text{O}_4\text{-PEG}$

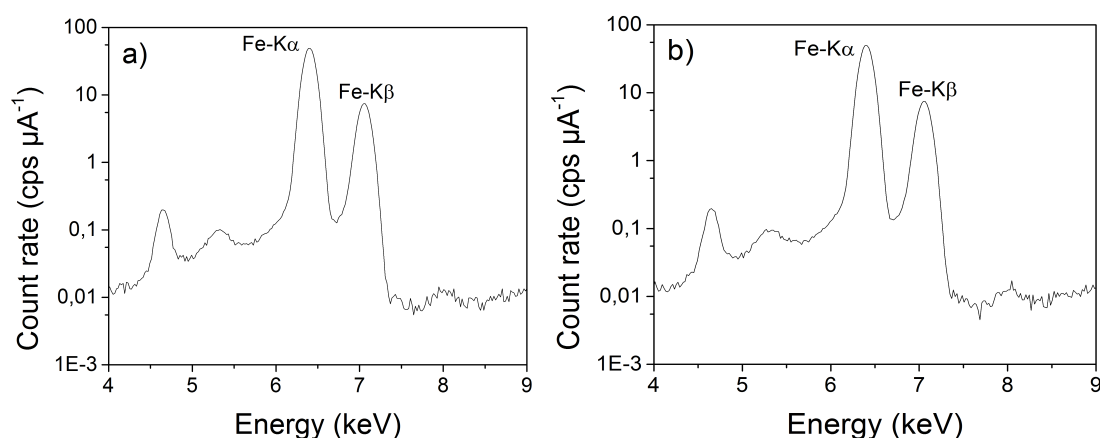
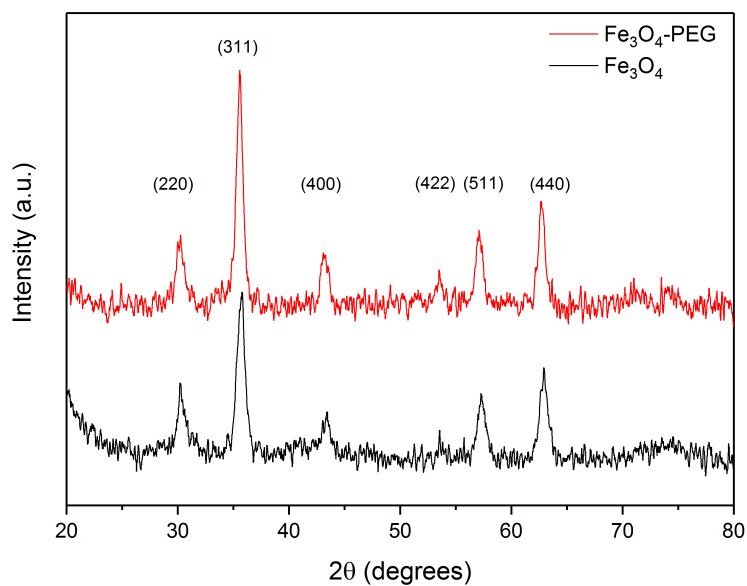
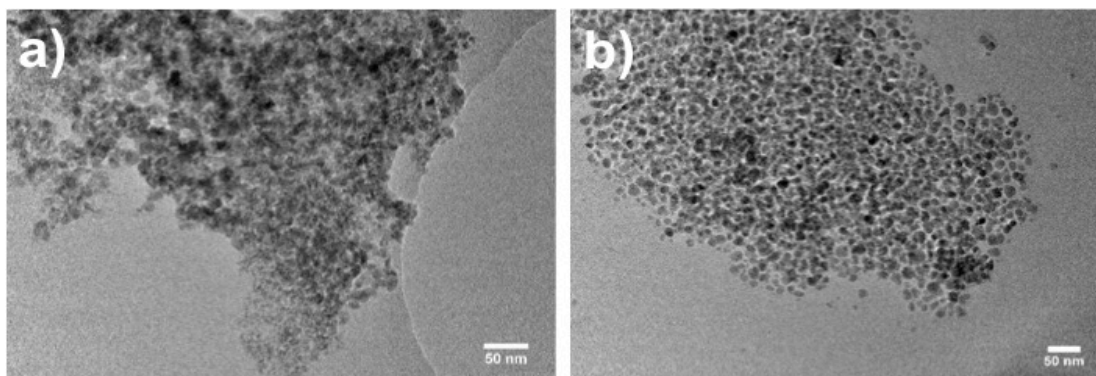
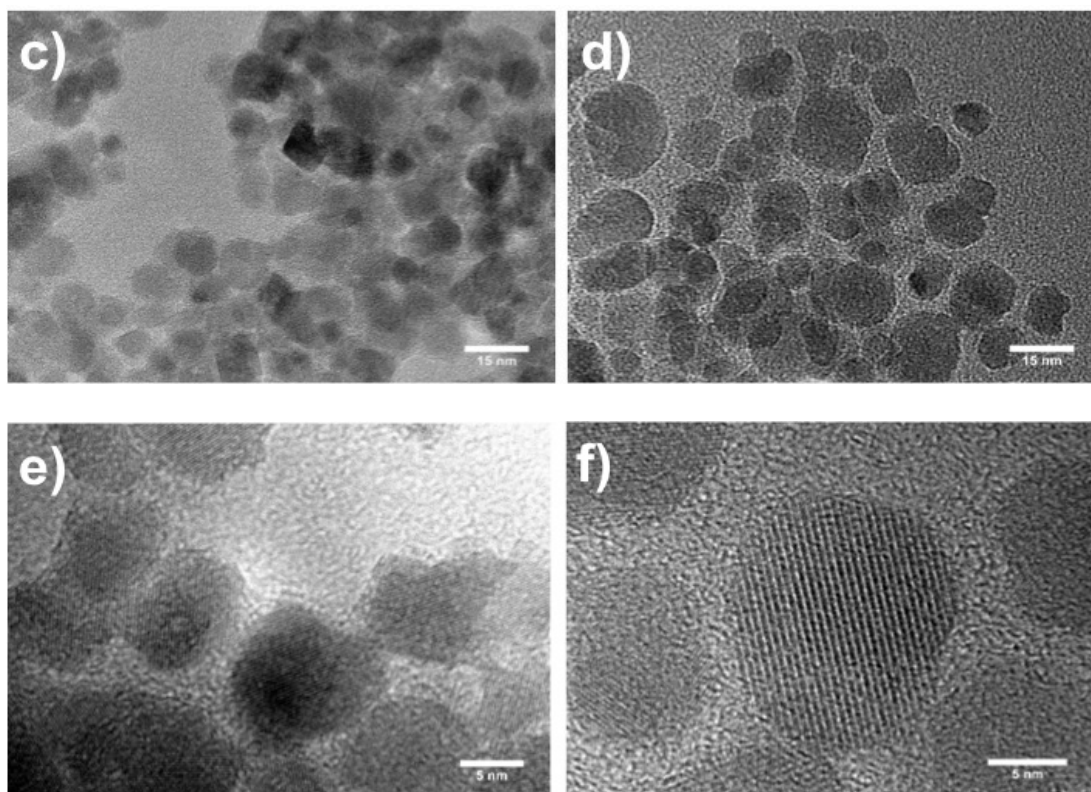


Figure 3.2 - XRD patterns for  $n\text{Fe}_3\text{O}_4$  and  $n\text{Fe}_3\text{O}_4\text{-PEG}$ Table 3.1 - Crystallite size ( $D$ ) of  $n\text{Fe}_3\text{O}_4$  and  $n\text{Fe}_3\text{O}_4\text{-PEG}$  in different planes

Plane	$D_{(hkl)}$ (nm)	
	$n\text{Fe}_3\text{O}_4$	$n\text{Fe}_3\text{O}_4\text{-PEG}$
220	11.59	13.93
311	13.29	14.07
400	13.05	13.29
422	-	14.12
511	11.68	14.94
440	16.10	17.05

Figure 3.3 - Size and morphology of magnetite nanoparticles observed by transmission electron microscopy of  $n\text{Fe}_3\text{O}_4$  (a, c and e) and  $n\text{Fe}_3\text{O}_4\text{-PEG}$  (b, d and f). Scale bar of (a) and (b): 50 nm; (c) and (d): 15 nm; (e) and (f): 5 nm



The DLS measurements (Table 3.2) revealed the hydrodynamic diameter of the nanoparticles in aqueous dispersion. The discrepancy between nanoparticle size shown by TEM and that measured by the DLS indicates particle aggregation. Such behavior and aggregate sizes are in agreement with reported values of  $208 \pm 15$  nm for 50-60 nm  $n\text{Fe}_3\text{O}_4$  suspended in water at  $10 \text{ mg L}^{-1}$  and  $438 \pm 13$  nm at  $20 \text{ mg L}^{-1}$ .<sup>22</sup> One could visually observe that such aggregates make these magnetite dispersions very unstable. At  $1000 \text{ mg Fe L}^{-1}$ , most particles were settled after 60 min, even in the  $n\text{Fe}_3\text{O}_4$ -PEG case.

The aggregation is controlled by an equilibrium between particles attraction (Van der Waals forces) and repulsion (surface charges or steric hindrance).<sup>40;41</sup> The pH registered for the uncoated magnetite dispersion and coated one were 5.58, and 5.08, respectively. Normally, for a same material lower pH values should lead to more positive zeta potentials.<sup>42</sup> Zeta-potential measurements indicated that the uncoated magnetite presented a negative value, whereas the PEG coated presented positive value. Thus, the sign of surface charges of  $\text{Fe}_3\text{O}_4$ -PEG was determined by the coating rather than by the pH. The measured  $\zeta$ -potential for the uncoated samples was different from values reported in the literature,  $4.31 \pm 0.05$  mV for the less concentrated dispersion ( $10 \text{ mg L}^{-1}$ ) and  $3.99 \pm 0.4$  mV for the highest one ( $20 \text{ mg L}^{-1}$ ).<sup>22</sup>

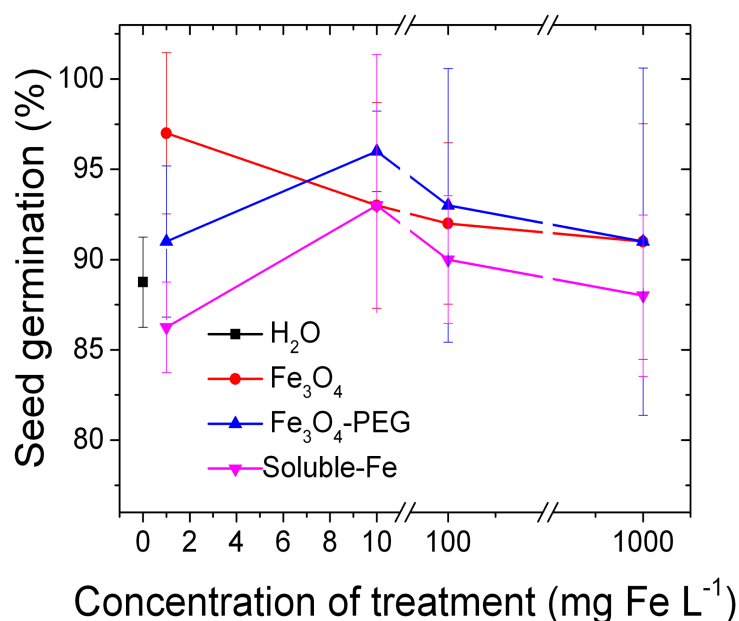
Table 3.2 - Zeta potential and hydrodynamic diameter of  $n\text{Fe}_3\text{O}_4$  and  $n\text{Fe}_3\text{O}_4\text{-PEG}$  dispersions determined by dynamic light scattering (DLS)

Magnetite type	Zeta-potential (mV)	Hydrodynamic Diameter (nm)		
		Peak 1	Peak 2	Peak 3
$n\text{Fe}_3\text{O}_4$	$-14 \pm 7$	$71 \pm 10$ (12%)	$310 \pm 60$ (88%)	--
$n\text{Fe}_3\text{O}_4\text{-PEG}$	$9 \pm 6$	$170 \pm 60$ (54%)	$480 \pm 150$ (41%)	$2\,700 \pm 160$ (5%)

### 3.3.2 Effects of magnetite nanoparticles on *P. vulgaris* seed germination and radicle growth

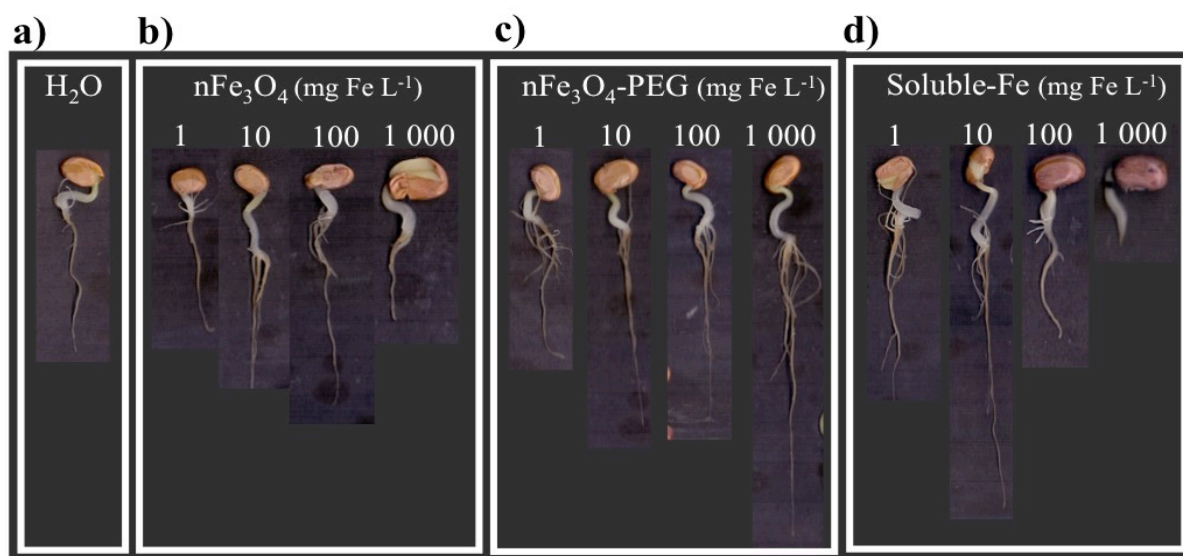
The number of germinated seeds was counted daily and all the radicles emerged almost in the same period. At the end of the germination assay, the deionized water treatment control gave an average germination rate of 88.8% (Figure 3.4). All the others treatments had higher or comparable values to the negative control. The highest germination rate was found for  $1\text{ mg Fe L}^{-1}$  of  $n\text{Fe}_3\text{O}_4$  and  $10\text{ mg Fe L}^{-1}$  of  $n\text{Fe}_3\text{O}_4\text{-PEG}$  (97 and 96%, respectively). However, under ANOVA statistical analysis, no difference was found among treatments and controls ( $p < 0.05$ ).

Figure 3.4 - Germination rate of *P. vulgaris* seeds exposed to  $n\text{Fe}_3\text{O}_4$ ,  $n\text{Fe}_3\text{O}_4\text{-PEG}$ , soluble-Fe (1, 10, 100 and 1 000  $\text{mg Fe L}^{-1}$ ) and  $\text{H}_2\text{O}$  after 5 days of germination



Although the treatments did not affect the germination rate, a different scenario was observed in the radicle elongation of the seedlings. The phenotypic images of the seedlings after 5 days of Fe treatments exposure (Figure 3.5) indicate that the highest applied concentration was toxic for the seedlings development, while it was not observed for the  $n\text{Fe}_3\text{O}_4$ -PEG treatment.

Figure 3.5 - Seedlings of *P. vulgaris* whose seeds were soaked in (a)  $\text{H}_2\text{O}$ , (b)  $n\text{Fe}_3\text{O}_4$ , (c)  $n\text{Fe}_3\text{O}_4$ -PEG and (d) soluble-Fe. Applied concentrations were 1, 10, 100 and 1 000  $\text{mg Fe L}^{-1}$



The average length of the radicle of negative control was  $5.9 \pm 1.0$  cm long, whilst  $n\text{Fe}_3\text{O}_4$  and soluble-Fe at  $1\,000\text{ mg Fe L}^{-1}$  shortened it, yielding  $2.9 \pm 0.5$  and  $1.2 \pm 0.3$  cm, respectively. Conversely, PEG improved the radicle development even at its higher concentration, where the highest radicle elongation of  $8.1 \pm 1.1$  cm was observed (Figure 3.6a). One of the hypotheses to explain this result regards the hydrophilic nature of the PEG.<sup>43</sup> The polymeric coating might have reduced the water potential, which caused greater water absorption by the tissues. If so, it may have aided the root growth by redirecting water to a region close to the root of the seedlings. Furthermore, the nanoparticles distribution on seed coat was more homogeneous where PEG was added. This allowed a controlled absorption of  $n\text{Fe}_3\text{O}_4$ , by reducing the water surface tension.<sup>44</sup>

After the length measurements, the radicles were removed and weighed (Figure 3.6b). The same trend was observed for length and weight, radicles from water treatment presented  $1.94 \pm 0.13$  g and  $n\text{Fe}_3\text{O}_4$  at  $1\,000\text{ mg Fe L}^{-1}$  had  $0.82 \pm 0.09$  g. According to the Tukey's test ( $p < 0.05$ ), radicle length was significantly different from the control at  $1\,000\text{ mg Fe L}^{-1}$  for all

the tested materials, positively for nFe<sub>3</sub>O<sub>4</sub>-PEG and negatively for nFe<sub>3</sub>O<sub>4</sub> and soluble-Fe treatments (Figure 3.7). However, radicle weight data were only statistically different from control for nFe<sub>3</sub>O<sub>4</sub> and soluble-Fe at 1 000 mg Fe L<sup>-1</sup> (Figure 3.8).

Figure 3.6 - (a) Radicle length and (b) weight of *P. vulgaris* seedlings whose seeds were soaked in nFe<sub>3</sub>O<sub>4</sub>, nFe<sub>3</sub>O<sub>4</sub>-PEG, soluble-Fe (1, 10, 100 and 1 000 mg Fe L<sup>-1</sup>) and H<sub>2</sub>O (control)

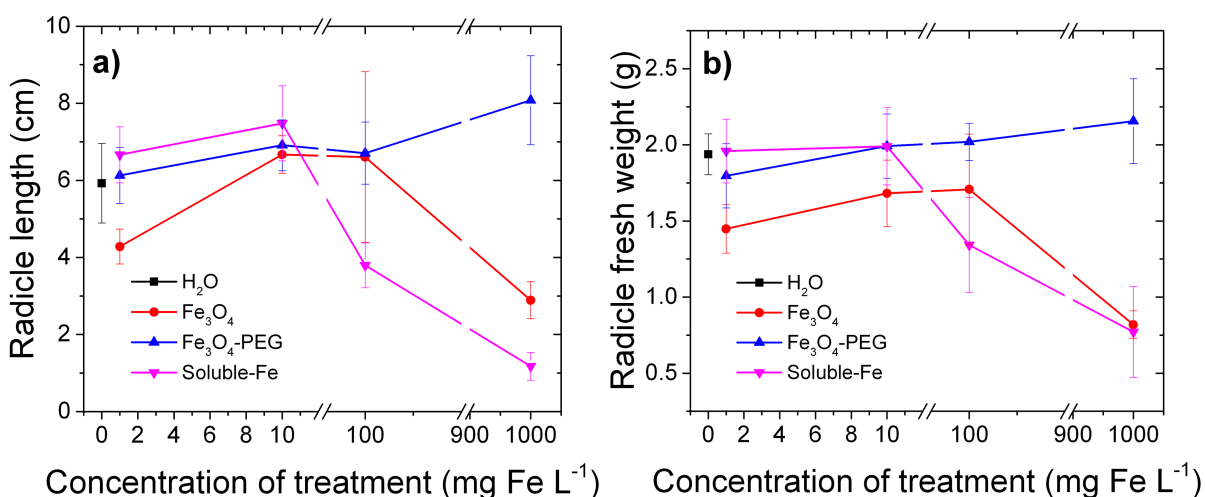


Figure 3.7 - Radicle length of *P. vulgaris* seedlings as function of the applied concentration of magnetite nanoparticles and soluble-Fe (mg Fe L<sup>-1</sup>). The data points followed by the same letter were significantly different according to the Tukey test ( $p < 0.05$ )

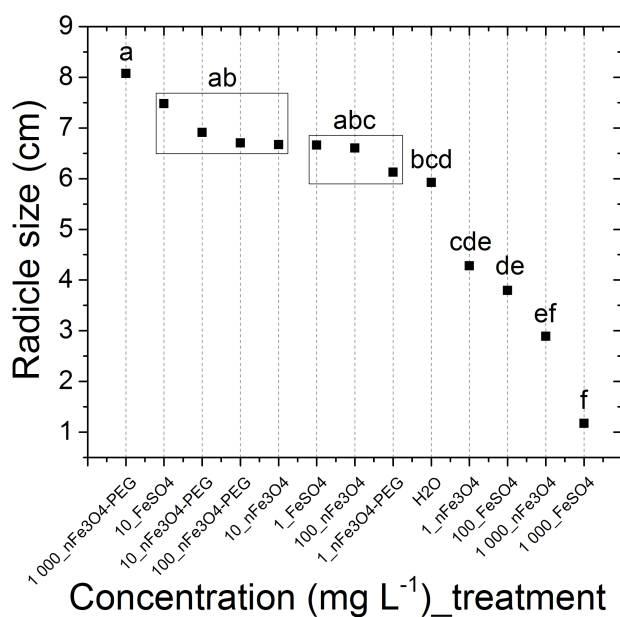
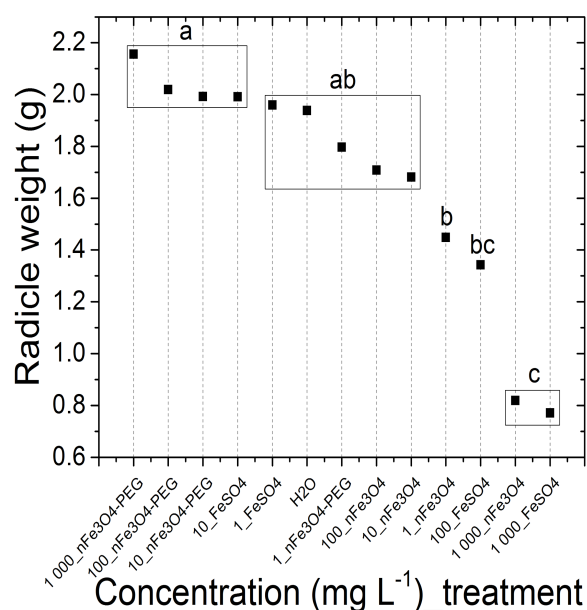


Figure 3.8 - Radicle weight of *P. vulgaris* seedlings as function of the applied concentration of magnetite nanoparticles and soluble-Fe (mg Fe L<sup>-1</sup>). The data points followed by the same letter were significantly different according to the Tukey ( $p < 0.05$ )



The phytotoxicity observed for high concentrations of soluble-Fe and nFe<sub>3</sub>O<sub>4</sub> might be related to the Fe accumulation in the seed tissues. Such conclusion is reinforced by the fact that the absorption of soluble-Fe occurs mainly by the micropyle, determinant structure for water imbibition by seeds,<sup>45</sup> mainly in the initial stages of the germination process as will be discussed in depth below.

Studies reported root shortening as a response to the increase of nanoparticles concentration in the dispersion, as demonstrated for ZnO,<sup>46; 47</sup> Ag,<sup>48</sup> CuO<sup>17; 49</sup> and TiO<sub>2</sub>.<sup>50</sup> The anomalous behavior found for Fe in the present study was also observed for white mustard, where the root elongation of the seedlings treated with the highest nFe<sub>3</sub>O<sub>4</sub> concentrations (100 and 1 000 mg L<sup>-1</sup>) was higher than the lower tested concentration (10 mg L<sup>-1</sup>), however the difference was not statistically significant.<sup>25</sup> On the other hand, soybean and rice seeds treated with  $\gamma$ -Fe<sub>2</sub>O<sub>3</sub> nanoparticles at 500, 1 000 and 2 000 mg L<sup>-1</sup> developed seedlings with the root elongation significantly higher than the control.<sup>51; 52</sup>

Nano zerovalent iron at 5 000 mg L<sup>-1</sup> also promoted the root elongation of *Arabidopsis thaliana* by 150-200% compared to the control, with the elongation caused by hydroxyl radical-induced cell-wall loosening.<sup>53</sup> Other authors observed that  $\gamma$ -Fe<sub>2</sub>O<sub>3</sub> nanoparticles promoted the growth of peanut by regulating the antioxidant enzyme activity and the content

of abscisic acid, a phytohormone that stimulates the senescence and reduces the metabolism. The peanut root dry biomass was increased by  $\text{Fe}_2\text{O}_3$  nanoparticles at  $1\ 000\ \text{mg}\ \text{kg}^{-1}$  applied to the soil.<sup>54</sup>

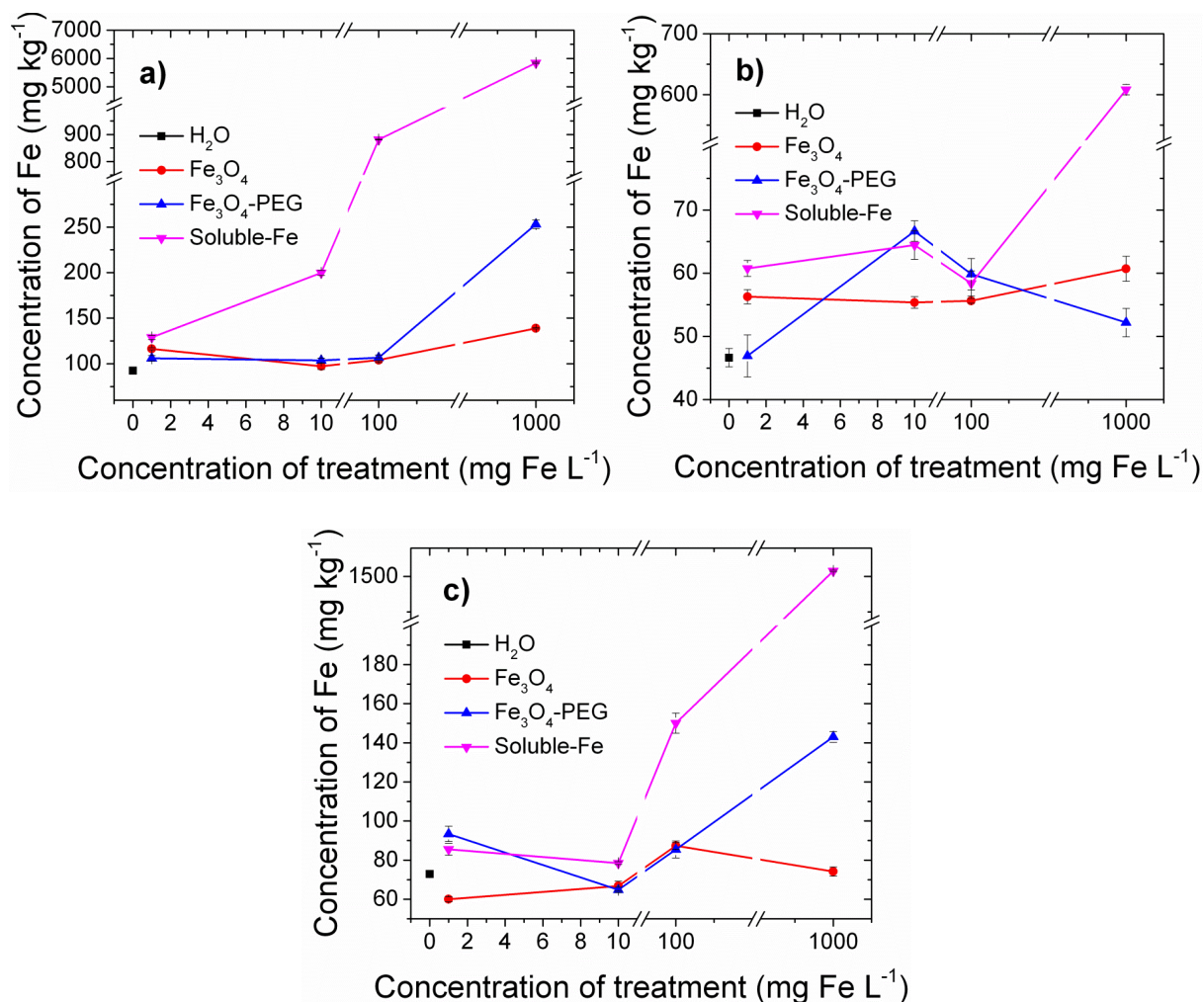
Since PEG is hydrophilic, it can prevent the  $\text{nFe}_3\text{O}_4$ -PEG from interacting with cells and/or proteins.<sup>30</sup> The surface chemistry modification of iron oxide nanoparticles by PEG reduced the cytotoxicity and the formation of reactive oxygen species (ROS), the cell length being not affected compared to the ones treated with bare nanoparticles.<sup>55</sup> Also, it was previously shown that the uptake of PEG-coated magnetite by macrophage cells was much lower than that of uncoated nanoparticles.<sup>23; 24</sup>

### 3.3.3 Determination of Fe uptake by *P. vulgaris* seeds

After the germination assays, the seedling tissues were divided and the Fe content was determined. Figure 3.9 presents the concentration of Fe in the (a) seed coat, (b) cotyledon and (c) radicle of the seedlings exposed to  $\text{nFe}_3\text{O}_4$ ,  $\text{nFe}_3\text{O}_4$ -PEG, soluble-Fe and water negative control.

The negative control (deionized water) revealed that Fe was more concentrated in the seed coat of the tested common beans than in the other tissues analyzed. It presented  $92.3 \pm 0.6\ \text{mg}\ \text{Fe}\ \text{kg}^{-1}$  in contrast to  $46.6 \pm 1.4\ \text{mg}\ \text{Fe}\ \text{kg}^{-1}$  in the cotyledons and  $72.8 \pm 0.5\ \text{mg}\ \text{Fe}\ \text{kg}^{-1}$  in the radicle. In the case of the seedlings with nanoparticle treatment, the ones soaked in  $\text{nFe}_3\text{O}_4$  presented similar Fe content in the three analyzed regions regardless of the applied concentration. The difference between the water control and  $\text{nFe}_3\text{O}_4$  treatment reached a maximum value of 50% in the seed coat sample soaked in  $1\ 000\ \text{mg}\ \text{Fe}\ \text{L}^{-1}$ . It reached more than 6000-fold higher for the soluble-Fe treatment. For the highest treatment concentration, the incorporation of Fe from the  $\text{nFe}_3\text{O}_4$ -PEG in the seed coat and in the radicle was intermediate between those of  $\text{nFe}_3\text{O}_4$  and soluble-Fe.

Figure 3.9 - Iron concentration in the (a) seed coat, (b) cotyledon and (c) radicle of germinated *P. vulgaris* seeds soaked in  $n\text{Fe}_3\text{O}_4$ ,  $n\text{Fe}_3\text{O}_4\text{-PEG}$  and soluble-Fe at  $1\,000\text{ mg Fe L}^{-1}$  and  $\text{H}_2\text{O}$



Priming rice seeds with Zn also substantially increased the Zn concentration in the husk, but not in the endosperm. This study suggests that part of the Zn accumulated in the husk during the priming process can be transported to the endosperm during the germination. It was stated since the Zn concentration declined at the same time that increased in the endosperm, and this was not the case of unprimed seeds.<sup>56</sup>

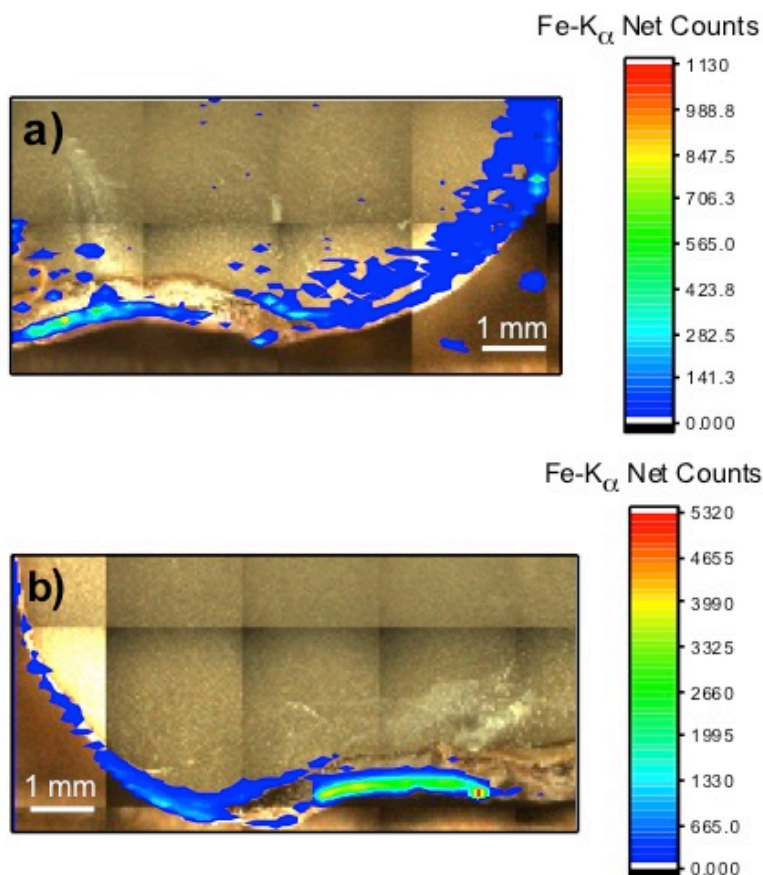
To estimate the contribution of dissolved Fe on the seedling development and Fe uptake, solubility tests in deionized water were performed. For  $n\text{Fe}_3\text{O}_4$  and  $n\text{Fe}_3\text{O}_4\text{-PEG}$  dispersions at 100 and  $1\,000\text{ mg Fe L}^{-1}$ , the soluble Fe fractions were not quantitatively detected, i.e. they were below the limit of quantification of the method ( $0.15\text{ mg Fe L}^{-1}$ ). A study carried out by Landa et al.<sup>25</sup> found soluble-Fe fractions at  $6.51 \pm 2.24\text{ mg Fe L}^{-1}$  in the supernatant of a cultivation medium supplemented with  $n\text{Fe}_3\text{O}_4$  at  $1\,000\text{ mg L}^{-1}$ .

Anyhow, it is important to keep in mind that the presence of other molecules can induce the generation of soluble complexes with Fe.

### 3.3.4 Spatial distribution and chemical speciation of Fe in the primed seeds

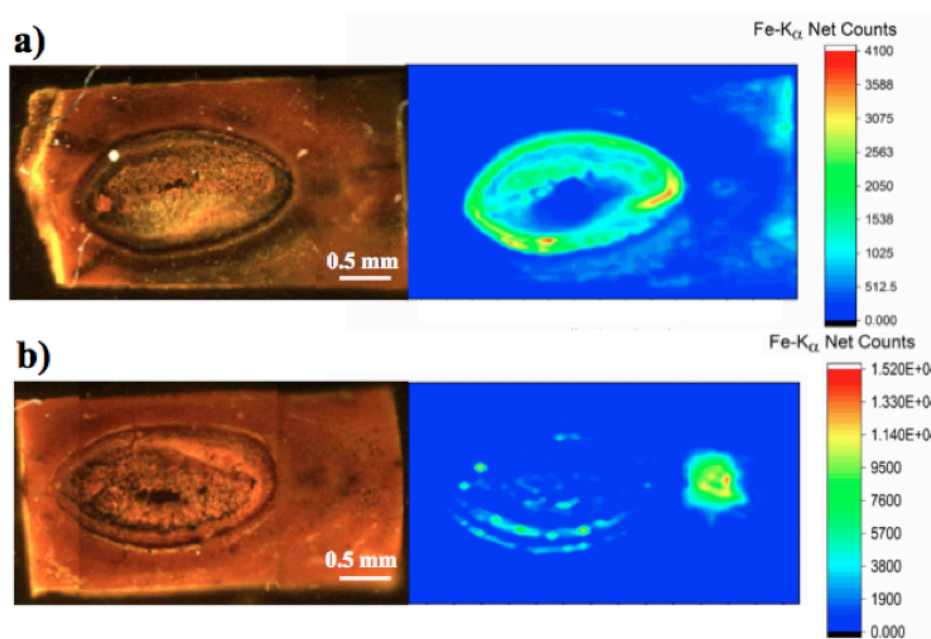
Figure 3.10 presents the internal side of the cotyledon of a *P. vulgaris* seeds soaked for 20 min in (a)  $n\text{Fe}_3\text{O}_4\text{-PEG}$  and (b) soluble-Fe at  $1\,000\text{ mg Fe L}^{-1}$ . The results corroborate the quantitative analysis, indicating that the treatments concentrated Fe in the seed coat, mainly in the hilum region, and the number of XRF counts was almost 5-fold higher for the soluble-Fe treatment compared to the nanoparticle one.

Figure 3.10 -  $\mu\text{-XRF}$  chemical maps for Fe in *P. vulgaris* seeds soaked in (a)  $n\text{Fe}_3\text{O}_4\text{-PEG}$  and (b) soluble-Fe at  $1\,000\text{ mg Fe L}^{-1}$



Additional  $\mu$ -XRF chemical maps were recorded specifically in the hilum region of the treated seeds. The images of the Fe distribution in the hilum revealed a different pattern of distribution between seeds soaked in  $n\text{Fe}_3\text{O}_4$ -PEG dispersion and soluble-Fe solution at  $1\,000\text{ mg Fe L}^{-1}$  (Figure 3.11). The nanoparticle treatment presented Fe mainly concentrated in the edge around the hilum (Figure 3.11a), while soluble-Fe presented a hotspot in the micropyle (Figure 3.11b). Another study using magnetic resonance microscopy showed that during the imbibition process, water enters the *P. vulgaris* seed through the micropyle<sup>57</sup>. Thus, we conclude that this structure acted also as a channel for soluble Fe ions.

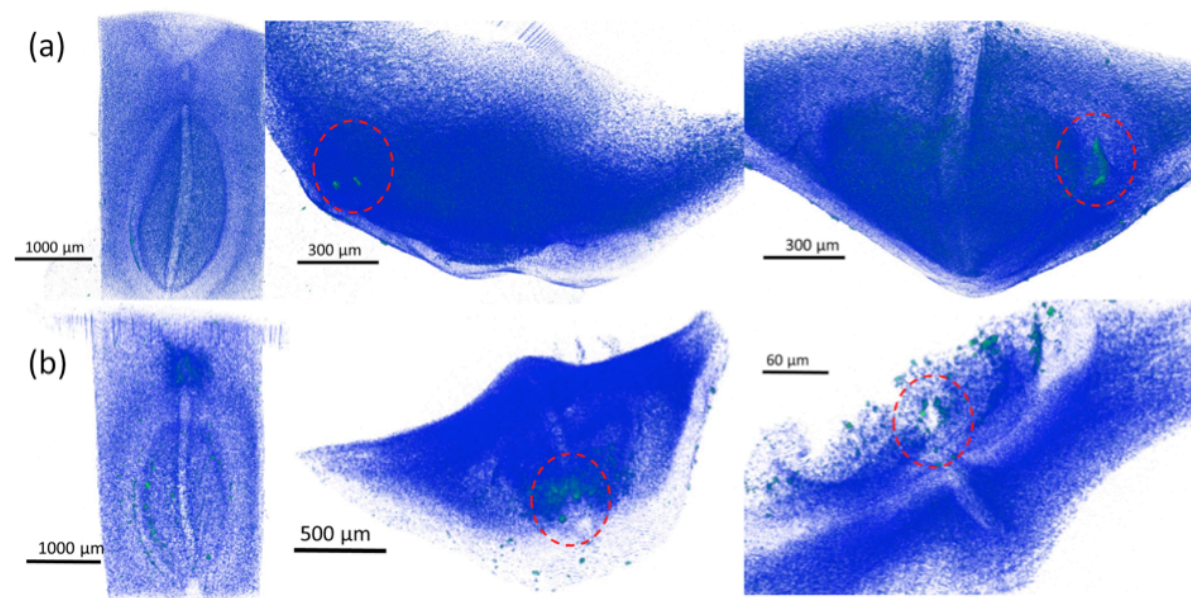
Figure 3.11 - Pictures of the hilum of *P. vulgaris* seeds soaked in (a)  $n\text{Fe}_3\text{O}_4$ -PEG and (b) soluble-Fe at  $1\,000\text{ mg Fe L}^{-1}$  and its corresponding  $\mu$ -XRF chemical maps for Fe



The hilum is a sponge-like tissue, thus besides sticking on the tissue's outer surface, the nanoparticles can penetrate through the channels reaching the seed's internal layers. In spite of X-ray fluorescence's high analytical sensitivity, it yielded only 2D maps. The 6.4 keV K $\alpha$  photons emitted by Fe atoms embedded in the seed coat can escape from a depth that lies in the mm range. Images such as these shown in Figure 3.11 cannot specify whether Fe is only adsorbed on the surface of the seed coat or also inside the hilum tissue.

Hence, the hilum region of treated seeds was subjected to further X-ray tomography analysis. Figure 3.12 shows 3D projections and slices of phase contrast tomography for the seed coat of seeds soaked in (a)  $n\text{Fe}_3\text{O}_4\text{-PEG}$  and (b) soluble-Fe at  $1\,000\text{ mg Fe L}^{-1}$  for 20 min. The green regions, highlighted by the red circles, indicate the presence of Fe that penetrated within the hilum sponge tissue. This can be observed for both  $n\text{Fe}_3\text{O}_4\text{-PEG}$  and soluble-Fe. The combination of  $\mu\text{-XRF}$  and X-ray tomography unequivocally showed that Fe supplied under nanoparticle format could enter in the seeds.

Figure 3.12 - X-ray tomograms of the hilum of a *P. vulgaris* seed treated with (a)  $\text{Fe}_3\text{O}_4\text{-PEG}$  nanoparticle and (b) soluble-Fe at  $1\,000\text{ mg Fe L}^{-1}$  dispersion for 20 min. The green spots highlighted by the red circles indicates the presence of Fe embedded in the organic tissue



X-ray tomography was previously employed to understand physiological seed development of rice,<sup>58</sup> maize<sup>59</sup> and oilseed rape,<sup>60</sup> observe germination behavior of sugar beet seeds,<sup>61</sup> and also to analyze archaeological seeds in the investigation of crop domestication.<sup>62;</sup> However, to the best of our knowledge, no other study examined 3D images of a nanoparticle-treated bean seed, although some researchers used this technique to verify the uptake and distribution of gold and yttrium nanoparticles in *Arabidopsis thaliana*<sup>64</sup> and cabbage plants.<sup>65</sup>

The chemical form of Fe trapped in the hilum was evaluated by Fe K edge XANES. Figure 3.13a shows the XANES spectra for the control bean (pristine without any treatment),  $n\text{Fe}_3\text{O}_4\text{-PEG}$ ,  $\text{Fe}_2(\text{SO}_4)_3$  and  $\text{Fe}(\text{SO}_4)$  reference compounds. The spectral features are a function of the chemical environment. The energy of the threshold depends on the oxidation state, this is the reason why  $\text{Fe}^{2+}$  ( $\text{Fe}(\text{SO}_4)$ ) is shifted towards lower energies compared to  $\text{Fe}_2(\text{SO}_4)_3$ . The threshold energy for the control bean and  $n\text{Fe}_3\text{O}_4\text{-PEG}$  fall in between  $\text{Fe}^{2+}$  and  $\text{Fe}^{3+}$ , which indicates that these two latter samples are composed of mixed iron oxidation states. This is well known for magnetite, but to the best of our knowledge it has never been reported for bean seeds.

Figure 3.13b presents the XANES spectrum for the hilum of a seed treated with  $n\text{Fe}_3\text{O}_4\text{-PEG}$  and its respective linear combination analysis fit. The Fe in the treated hilum can be defined as mixture of 75 wt%  $n\text{Fe}_3\text{O}_4\text{-PEG}$  and 25 wt% control bean. In spite of its capabilities, the XANES ability to distinguish fractions in a linear combination analysis is limited. Due to its intrinsic sensibility, XANES would hardly detected fraction below 5 wt%.<sup>66</sup> To assure that the detected Fe was not simply adsorbed on the surface of the hilum, the tissue was carefully washed and measured again. Figure 3.13c shows that after successive rinsing, the fraction of  $n\text{Fe}_3\text{O}_4\text{-PEG}$  decreased to 47 wt%. This happened because the iron particles lying on the surface were removed during the washing process.

The presence of Fe within the hilum was also confirmed by SEM-EDX. Figure 3.14 show the images for  $n\text{Fe}_3\text{O}_4\text{-PEG}$  treated hilum cross sections. It is possible to distinguish an agglomerate of particles; the EDX detector confirmed that this structure was a Fe hotspot (Figure 3.14e).

Thanks to the complementary of spectroscopic and imaging tools, we can state that the Fe structures within the hilum are magnetite particles incorporated during the seed treatment.

Figure 3.13 - (a) Fe K edge XANES spectra for the control bean (pristine without any treatment),  $n\text{Fe}_3\text{O}_4\text{-PEG}$ ,  $\text{Fe}_2(\text{SO}_4)_3$  and  $\text{Fe}(\text{SO}_4)$  reference compounds; (b) Linear combination fit for Fe K edge XANES spectrum for the hilum of a seed treated with  $n\text{Fe}_3\text{O}_4\text{-PEG}$ ; (c) Linear combination fit for the hilum of a seed treated with  $n\text{Fe}_3\text{O}_4\text{-PEG}$  after washing

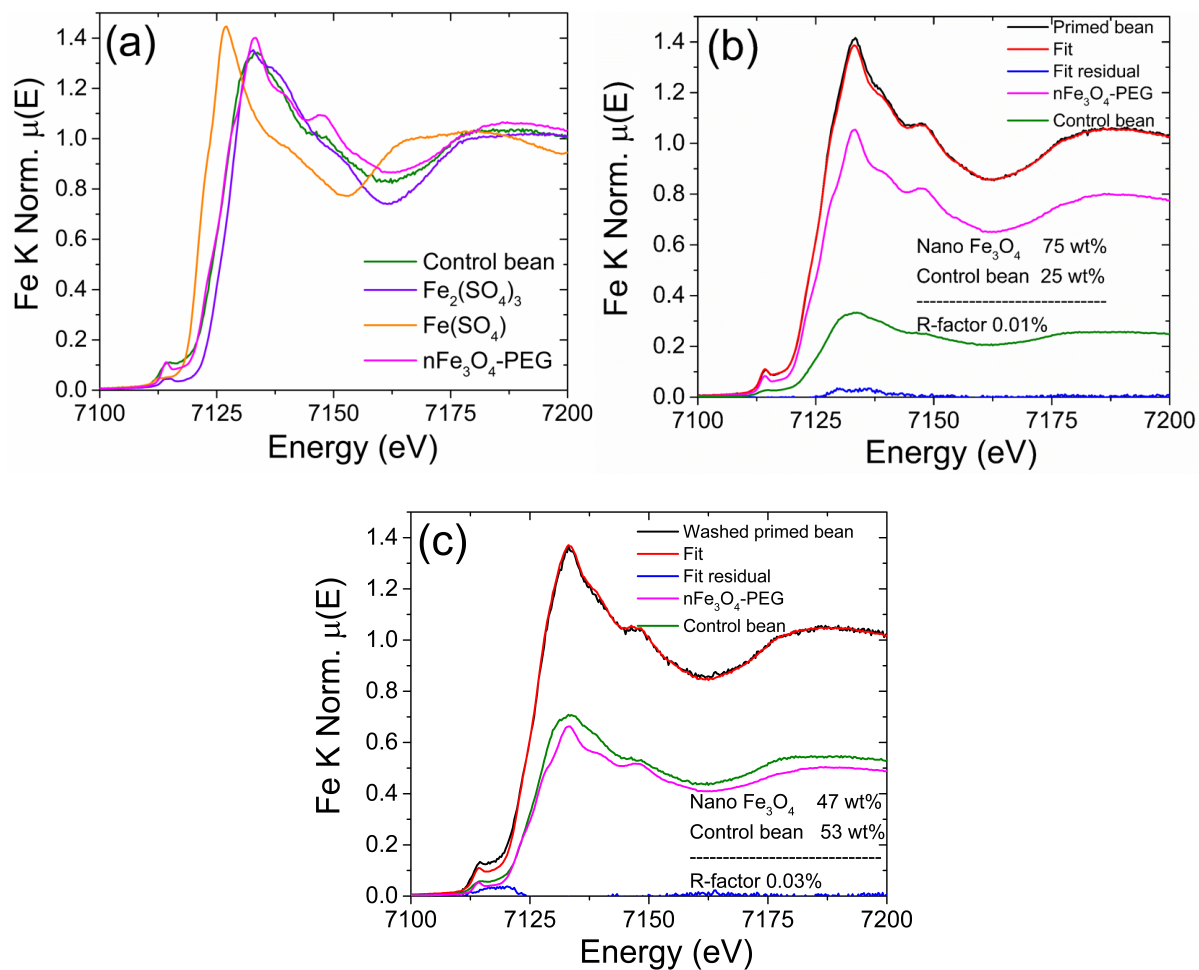
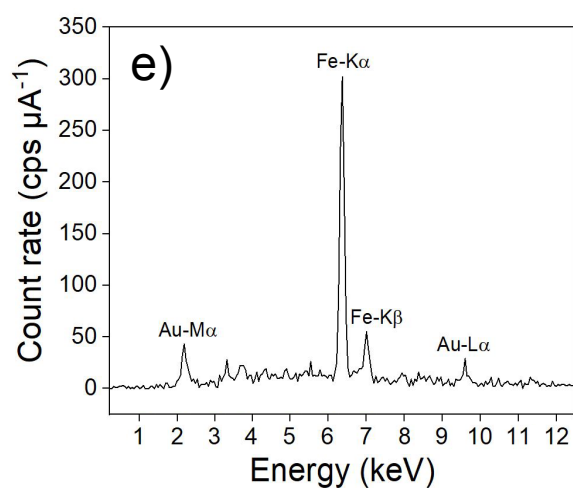
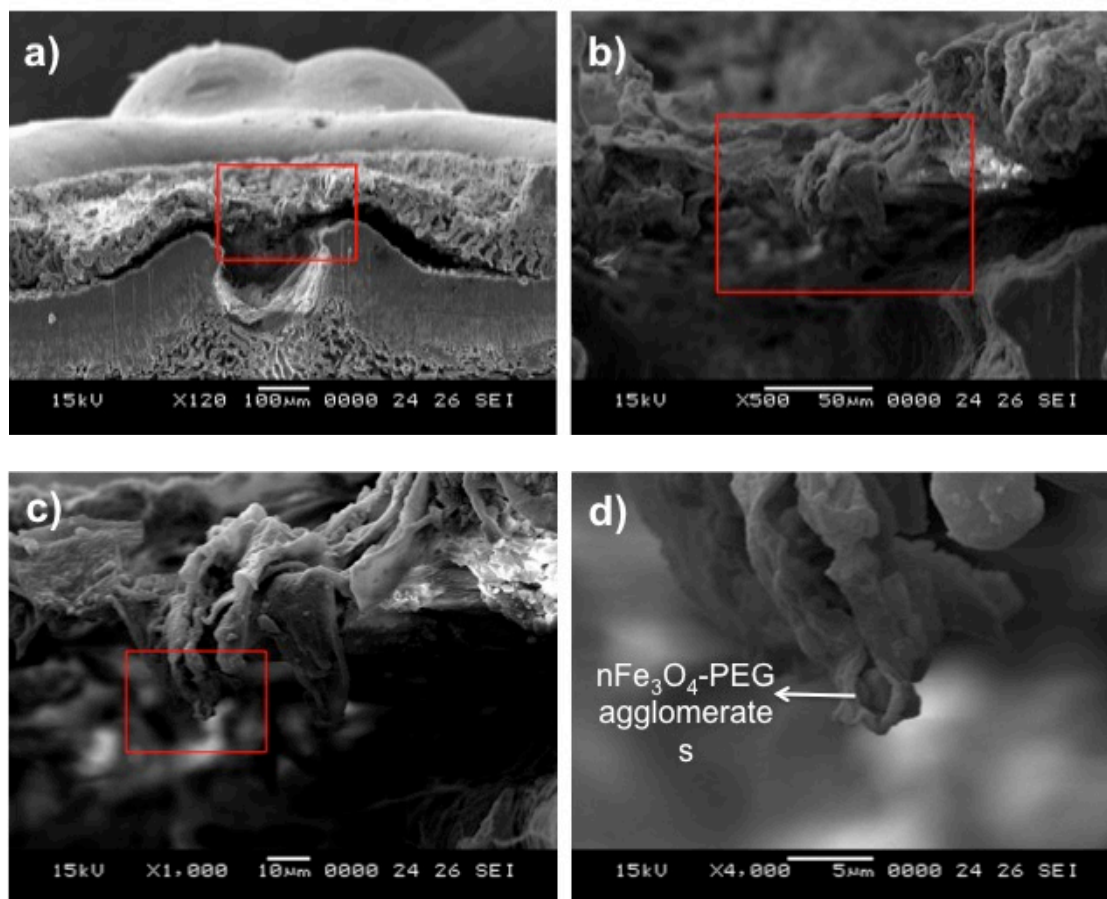


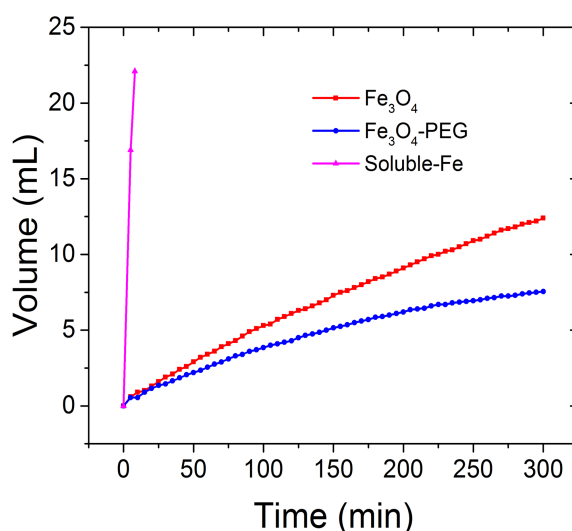
Figure 3.14 - SEM image of the hilum cross section of a *P. vulgaris* seed treated with  $n\text{Fe}_3\text{O}_4\text{-PEG}$  at  $1\,000\text{ mg Fe L}^{-1}$ . (a) Overall view of the hilum (scale bar:  $100\ \mu\text{m}$ ); (b)  $\times 500$  magnification (scale bar:  $50\ \mu\text{m}$ ); (c)  $\times 1\,000$  magnification (scale bar:  $10\ \mu\text{m}$ ); (d)  $\times 4\,000$  magnification highlighting  $n\text{Fe}_3\text{O}_4\text{-PEG}$  agglomerates (scale bar:  $5\ \mu\text{m}$ ); (e) XRF spectrum recorded for the agglomerates to confirm the Fe presence. Red rectangles indicate the selected area for magnification



### 3.3.5 Chemical reactivity of $n\text{Fe}_3\text{O}_4$ and $n\text{Fe}_3\text{O}_4\text{-PEG}$

The chemical reactivity of the tested materials was accessed through the volume of  $\text{O}_2$  produced during the degradation of  $\text{H}_2\text{O}_2$  by the magnetite nanoparticles and soluble-Fe used for seed soaking. The most reactive nanoparticle was  $n\text{Fe}_3\text{O}_4$  which produced 12.4 mL of  $\text{O}_2$  in 300 min, while  $n\text{Fe}_3\text{O}_4\text{-PEG}$  produced 7.5 mL in the same time. On the other hand, soluble-Fe readily produced 22.1 mL in 8 min (Figure 3.15). Iron catalyzes the decomposition of  $\text{H}_2\text{O}_2$  through Fenton reaction. The high reactivity of the soluble-Fe is due to the availability of free ionic Fe that leads to homogenous Fenton reaction, which is faster than the heterogeneous one.<sup>67</sup> On the other hand, the lower reactivity of the PEG coated nanoparticles may be the result of a lower number of available Fe sites, since the nanoparticle surface is sterically hindered by the polymeric chains. This result may explain the non-deleterious effects caused by the coated nanoparticles in the radicle elongation, even at high concentrations.

Figure 3.15 -  $\text{H}_2\text{O}_2$  degradation rate in the presence of  $n\text{Fe}_3\text{O}_4$ ,  $n\text{Fe}_3\text{O}_4\text{-PEG}$  and soluble-Fe. The uncoated magnetite decomposed the  $\text{H}_2\text{O}_2$  faster compared to the coated one. However, the former were much slower compared to the  $\text{O}_2$  release from the soluble-Fe



### 3.3.6 $\alpha$ -amylase activity

The energy source necessary for the germination and early seedling development of leguminous comes mainly from the degradation of proteins and carbohydrates present in the seed reserves. Protein and starch comprise about 20% and 40% of the whole *P. vulgaris* seed, respectively.<sup>68</sup> Here we evaluated the  $\alpha$ -amylase (starch degrading enzyme)

activity in the seedlings whose seeds were soaked in  $n\text{Fe}_3\text{O}_4$ ,  $n\text{Fe}_3\text{O}_4\text{-PEG}$  and soluble-Fe at  $1\,000\text{ mg Fe L}^{-1}$ .

Compared to the result that was obtained for the non-treated seeds ( $1600 \pm 300\text{ U}$ ), soluble-Fe treatment presented the lowest enzymatic activity, followed by  $n\text{Fe}_3\text{O}_4$  ( $730 \pm 30$  and  $760 \pm 140\text{ U}$ , respectively). Reinforcing what was observed in the radicle development and in the chemical reactivity analysis,  $n\text{Fe}_3\text{O}_4\text{-PEG}$  treatment was the least harmful to the  $\alpha$ -amylase activity ( $900 \pm 180\text{ U}$ ) (Table 3.3).

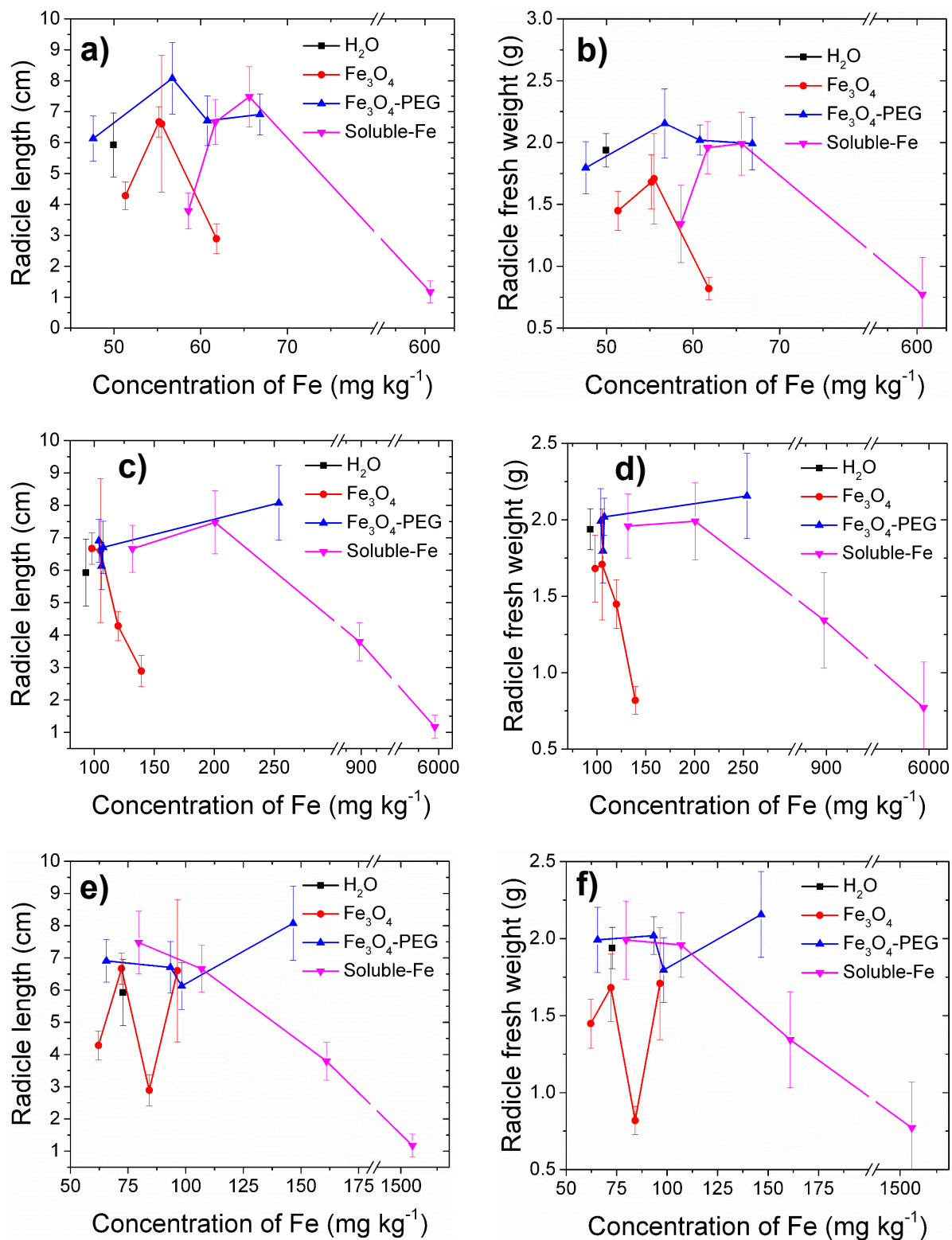
$\alpha$ -amylase is a metalloenzyme which needs  $\text{Ca}^{2+}$  to its activity and stability, its affinity is much stronger than that with others ions.<sup>69</sup> Since  $\text{Fe}^{2+}$  is also a divalent ion, its presence in abundance could provoke a competition with  $\text{Ca}^{2+}$  during the  $\alpha$ -amylase biosynthesis, leading to enzymatic activity loss. This possibility is supported by the previously observed reduction of amylase activity *in vitro* in fish intestine after  $\text{Fe}^{2+}$  addition ( $50\text{ mg kg}^{-1}$ ).<sup>70</sup>

Table 3.3 -  $\alpha$ -amylase activity in *P. vulgaris* seedlings whose seeds were soaked in  $n\text{Fe}_3\text{O}_4$ ,  $n\text{Fe}_3\text{O}_4\text{-PEG}$  and soluble-Fe at  $1\,000\text{ mg Fe L}^{-1}$ . The value of 1 U (enzymatic activity unit) is the reduction of 10% of the colorimetric intensity of the amylose-iodine complex

Treatment	Enzymatic activity (U) average
Control	$1600 \pm 300$
$n\text{Fe}_3\text{O}_4$	$760 \pm 140$
$n\text{Fe}_3\text{O}_4\text{-PEG}$	$900 \pm 180$
Soluble-Fe	$730 \pm 30$

Figure 3.16 attempts to correlate the radicle length and weight to the content of Fe incorporated by the seedling tissues. Although the Fe amount in the seedling tissues was very similar, the biologic effects were distinct: The deleterious effects caused by  $1\,000\text{ mg Fe L}^{-1}$  soluble-Fe can be attributed to phytotoxicity due the excess of this element, as previously discussed. However, the growth promotion induced by  $n\text{Fe}_3\text{O}_4\text{-PEG}$  cannot be explained solely by the content of Fe incorporated by the seedlings. Since the highest seedling growth and weight gain were observed for the  $n\text{Fe}_3\text{O}_4\text{-PEG}$ , and this treatment did not yield the highest  $\alpha$ -amylase activity, one can infer that the decomposition of starch was not the limiting factor for the seedling development.

Figure 3.16 - Correlation between radicle length and weight with the content of Fe incorporated by the following seedling tissues: (a) and (b) cotyledon; (c) and (d) seed coat; (e) and (f) radicle



### 3.4 Conclusions

It was previously demonstrated that Cu from CuO nanoparticles was mostly concentrated in the seed coat of *P. vulgaris* seeds after soaking, especially in the hilum region.<sup>17</sup> In this work, X-ray microtomography and SEM have shown that Fe from magnetite nanoparticles was not only absorbed on the surface of the seed coat, but also penetrated the hilum tissue, evidence that nanoparticles do enter into the seeds. The chemical identity of the incorporated Fe was confirmed by XANES.

Altogether, the results showed that nanomaterials are potential candidates for seed priming. The deleterious effects of magnetite nanoparticles were smaller than those shown by aqueous Fe<sup>3+</sup>/Fe<sup>2+</sup>. Thus, the supplying of nutrients through sources of intermediate solubility makes phytotoxicity less prone to occur. Rather than only transferring nutrients to the roots, X-ray fluorescence, XANES, SEM and tomography showed that the nanoparticles can penetrate within the seed structure and thus modify the seedling development. Finally, the PEG coating played a major role on the properties of the magnetite nanoparticles and might be responsible for the growth promotion reported in this study.

### 3.5 References

- 1 RALIYA, R. et al. Nanofertilizer for precision and sustainable agriculture: current state and future perspectives. **Journal of Agricultural and Food Chemistry**, Washington, DC, 2017 Aug 23. [Epub ahead of print]. DOI:10.1021/acs.jafc.7b02178.
- 2 FAROOQ, M.; WAHID, A.; SIDDIQUE, K. H. M. Micronutrient application through seed treatments - a review. **Journal of Soil Science and Plant Nutrition**, Tokyo, v. 12, n. 1, p. 125-142, 2012.
- 3 HARRIS, D. et al. 'On-farm' seed priming with zinc sulphate solution - A cost-effective way to increase the maize yields of resource-poor farmers. **Field Crops Research**, Amsterdam, v. 102, n. 2, p. 119-127, 2007.
- 4 SARIC, T.; SACIRAGIC, B. Effect of oat seed treatment with microelements. **Plant and Soil**, Dordrecht, v. 31, n. 1, p. 185-187, 1969.
- 5 MARCAR, N. E.; GRAHAM, R. D. Effect of seed manganese content on the growth of wheat (*Triticum aestivum*) under manganese deficiency. **Plant and Soil**, Dordrecht, v. 96, n. 2, p. 165-173, 1986.
- 6 MALHI, S. S. Effectiveness of seed-soaked Cu, autumn- versus spring-applied Cu, and Cu-treated P fertilizer on seed yield of wheat and residual nitrate-N for a Cu-deficient soil. **Canadian Journal of Plant Science**, Ottawa, v. 89, n. 6, p. 1017-1030, 2009.

- 7 KANG, B. T.; OKORO, E. G. Response of flooded rice grown on a vertisol from northern Nigeria to zinc sources and methods of application. **Plant and Soil**, Dordrecht, v. 44, n. 1, p. 15-25, 1976.
- 8 RENGEL, Z.; GRAHAM, R. D. Importance of seed Zn content for wheat growth on Zn-deficient soil - I. Vegetative growth. **Plant and Soil**, Dordrecht, v. 173, n. 2, p. 259-266, 1995.
- 9 MARSCHNER, P. **Mineral nutrition of higher plants**. 3. ed. San Diego: Academic Press, 2012. 672 p.
- 10 SCHWERTMANN, U. Solubility and dissolution of iron-oxides. **Plant and Soil**, Dordrecht, v. 130, n. 1-2, p. 1-25, 1991.
- 11 LOEPPERT, R. H.; CLARKE, E. T. Reactions of  $Fe^{2+}$  and  $Fe^{3+}$  in calcareous soils. **Journal of Plant Nutrition**, New York, v. 7, n. 1-5, p. 149-163, 1984.
- 12 COLOMBO, C. et al. Review on iron availability in soil: interaction of Fe minerals, plants, and microbes. **Journal of Soils and Sediments**, Heidelberg, v. 14, n. 3, p. 538-548, 2014.
- 13 MIELKI, G. F. et al. Iron availability in tropical soils and iron uptake by plants. **Revista Brasileira de Ciencia do Solo**, Vicosa, v. 40, n. e0150174, p. 1-14, 2016.
- 14 TANG, C. X.; ROBSON, A. D.; DILWORTH, M. J. The role of iron in nodulation and nitrogen-fixation in *Lupinus angustifolius* L. **New Phytologist**, Malden, v. 114, n. 2, p. 173-182, 1990.
- 15 MORAN, J. F. et al. Complexes of iron with phenolic compounds from soybean nodules and other legume tissues: Prooxidant and antioxidant properties. **Free Radical Biology and Medicine**, Oxford, v. 22, n. 5, p. 861-870, 1997.
- 16 PEREZ, A. A. G. et al. Nutrient extraction and exportation by nitrogen-fertilized common bean grown after different periods of no-tillage system establishment. **Revista Brasileira de Ciencia do Solo**, Vicosa, v. 37, n. 5, p. 1276-1287, 2013.
- 17 DURAN, N. M. et al. X-ray spectroscopy uncovering the effects of Cu based nanoparticle concentration and structure on *Phaseolus vulgaris* germination and seedling development. **Journal of Agricultural and Food Chemistry**, Washington, DC, v. 65, n. 36, p. 7874-7884, 2017.
- 18 SANTOS, E. F. et al. Physiological highlights of manganese toxicity symptoms in soybean plants: Mn toxicity responses. **Plant Physiology and Biochemistry**, Paris, v. 113, p. 6-19, 2017.
- 19 OZTURK, L. et al. Shoot biomass and zinc/cadmium uptake for hyperaccumulator and non-accumulator *Thlaspi* species in response to growth on a zinc deficient calcareous soil. **Plant Science**, Clare, v. 164, n. 6, p. 1095-1101, 2003.
- 20 FIGUEROLA, A. et al. From iron oxide nanoparticles towards advanced iron-based inorganic materials designed for biomedical applications. **Pharmacological Research**, London, v. 62, n. 2, p. 126-143, 2010.

- 21 LAURENT, S. et al. Magnetic iron oxide nanoparticles: Synthesis, stabilization, vectorization, physicochemical characterizations, and biological applications. **Chemical Reviews**, Washington, DC, v. 108, n. 6, p. 2064-2110, 2008.
- 22 TRUJILLO-REYES, J. et al. Exposure studies of core-shell Fe/Fe<sub>3</sub>O<sub>4</sub> and Cu/CuO NPs to lettuce (*Lactuca sativa*) plants: Are they a potential physiological and nutritional hazard? **Journal of Hazardous Materials**, Amsterdam, v. 267, p. 255-263, 2014.
- 23 ZHANG, Y.; KOHLER, N.; ZHANG, M. Q. Surface modification of superparamagnetic magnetite nanoparticles and their intracellular uptake. **Biomaterials**, Oxon, v. 23, n. 7, p. 1553-1561, 2002.
- 24 XIE, J. et al. Controlled PEGylation of monodisperse Fe<sub>3</sub>O<sub>4</sub> nanoparticles for reduced non-specific uptake by macrophage cells. **Advanced Materials**, Weinheim, v. 19, n. 20, p. 3163-3166, 2007.
- 25 LANDA, P. et al. Effect of metal oxides on plant germination: phytotoxicity of nanoparticles, bulk materials, and metal ions. **Water Air and Soil Pollution**, Dordrecht, v. 227, n. 448, p. 1-10, 2016.
- 26 ZHU, H. et al. Uptake, translocation, and accumulation of manufactured iron oxide nanoparticles by pumpkin plants. **Journal of Environmental Monitoring**, Cambridge, v. 10, n. 6, p. 713-717, 2008.
- 27 LI, X. et al. Stimulation of peanut seedling development and growth by zero-valent iron nanoparticles at low concentrations. **Plos One**, San Francisco, v. 10, n. 4, p. 1-12, 2015.
- 28 LI, J. L. et al. Physiological effects of magnetic iron oxide nanoparticles towards watermelon. **Journal of Nanoscience and Nanotechnology**, Valencia, v. 13, n. 8, p. 5561-5567, 2013.
- 29 GUPTA, A. K.; GUPTA, M. Synthesis and surface engineering of iron oxide nanoparticles for biomedical applications. **Biomaterials**, Oxon, v. 26, n. 18, p. 3995-4021, 2005.
- 30 GUPTA, A. K.; WELLS, S. Surface-modified superparamagnetic nanoparticles for drug delivery: Preparation, characterization, and cytotoxicity studies. **IEEE Transactions on Nanobioscience**, Piscataway, v. 3, n. 1, p. 66-73, 2004.
- 31 YAMASHITA, T.; HAYES, P. Analysis of XPS spectra of Fe<sup>2+</sup> and Fe<sup>3+</sup> ions in oxide materials. **Applied Surface Science**, Amsterdam, v. 254, n. 8, p. 2441-2449, 2008.
- 32 ROSSI, G. B. et al. Comparison of grain proteome profiles of four brazilian common bean (*Phaseolus vulgaris* L.) cultivars. **Journal of Agricultural and Food Chemistry**, Washington, DC, v. 65, n. 34, p. 7588-7597, 2017.
- 33 SAKO, Y. et al. A system for automated seed vigour assessment. **Seed Science and Technology**, Zurich, v. 29, n. 3, p. 625-636, 2001.
- 34 VIEIRA, C.; PAULA JÚNIOR, T. J.; BORÉM, A. **Feijão**. 2. ed. Viçosa: Universidade Federal de Viçosa, 2006. 600 p.

- 35 DURAN, N. M. et al. Bean seedling growth enhancement using magnetite nanoparticles. **Journal of Agricultural and Food Chemistry**, Washington, DC, 2018. [Epub ahead of print].
- 36 RAVEL, B.; NEWVILLE, M. ATHENA, ARTEMIS, HEPHAESTUS: data analysis for X-ray absorption spectroscopy using IFEFFIT. **Journal of Synchrotron Radiation**, Copenhagen, v. 12, p. 537-541, 2005.
- 37 SILVA, A. C. et al. Nb-containing hematites  $\text{Fe}_{2-x}\text{Nb}_x\text{O}_3$ : The role of  $\text{Nb}^{5+}$  on the reactivity in presence of the  $\text{H}_2\text{O}_2$  or ultraviolet light. **Applied Catalysis A: General**, Amsterdam, v. 357, n. 1, p. 79-84, 2009.
- 38 CARVALHO, H. W. P. et al. Improvement of the photocatalytic activity of magnetite by Mn-incorporation. **Materials Science and Engineering: B - Advanced Functional Solid-State Materials**, Amsterdam, v. 181, p. 64-69, 2014.
- 39 FUWA, H. A new method for microdetermination of amylase activity by the use of amylose as the substrate. **Journal of Biochemistry**, Tokyo, v. 41, n. 5, p. 583-603, 1954.
- 40 ALBANESE, A.; CHAN, W. C. W. Effect of gold nanoparticle aggregation on cell uptake and toxicity. **Acs Nano**, Washington, DC, v. 5, n. 7, p. 5478-5489, 2011.
- 41 CHEGEL, V. et al. Gold nanoparticles aggregation: drastic effect of cooperative functionalities in a single molecular conjugate. **Journal of Physical Chemistry C**, Washington, DC, v. 116, n. 4, p. 2683-2690, 2012.
- 42 SALIS, A. et al. Measurements and Theoretical interpretation of points of zero charge/potential of BSA protein. **Langmuir**, Washington, DC, v. 27, n. 18, p. 11597-11604, 2011.
- 43 THIJIS, H. M. L. et al. Water uptake of hydrophilic polymers determined by a thermal gravimetric analyzer with a controlled humidity chamber. **Journal of Materials Chemistry**, Cambridge, v. 17, n. 46, p. 4864-4871, 2007.
- 44 SCHWUGER, M. Mechanism of interaction between ionic surfactants and polyglycol ethers in water. **Journal of Colloid and Interface Science**, San Diego, v. 43, n. 2, p. 491-498, 1973.
- 45 DAS, B.; SAHA, P. K. Ultrastructural dimorphism of micropyle determines differential germinability of *Sesbania cannabina* seeds. **Seed Science and Technology**, Zurich, v. 34, n. 2, p. 363-372, 2006.
- 46 LIN, D. H.; XING, B. S. Phytotoxicity of nanoparticles: Inhibition of seed germination and root growth. **Environmental Pollution**, Oxford, v. 150, n. 2, p. 243-250, 2007.
- 47 ZHANG, R. C. et al. Phytotoxicity of ZnO nanoparticles and the released Zn(II) ion to corn (*Zea mays* L.) and cucumber (*Cucumis sativus* L.) during germination. **Environmental Science and Pollution Research**, Landsberg, v. 22, n. 14, p. 11109-11117, 2015.

- 48 NAIR, P. M. G.; CHUNG, I. M. Physiological and molecular level studies on the toxicity of silver nanoparticles in germinating seedlings of mung bean (*Vigna radiata* L.). **Acta Physiologiae Plantarum**, Warszawa, v. 37, n. 1, p. 1719, 2015. DOI: 10.1007/s11738-014-1719-1.
- 49 ADAMS, J. et al. Cu from dissolution of CuO nanoparticles signals changes in root morphology. **Plant Physiology and Biochemistry**, Paris, v. 110, p. 108-117, 2017.
- 50 CASTIGLIONE, M. R. et al. The effects of nano-TiO<sub>2</sub> on seed germination, development and mitosis of root tip cells of *Vicia narbonensis* L. and *Zea mays* L. **Journal of Nanoparticle Research**, Dordrecht, v. 13, n. 6, p. 2443-2449, 2011.
- 51 ALIDOUST, D.; ISODA, A. Effect of gamma Fe<sub>2</sub>O<sub>3</sub> nanoparticles on photosynthetic characteristic of soybean (*Glycine max* L.) Merr.): foliar spray versus soil amendment. **Acta Physiologiae Plantarum**, Warszawa, v. 35, n. 12, p. 3365-3375, 2013.
- 52 ALIDOUST, D.; ISODA, A. Phytotoxicity assessment of gamma-Fe<sub>2</sub>O<sub>3</sub> nanoparticles on root elongation and growth of rice plant. **Environmental Earth Sciences**, New York, v. 71, n. 12, p. 5173-5182, 2014.
- 53 KIM, J. H. et al. Exposure of iron nanoparticles to *Arabidopsis thaliana* enhances root elongation by triggering cell wall loosening. **Environmental Science & Technology**, Washington, DC, v. 48, n. 6, p. 3477-3485, 2014.
- 54 RUI, M. M. et al. Iron oxide nanoparticles as a potential iron fertilizer for peanut (*Arachis hypogaea*). **Frontiers in Plant Science**, Lausanne, v. 7, n. 815, p. 1-10, 2016.
- 55 YU, M. et al. Dextran and polymer polyethylene glycol (PEG) coating reduce both 5 and 30 nm iron oxide nanoparticle cytotoxicity in 2D and 3D cell culture. **International Journal of Molecular Sciences**, Basel, v. 13, n. 5, p. 5554-5570, 2012.
- 56 PROM-U-THAI, C. et al. Zinc priming promotes seed germination and seedling vigor of rice. **Journal of Plant Nutrition and Soil Science**, Weinheim, v. 175, n. 3, p. 482-488, 2012.
- 57 MIKAC, U.; SEPE, A.; SERSA, I. MR microscopy for noninvasive detection of water distribution during soaking and cooking in the common bean. **Magnetic Resonance Imaging**, New York, v. 33, n. 3, p. 336-345, 2015.
- 58 JHALA, V. M.; THAKER, V. S. X-ray computed tomography to study rice (*Oryza sativa* L.) panicle development. **Journal of Experimental Botany**, Oxford, v. 66, n. 21, p. 6819-6825, 2015.
- 59 ROUSSEAU, D. et al. Fast virtual histology using X-ray in-line phase tomography: application to the 3D anatomy of maize developing seeds. **Plant Methods**, London, v. 11, n. 55, p. 1-10, 2015.
- 60 VERBOVEN, P. et al. Void space inside the developing seed of *Brassica napus* and the modelling of its function. **New Phytologist**, Malden, v. 199, n. 4, p. 936-947, 2013.

- 61 BLUNK, S. et al. Quantification of differences in germination behaviour of pelleted and coated sugar beet seeds using X-ray computed tomography (X-ray CT). **Biomedical Physics & Engineering Express**, Bristol, v. 3, n. 4, p. 1-11, 2017.
- 62 ZONG, Y. B. et al. Selection for oil content during soybean domestication revealed by X-ray tomography of ancient beans. **Scientific Reports**, London, v. 7, n. 43595, p. 1-10, 2017.
- 63 MURPHY, C.; FULLER, D. Q. Seed coat thinning during horsegram (*Macrotyloma uniflorum*) domestication documented through synchrotron tomography of archaeological seeds. **Scientific Reports**, London, v. 7, n. 5369, p. 1-9, 2017.
- 64 AVELLAN, A. et al. Nanoparticle uptake in plants: gold nanomaterial localized in roots of *Arabidopsis thaliana* by X-ray computed nanotomography and hyperspectral imaging. **Environmental Science & Technology**, Washington, DC, v. 51, n. 15, p. 8682-8691, 2017.
- 65 CHEN, Y. Y. et al. Observation of yttrium oxide nanoparticles in cabbage (*Brassica oleracea*) through dual energy K-edge subtraction imaging. **Journal of Nanobiotechnology**, London, v. 14, n. 23, p. 1-10, 2016.
- 66 AJIBOYE, B.; AKINREMI, O. O.; JURGENSEN, A. Experimental validation of quantitative XANES analysis for phosphorus speciation. **Soil Science Society of America Journal**, Madison, v. 71, n. 4, p. 1288-1291, 2007.
- 67 XAVIER, S. et al. Comparison of homogeneous and heterogeneous Fenton processes for the removal of reactive dye Magenta MB from aqueous solution. **Desalination and Water Treatment**, Philadelphia, v. 53, n. 1, p. 109-118, 2015.
- 68 MARQUEZI, M. et al. Physical and chemical properties of starch and flour from different common bean (*Phaseolus vulgaris* L.) cultivars. **Brazilian Journal of Food Technology**, Campinas, v. 19, e2016005, p. 1-8, 2016.
- 69 GUPTA, R. et al. Microbial alpha-amylases: a biotechnological perspective. **Process Biochemistry**, Oxon, v. 38, n. 11, p. 1599-1616, 2003.
- 70 LI, J. S.; LI, J. L.; WU, T. T. The effects of copper, iron and zinc on digestive enzyme activity in the hybrid tilapia *Oreochromis niloticus* (L.) x *Oreochromis aureus* (Steindachner). **Journal of Fish Biology**, Oxon, v. 71, n. 6, p. 1788-1798, 2007.



#### 4. FINAL REMARKS AND OUTLOOK

The investigation of how plants benefit from seed priming by nanoparticulate nutrients is a challenging topic. The results here presented indicate that, beyond the nanoparticle type (Cu or Fe), the priming effects on the seedling development of *P. vulgaris* are strongly influenced by the nanoparticle size, surface coverage and the applied concentration.

The seed priming not only supplied Cu and Fe as nutrient to the seedlings, but also affected its growth. Exposing seeds to 40 nm nCuO at 100 mg Cu L<sup>-1</sup> and nFe<sub>3</sub>O<sub>4</sub>-PEG at 1 000 mg Fe L<sup>-1</sup> positively affected the seedling development after 5 days of germination, whereas 1 000 mg Cu/Fe L<sup>-1</sup> for the 25 nCuO and bare magnetite treatments prevented it.

Although most of the metal oxides are virtually insoluble in water, solubility tests carried out by XRF analysis indicated that a small amount of Cu ions were released from nCuO dispersions. Interestingly, in this case, the smaller the nanoparticle size, the greater the solubility. Albeit ions release may occur in the soaking solution, the promotion and inhibition of the seedling development might be a consequence of the slow release of ions from the oxide structure to the physiological solution during the germination process.

The XRF results indicated that most of the incorporated Cu/Fe remains in the seed coat, especially in the hilum region, which is the structure responsible for the water entrance during the imbibition process. X-ray tomography complemented this data by demonstrating that Fe from nFe<sub>3</sub>O<sub>4</sub>-PEG can penetrate within this tissue, whereas XAS and SEM-EDX confirmed the presence of magnetite inside the hilum. XAS also unraveled that most of the Cu incorporated by the seeds soaked in nCuO dispersions remained in its pristine form, except for the 40 nm nCuO treatment that presented in the embryo of the seeds Cu slightly reduced compared to that found in the seed coat, an evidence that nanoparticles can be biotransformed after seed soaking.

Much attention must be paid to the core shell effects. Differently from the others, the 25 nm nCuO consisted of a metallic core made of Cu covered by oxidized layers of Cu<sub>2</sub>O and CuO, which made this treatment the most harmful to the seedling development and also the most chemically reactive. The final disposal of that kind of nanoparticle is an environmental issue to be addressed.

On the other hand, the surface chemistry modification by hydrophilic materials like PEG can be a promise way to boost seedling development. The highest radicle elongation caused by nFe<sub>3</sub>O<sub>4</sub>-PEG might be the outcome of a higher water uptake by the seedlings tissues induced by the PEG. This coating material provided magnetite nanoparticles less reactive and less toxic to the seedlings.

Therefore, depending on its physical-chemical properties, the use of CuO and magnetite nanoparticles on seed priming can be a promise way to enhance *P. vulgaris* development since, in general, toxicity caused by nanoparticles was less prone to occur than by conventional soluble sources (CuSO<sub>4</sub> and Fe<sup>3+</sup>/Fe<sup>2+</sup>).

Further investigations are necessary once the results here presented concern only for the early growth stages of the plant and the effects for the advanced ones still unknown. Besides that, these responses may vary according to the crops and genotypes.